

STRUCTURAL PLASTICITY IN NEURONAL NETWORKS

Thesis by
Shreesh Pranesh Mysore

In Partial Fulfillment of the Requirements
for the Degree of
Doctor of Philosophy



California Institute of Technology
Pasadena, California
2007
(Defended September 25, 2006)

© 2007

Shreesh P. Mysore

All Rights Reserved

Acknowledgements

My journey to a Ph.D. has been via the scenic route – challenging and a tad long, but immensely enjoyable with a wide variety of research experiences and several wonderful mentors. Consequently, I have many people to thank.

I sincerely thank Prof. Erin Schuman, my adviser on the experimental part of this thesis, for her surprisingly, to me, great belief in my ability. When I first showed up in her office three years ago, Erin accepted my complete lack of experience in experimental biology at that time without so much as a hint of hesitation and permitted me to join her lab. The underlying philosophy of her lab to pursue any question of interest in neuroscience without constraints embodies wonderfully the fundamental spirit of the scientific quest and has facilitated an exciting, fun, and stimulating research experience. Without her support and guidance, I would never have started on the path of experimental neuroscience, a field that continues to fascinate me to no end, and one that I wish to make my academic home. She has repeatedly encouraged me when I least expected it, and has been a great research mentor. Her deep insight and incisive intellect are qualities I aspire to.

I am deeply indebted to Prof. Steven Quartz, my adviser on the computational modeling part of this thesis, who took me on at the darkest hour of my stay at Caltech – my self-confidence was at its nadir, yet he seemed to think I had potential to do very well. When I first started working with Steve, he was as much a friend as a research guide, and he opened my eyes to the world of neuroscience – both the experimental and

the computational modeling projects in my thesis were originally suggested by him. I have been repeatedly inspired by his ideas, his openness, his ability to motivate, and his desire to nurture the careers of young researchers. If not for Steve, I would not be here now, writing my Ph.D. thesis.

I am very thankful to Prof. Christof Koch in whose lab I worked for nearly a year and a half. At a critical juncture, he suggested a course-correction for me that, in hindsight, was a much needed one. I was too close to a problem to see it, but he gently suggested a solution and nudged me in the right direction. For this, and for his endless enthusiasm for science, I am very grateful.

I am extremely thankful for, and constantly astonished by, the breadth of the vision of the Control and Dynamical Systems (CDS) option at Caltech. Beginning with my application to this program, my research interests have never been within what some may consider as being the boundaries of a rigorous applied mathematics type program. Yet, since the first time I visited Caltech as a prospective, and all through the ups and downs of my graduate experience at Caltech, CDS, and particularly Prof. Richard Murray, have always encouraged my interests wholeheartedly. I have encountered no boundaries at all as I have tried to cross imaginary ones across research fields, and there are few other universities and departments where I could have expected broad-mindedness to such an extent, and such an inviting and invigorating research atmosphere. In hindsight, my decision to come here (over MIT) is one I would make again in a heartbeat. To Prof. Murray, CDS, and Caltech, I owe a great debt of gratitude.

The time I spent at Penn State before Caltech, in Prof. Soundara Kumara's lab, was critical to my growth as a scientist. I learned all kinds of wonderful mathematics

while in his lab, and without that, I would not be able to appreciate so much of what I now can. When I was still an undergraduate, it was his research that inspired me to embark on the quest to understand, model, and design learning and intelligence. I was a clueless senior when he called up my home in Chennai to offer me a spot in his research group, and in the three years I spent in his lab, I learned so much about research, science, mentoring, and the passionate pursuit of science and engineering. For Dr. Kumara's inspiring research, for excellent academic guidance, for the total academic freedom he allowed, and for his wonderful and warm heart, I cannot thank him enough. A truly wise person is Dr. Kumara, and I will be happy if I am even half of who he is, academically, and otherwise.

Also at Penn State, I was greatly influenced by Prof. Asok Ray. He served more as a mentor than as the instructor of several wonderful Math classes. A better teacher I have yet to encounter. His passion for understanding phenomena at a fundamental level and for solving problems influences all who work with him. A deep thinker, and a rigorous scientist, he continues to be one of my role models.

Before Penn State, there was IIT Madras. The seeds for my academic interest in all things to do with learning and intelligence were sowed during a year-long series of lectures on artificial neural networks by Prof. B. Yegnanarayana. I was still an undergraduate in Mechanical Engineering then, and these graduate classes in Computer Science riveted my attention like no other classes had in my entire four years. I thank him for teaching the subject so well and with such obvious zeal for the field.

My peers and friends have also contributed greatly to the joy of learning and living as a graduate student. Dr. Michael Sutton spent huge dollops of his time educating

me about neurobiology, sharing his ideas and generally being an older research-brother in the Schuman lab. The clarity of his thinking about neuroscience, and the purity of his motives regarding science have been truly inspiring. All I can say is, “Mike, I want to steal your brain!” Dr. Chin-Yin Tai, also in the Schuman lab, has taught me everything I know about doing good experiments and doing them well. She has the best pair of hands I have seen in an experimentalist and I have bugged, annoyed, and generally been a parasite while trying to learn from her. For smilingly tolerating me, Chin-Yin, I cannot thank you enough. I am grateful to Dr. Daniela Dieterich, Dr. Young “N” Yoon, Dr. Sally Kim, and Jennifer Lee for livening up my life with music, gummy bears, double-or-nothing, funny cat videos, and a whole host of other things. You guys rock! I am deeply grateful to Alana Rathbun, also in the Schuman Lab, for caring so much about all of us. We call her the lab-mom, and there is no better appellation to describe what she means to us. Thanks, Alana! I have greatly enjoyed my interaction with the members of Schuman lab who have made it a blast to work alongside them. Thanks also to Fritz Rohweder for many a deep conversation. To my buddies, especially Cedric Anen, Dr. Harish Bhat, Dr. Domitilla Delvecchio, Melvin Flores, Dr. Ming Hsu, Asha Iyer, Rajesh Iyer, Dr. Melvin Leok, Xin Liu, Geetanjali Mande, Dr. Martin Meckesheimer, Dr. Sivakumar Mudanai, Arvinth Murugan, Dr. Antonis Papachristodoulou, Dr. Steven Prajna Dr. Abhijit Shevade, Dr. Sathyan Subbiah, and Pranjal Trivedi – thank you guys, for sharing your lives with me; it has been fantastic. Abhi and Geeta – thanks for all the food and the love.

During my graduate work, four books have taken great hold over my thinking and have entirely changed (and I believe for the better) how I view life. They are my all-time

favorites and I owe many thanks to their authors – Hermann Hesse for *Siddhartha* and *Narcissus and Goldmund*, Paulo Coelho for *The Alchemist*, and Plato for *The Republic*.

For as long as I can remember, I have always wanted to be an academic, and for this, I have my dad, Prof. M. R. Pranesh, to thank. His incredible intellect, unwavering integrity, unflinching discipline, and remarkable simplicity have molded me all my life. Thanks, dad, for instilling in me a desire for excellence, and for being there in ways I still don't fully appreciate. My mom, Mrs. Rama Pranesh, gets almost all the credit for who I am today. For her wonderful patience, wisdom, understanding, and for choosing to raise us full-time, I cannot thank her enough; if not for her, I would be nothing. Of all her wonderful gifts to me, the greatest is music – a love for it, and an appreciation of its ability to uplift one's soul. If I were not an aspiring academic, I would most certainly be an aspiring musician, all thanks to her. My sister, Dr. M. P. Veenashree has been a lighthouse for me all my life – always there, always guiding, always urging me to reach higher, and be wiser. From my earliest memory, she has been my best friend and someone who has understood me better than I have done myself. Thanks, sis!

I dedicate this thesis to Dr. Hita Adwanikar. When I first met her, it seemed like we had known each other for eons, and that we were simply picking up from where we had last left off. The path to my Ph.D. has been as much spiritual as intellectual, and she is the greatest gift this path has given me; she makes my life worth living. Thanks, Hita, for who you are and for your love!

Abstract

Neuronal networks are established during development by the formation of connections (synapses) between neurons. Once formed, these synapses undergo experience-dependent modifications throughout the lifespan of the animal (synaptic plasticity). Additionally, the connectivity pattern itself can be modified in an activity-dependent manner (architectural plasticity). Changes in the structure of synapses, neurons, and networks – collectively called structural plasticity – are the predominant mechanisms for changes in the network architecture in the brain. Structural plasticity forms the focus of this thesis and motivates both the experimental and the computational modeling work reported here. With experiments, we look in detail at one form of structural plasticity, namely dendritic spine dynamics. We develop a unified approach to characterize motility and use this both to detect subtle forms of structural dynamics and to uncover novel phenomena in it. We show that disruption of N-cadherin, a synaptic adhesion molecule, causes spines to first be more motile and to shrink in length, and then to be lost. Along with this, synapses are eliminated as well. For the first time, we show that early structural changes can predict later synapse elimination, suggesting that early dynamics may be readouts for future changes in the neural wiring diagram. We also address some of the related mechanistic questions. In our computational modeling work, we address structural plasticity at the next higher scale of complexity. We provide a novel, neurobiologically plausible, and experimentally consistent explanation for how changes in visual experience may produce axogenesis and the formation of new synaptic pathways in the barn owl auditory

localization system. We discuss implications of architectural plasticity to the representational power of networks and explore links with statistical learning theory. Taken together, our work argues that architectural changes are a powerful and indispensable form of neural plasticity and sheds new light on the mechanisms of structural plasticity in the brain, thereby contributing to our understanding of learning and memory.

Table of Contents

ACKNOWLEDGEMENTS.....	iii
ABSTRACT.....	viii
CHAPTER 1. INTRODUCTION	1
1.1 BACKGROUND	2
<i>A. Synaptic communication.....</i>	2
<i>B. Spines.....</i>	4
<i>C. Classification of spines.....</i>	6
<i>D. Composition of spines</i>	6
1.2 STRUCTURAL MECHANISMS OF ARCHITECTURAL PLASTICITY	8
<i>A. Spine motility.....</i>	8
<i>B. Changes in spine density and synapse number.....</i>	9
<i>C. Neurogenesis.....</i>	11
1.3 ARCHITECTURAL PLASTICITY AND REPRESENTATION CONSTRUCTION	13
1.4 SUMMARY OF THE REMAINDER OF THE THESIS	15
<i>A. Characterization of spine motility.....</i>	16
<i>B. Regulation of spine dynamics and synaptic function by N-cadherin.</i>	16
<i>C. Modeling architectural plasticity in the auditory localization system of barn owls</i>	17
CHAPTER 2. CHARACTERIZATION OF SPINE MOTILITY	18
2.1 SPINE QUANTIFIERS IN THE LITERATURE	20
2.2 UNIFIED SCHEME FOR CHARACTERIZING MOTILITY – SIZE, POSITION, TIMESCALE, AND SHAPE	22
<i>A. Preprocessing: live imaging to spine verification.....</i>	24
<i>B. Acquisition protocol</i>	25
<i>C. Size, position, and shape</i>	25
<i>D. Two timescales in each quantifier</i>	26
<i>E. Comparing groups of spines</i>	26
<i>F. Noise sources – correcting for them or estimating their contributions.....</i>	28
<i>G. Advanced shape quantification with EFFs.....</i>	33
2.3 CONCLUSIONS	40
CHAPTER 3. REGULATION OF SPINE DYNAMICS AND SYNAPTIC FUNCTION BY N-CADHERIN	42
3.1 INTRODUCTION	42
3.2 METHODS	44
<i>A. Cell culture and infection</i>	44
<i>B. N-cadherin disruption.....</i>	45

C. <i>Live imaging</i>	45
D. <i>Analysis</i>	45
E. <i>Statistical comparisons</i>	46
F. <i>Electrophysiology</i>	47
G. <i>Immunoprecipitation</i>	47
H. <i>Immunofluorescence</i>	48
I. <i>L-cells aggregation assay</i>	49
3.3 RESULTS: FAST AND SLOW SPINE DYNAMICS ARE PRECURSORS OF SPINE LOSS	50
A. <i>More spines are motile after N-cadherin disruption</i>	50
B. <i>More spines shrink in length after N-cadherin disruption</i>	53
C. <i>N-cadherin disruption induces spine loss and synapse elimination</i>	55
D. <i>Increased spine motility and shorter spine length after N-cadherin disruption predict later spine loss</i>	58
3.4 RESULTS: SUBCELLULAR EFFECTS OF ACUTE N-CADHERIN DISRUPTION	60
A. <i>N-cadherin disruption produces a biphasic response in spine β-catenin</i>	61
B. <i>N-cadherin disruption reduces binding of β-catenin to N-cadherin, but not to other binding partners</i>	62
C. <i>N-cadherin disruption produces biphasic responses in endogenous β-catenin and surface N-cadherin</i>	64
D. <i>N-cadherin disruption produces long-lasting effects on N-cadherin mediated adhesion in L-cells</i>	67
3.6 CONCLUSIONS	69
3.7 FUTURE DIRECTIONS	70
A. <i>Structural compensation in response to N-cadherin disruption</i>	70
B. <i>Functional recovery after N-cadherin disruption</i>	70
C. <i>Correlating structure-function changes at synapses after N-cadherin disruption</i>	70
D. <i>Changes to synaptic protein distributions after N-cadherin disruption: detailed investigation</i>	71
E. <i>Uncovering the signaling mechanisms in detail</i>	71
F. <i>What is unique about the spines that are lost?</i>	72
G. <i>Predicting structural dynamics</i>	73
H. <i>Why do neighboring spines display widely different dynamics?</i>	73
I. <i>Spine twitching: moment-to-moment regulation of synaptic efficacy?</i>	73
CHAPTER 4. MODELING ARCHITECTURAL PLASTICITY IN THE AUDITORY LOCALIZATION SYSTEM OF BARN OWLS	75
4.1 INTRODUCTION	75
4.2 KEY EXPERIMENTAL OBSERVATIONS	76
4.3 MODELING EFFORTS IN LITERATURE	85
4.4 MODEL	87
A. <i>Assumptions</i>	87
B. <i>The roles of inhibition</i>	88
C. <i>Neuron and plasticity model</i>	89
D. <i>Choice of parameter values</i>	90
4.5 RESULTS AND PREDICTIONS	91

<i>A. Responses in a normal network</i>	91
<i>B. Plasticity upon exposure to prism</i>	93
<i>C. Predictions</i>	98
4.6 CONCLUSIONS	98
4.7 FUTURE DIRECTIONS	99
CHAPTER 5. GENERAL DISCUSSION	100
5.1 N-CADHERIN, SPINE DYNAMICS, AND STRUCTURAL PLASTICITY.....	100
5.2 ARCHITECTURAL PLASTICITY AND REPRESENTATION CONSTRUCTION: BARN OWLS AND BEYOND	101
REFERENCES	105

Table of Figures

FIGURE 1-1. REPRESENTATIVE PYRAMIDAL NEURON FROM RAT HIPPOCAMPUS SHOWING NUMEROUS DENDRITIC SPINES.	5
FIGURE 1-2. MORPHOLOGICAL CLASSIFICATION AND SUBCELLULAR COMPOSITION OF DENDRITIC SPINES.	8
FIGURE 2-1. MORPHOLOGICAL DYNAMICS (“MOTILITY”) OF DENDRITIC SPINES.	19
FIGURE 2-2. UNIFIED SCHEME AND SUMMARY OF STEPS FOR CHARACTERIZING SPINE MOTILITY.	23
FIGURE 2-3. QUANTIFYING SPINE DYNAMICS.	27
FIGURE 2-4. ESTIMATING NOISE-FLOORS.	32
FIGURE 2-5. SUMMARIZING SPINE SHAPE WITH EFFS – EXAMPLE 1.	36
FIGURE 2-6. SUMMARIZING SPINE SHAPE WITH EFFS – EXAMPLE 2.	38
FIGURE 2-7. COMPARING RECONSTRUCTION ERRORS AND EFF FREQUENCY SPECTRA OF TWO SPINES.	39
FIGURE 3-1. MORE SPINES SHOW AN INCREASE IN CENTER-OF-MASS MOTILITY AFTER SURFACE N-CADHERIN DISRUPTION.	52
FIGURE 3-2. MORE SPINES SHRINK IN LENGTH AFTER SURFACE N-CADHERIN DISRUPTION.	55
FIGURE 3-3. ACUTE DISRUPTION OF SURFACE N-CADHERIN INDUCES SPINE LOSS.	57
FIGURE 3-4. INCREASED SPINE MOTILITY AND SHORTER SPINE LENGTH AT EARLY TIME POINT AFTER N-CADHERIN DISRUPTION PREDICT LATER SPINE LOSS.	59
FIGURE 3-5. β -CATENIN-GFP SHOWS A BIPHASIC RESPONSE IN SPINES AFTER SURFACE N- CADHERIN DISRUPTION.	62
FIGURE 3-6. β -CATENIN BINDING TO N-CADHERIN IS PREFERENTIALLY REDUCED 30 MINUTES AFTER SURFACE N-CADHERIN DISRUPTION.	64
FIGURE 3-7. N-CADHERIN DISRUPTION PRODUCES A BIPHASIC RESPONSE IN ENDOGENOUS β - CATENIN AND N-CADHERIN.	66
FIGURE 3-8. N-CADHERIN DISRUPTION BY 10 MIN HAV TREATMENT CAUSES LONG LASTING EFFECTS ON CADHERIN-MEDIATED ADHESION.	68
FIGURE 4-1. MIDBRAIN ITD PATHWAY IN BARN OWLS.	78
FIGURE 4-2. SIMULTANEOUS PRESENTATION OF SPATIALLY COINCIDENTAL AUDIO-VISUAL INPUT TO NORMAL OWL.	82
FIGURE 4-3. SCHEMATIC OF THE NETWORK IMMEDIATELY AFTER PRISM-FITTING.	83
FIGURE 4-4. SCHEMATIC OF THE NETWORK AFTER STRUCTURAL PLASTICITY AND BEHAVIORAL ADAPTATION TO CHRONIC PRISM EXPOSURE.	84
FIGURE 4-5. PLOTS OF MEMBRANE POTENTIALS, AND SPIKE TRACES IN A NORMAL NETWORK WHEN PRESENTED WITH UNIMODAL STIMULUS.	92
FIGURE 4-6. RESULTS WITH SYNCHRONOUS AND SPATIALLY COINCIDING AUDIO-VISUAL INPUT TO A NORMAL NETWORK.	93
FIGURE 4-7. MISMATCHED INPUT – POTENTIAL AND DEPOTENTIATION OF SYNAPSES.	95
FIGURE 4-8. POTENTIATION AND DEPOTENTIATION OF SYNAPSES.	97

Chapter 1. Introduction

The average human brain has approximately 10^{11} neurons (Kandel et al., 2000) that are networked following a well-defined connectivity diagram. Each connection between a pair of neurons is called a synapse, and there are on the order of 10^{14} synapses (Shepherd, 1998; Tang et al., 2001). Information is thought to be encoded in the brain in a distributed fashion across these synapses. The encoded information, while stable, is also susceptible to change, or *plasticity*, to adapt to new environments and to learn new information. Two broad categories of neural plasticity can be distinguished based on how the changes are implemented in the brain. If the changes involve modifications to the network topology (or connectivity pattern), they are said to constitute *architectural plasticity*. If there is no change to the connectivity pattern, but the efficacies of existing functional synapses are modified, then there is said to be *synaptic plasticity*. Most forms of architectural plasticity involve structural changes – to spines, axons, dendrites, and neurons (the one exception is the unsilencing of preexisting, non-functional synapses (see Atasoy and Kavalali, 2006; Gasparini et al., 2000; Groc et al., 2006 for reviews). Though structural changes can accompany synaptic plasticity (e.g., changes to size and morphology of spines), there are numerous other, non-structural mechanisms as well that implement synaptic efficacy change.

Whereas synaptic plasticity has been the predominantly studied form of plasticity (Martin and Morris, 2002), neuroscience research also provides evidence for activity-dependent architectural plasticity. Starting at the level of individual spines, in the form of

dendritic spine motility (which includes the addition and elimination of functional spines), through axogenesis, the growth of new axonal branches to aid in the process of spinogenesis, and all the way to a change in the number of neurons, architectural plasticity in neuronal networks manifests itself as a spectrum of change ranging from the subtle to the drastic. In addition to being observed during development, the above mechanisms have been observed in adult brains as well. The most common mechanism of architectural plasticity in the brain appears to be dendritic spine motility. In this thesis, we will study structural plasticity in the brain and, particularly, its role in mediating architectural changes. In the rest of this chapter, will briefly describe the terminology used, review what is known about the different forms of architectural plasticity with an emphasis on spines, and summarize the remainder of the thesis.

1.1 Background

A. Synaptic communication

Neurons communicate with one another through electrical and chemical signals at specialized punctate structures called synapses. Typically, a synapse is formed between the output process (called axon) of one neuron and the input process (called dendrite) of another.¹ Consequently, the axonal terminal is referred to as being *pre-synaptic* and the dendritic terminal, *post-synaptic*, and such a synapse is called axodendritic.² Synapses can also be classified as being electrical or chemical based on the manner in which information is transmitted across them (Kandel et al., 2000).

¹ Each neuron has a single axon, but numerous dendrites. Axons are much thinner than dendrites, which are also studded with spines in many cases.

² Synapses can also be formed between two dendrites (called dendrodendritic), between an axon and the cell body (or soma, and hence called axosomatic), or between two axons (called axo-axonic (Kandel et al., 2000)).

Electrical synapses or gap junctions allow for the direct exchange of ions between neurons, and the resulting ionic current directly couples the electrical activity of one cell to that of the other. At chemical synapses, information is transmitted by the release of chemical factors called neurotransmitters. Neurotransmitters diffuse across the extracellular space connecting the pre- and post-synaptic terminals (called the synaptic cleft), are recognized by specialized proteins called receptors, and result in the opening of ion channels that allow the inward or outward flow of ions from the cell. The resulting ionic currents and post-synaptic voltage changes constitute the received signal. Neurotransmitter molecules are packaged in the pre-synaptic terminal in containers called synaptic vesicles and their release occurs by a process called exocytosis in which the vesicle fuses with the pre-synaptic membrane, opens up (partially or fully), and delivers its contents into the synaptic cleft. Release of neurotransmitter at the pre-synaptic site can be evoked by relatively large electrical spikes called action potentials or can be spontaneous. Finally, based on whether they increase or decrease the activity of the target neuron, synapses can be classified as being either excitatory or inhibitory.³ Excitatory synapses outnumber inhibitory ones (approximately 5:1 in the cat visual cortex (Shepherd and Koch, 1998)) and are usually formed on dendrites, whereas inhibitory synapses are formed on the cell body.⁴

³ More locally, synapses can be defined as excitatory or inhibitory based on the sign of the ionic current (with respect to the resting state of the target cell) at the post-synaptic site.

⁴ Again, there are exceptions. See Kandel et al., 2000; Shepherd and Koch, 1998.

B. Spines

Spines are small morphological specializations that protrude from neuronal dendrites⁵ and were first described by Ramón y Cajal in 1888 in the cerebella of birds (see Bonhoeffer and Yuste, 2002). Most excitatory synapses (>90%) are formed on spines⁶ (Peters et al., 1991), and while some inhibitory synapses can be found on spines as well, typically, an inhibitory axospinal synapse is accompanied by an excitatory synapse on the same spine (Micheva and Beaulieu, 1995; Zito and Svoboda, 2002). Based on the synaptic input they receive, spines trigger different signaling pathways that can result in short-term or long-term synaptic changes. There are estimated to be more than 10^{13} spines in the human brain (Nimchinsky et al., 2002). A hippocampal pyramidal neuron (from rat) imaged live⁷ at 40x using a confocal microscope is shown in Fig. 1-1A, and a close-up of the boxed area is in Fig. 1-1B. Almost all the processes seen are dendrites, and the mushroom-like projections from them are spines. A time-lapse series of images of the boxed area in Fig. 1-1B illustrate that spines are morphologically dynamic (Fig. 1-1C). Cajal's drawings of spines are shown in Fig. 1-1D. Spines usually consist of a head (volume $\sim 0.001\text{--}1\ \mu\text{m}^3$) that is connected to the dendrite by a neck, and spine lengths vary between 0.5 and 2 μm .

⁵ Spines can be found on cell bodies and on initial axonal segments as well.

⁶ In other words, most axodendritic synapses are in fact axospinal.

⁷ The morphology of the neuron is visualized using a fluorescent protein (GFP) tagged to a cytoskeletal element called actin, which is known to be enriched in spines.

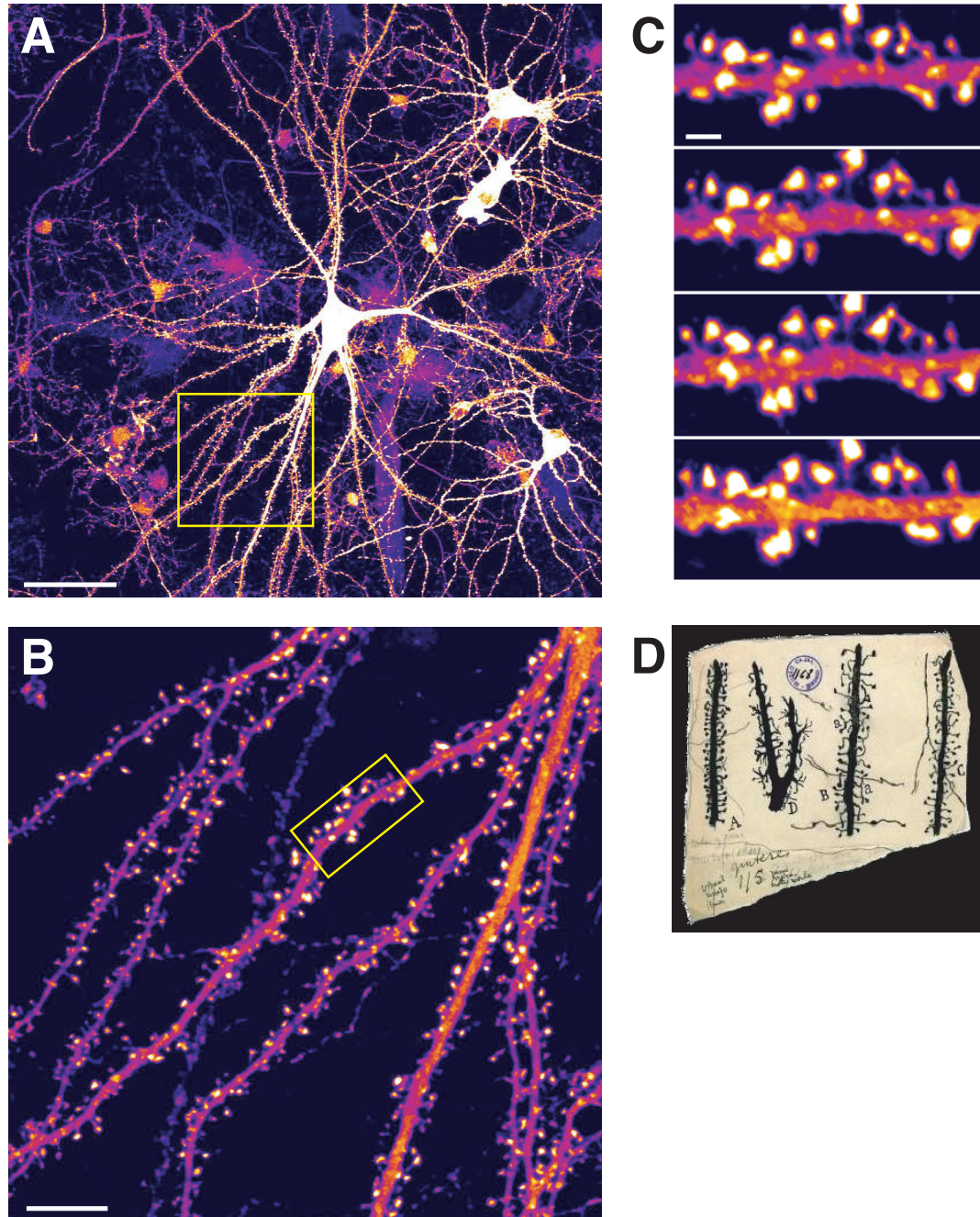


Figure 1-1. Representative pyramidal neuron from rat hippocampus showing numerous dendritic spines.

(A) A hippocampal pyramidal neuron overexpressing GFP-actin⁸ virus and imaged at 40x. Scalebar = 50 μm . (B) Zoomed-in view of the boxed area in (A) with a closer view of dendritic spines. Scalebar = 10 μm . (C) Time-lapse images of the dendritic portion

⁸ (E)GFP = (enhanced) green fluorescent protein (Hibbs, 2000; Lippincott-Schwartz and Patterson, 2003; Sullivan and Kay, 1999).

boxed in (B) showing morphological dynamics in dendritic spines. Images are taken once every 5 minutes. Scalebar = 2 μm . (D) Drawings of different types of spines by Cajal circa 1891 (reproduced from Yuste, 2000). In (A)–(C), the intensity of GFP-actin is represented using the “fire” pseudo-coloring scheme from IMAGEJ. In this scheme, an intensity of 0 is represented by the color black, 255 by white, and intermediate intensities by shades of purple and pink.

C. Classification of spines

Detailed anatomical studies using electron microscopy have led to the classification of dendritic protrusions into five types (Harris et al., 1992; Peters and Kaiserman-Abramof, 1970): Type I are called stubby spines; Type II, mushroom-shaped spines; Type III, thin spines; Type IV, filopodia; and Type V are called cup-shaped spines. Fig. 1-2A shows a schematic representation of these five types. If L , d_h , and d_n , denote the spine length, head diameter and neck diameter, respectively, the rules used to classify spines are: Type I if $L \sim d_n \sim d_h$, Type II if $d_h \gg d_n$, Type III if $L \gg d_n$, and Type IV if $L > 5\mu\text{m}$. Spine lengths are under 2 μm , while filopodia can be up to 10 μm . Filopodia are also very thin and are sometimes called headless spines. As we will see below, due to spine morphological dynamics in live neurons (Dailey and Smith, 1996), and the transitions observed in spine shapes (Dunaevsky et al., 1999; Maletic-Savatic et al., 1999; Parnass et al., 2000), the morphological label of a spine is dynamic as well.

D. Composition of spines

The subcellular composition of different kinds of spines (and filopodia) is diverse (Hering and Sheng, 2001). Of the various components in spines, three are of most interest to our discussion. They are actin (filamentous cytoskeletal element), an electron-dense macromolecular complex of proteins called the post-synaptic density (PSD), and polyribosomes (machinery that translates mRNA to produce proteins). Fig. 1-2B shows

these and other components subcellular components. The presence of actin in spines was determined early on (Fifkova and Delay, 1982) and its critical role in spine dynamics established (Fischer et al., 1998; Matus, 2000). Actin polymerization serves as the end effector that physically produces spine morphological changes. The PSD is perhaps the most important functional organelle in spines as it contains PSD95 (a major component that has been the subject of intense study (see Kennedy, 2000), and various neurotransmitter receptors, and communicates with several intracellular signaling mechanisms.⁹ Typically, it occupies about 10% of the area of the spine (Hering and Sheng, 2001). Polyribosomes are generally found at the base of spines. Various reviews discuss the structure and components of spines in detail (Hering and Sheng, 2001; Sorra and Harris, 2000).

⁹ Given the post-synaptic role of spines, the importance of PSD is not surprising. Though not all spines actually have synapses on them (Sotelo, 1990), although most do. Also, synapses have been found on filopodia as well (Fiala et al., 1998).

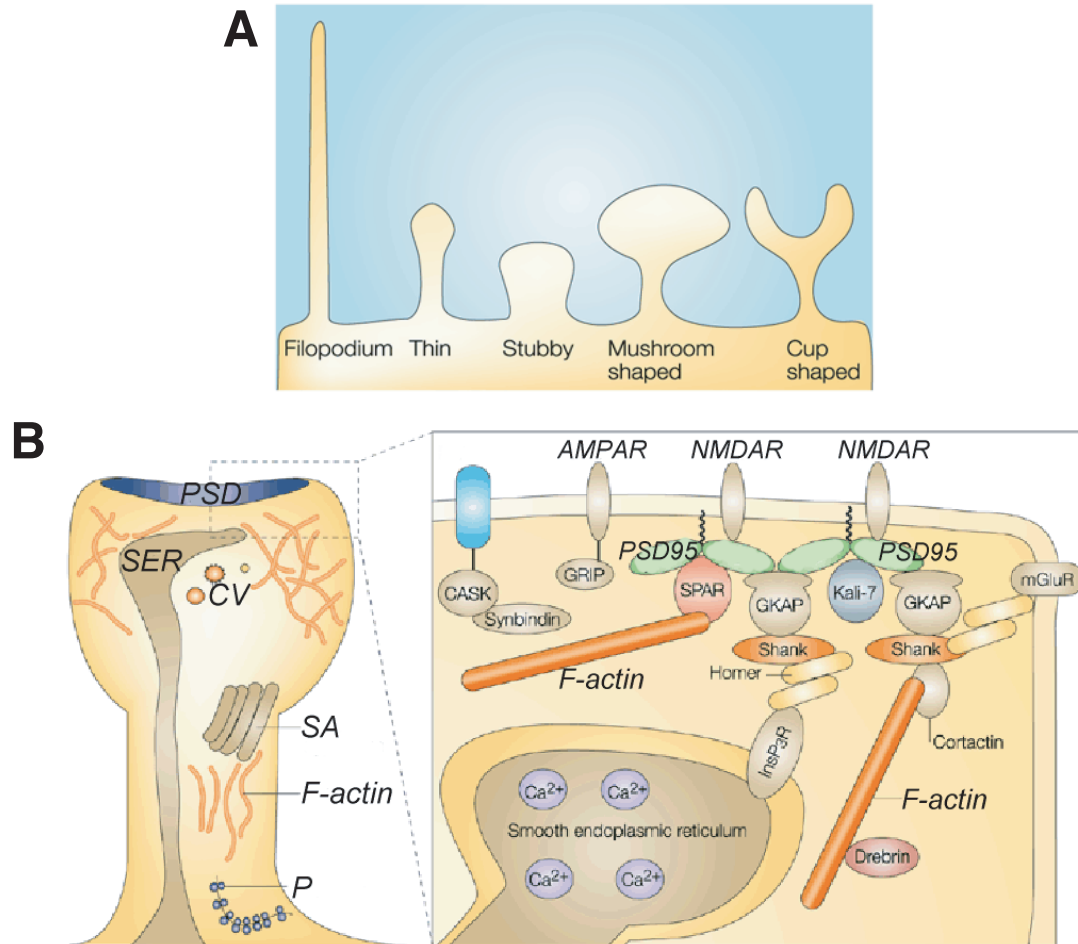


Figure 1-2. Morphological classification and subcellular composition of dendritic spines.

(A) Morphological spine types: stubby spines (Type I), mushroom spines (Type II), thin spines (Type III), filopodia (Type IV) and cup-shaped spines (Type V) (adapted from Hering and Sheng, 2001). (B) Morphological classification of spines. PSD – post-synaptic density, P – polyribosomes, SA – spine apparatus, SER – smooth endoplasmic reticulum (adapted from Hering and Sheng, 2001).

1.2 Structural mechanisms of architectural plasticity

A. Spine motility

Rapid morphological plasticity of spines, spine movement, and their growth and retraction are collectively referred to as spine motility or spine morphological dynamics. Motility was found to occur spontaneously in hippocampal neurons in slice cultures from

rats (Dailey and Smith, 1996; Fischer et al., 1998). Since its discovery, one of the main functions attributed to motility is that of exploring the extracellular space in search of pre-synaptic partners (but also see Dunaevsky et al., 2001). Other attributed functions are the modulation of biochemical signaling and protein scaffolding (Halpain, 2000). Motility has also been found in response to electrical stimulation of neurons (Maletic-Savatic et al., 1999), thus suggesting that experience may regulate motility. Direct evidence for this is available from several studies in which sensory deprivation of different kinds (tactile and visual) resulted in changes in spine dynamics, including effects on synapse turnover (Grutzendler et al., 2002; Holtmaat et al., 2006; Holtmaat et al., 2005; Lendvai et al., 2000; Majewska and Sur, 2003; Mizrahi and Katz, 2003; Trachtenberg et al., 2002; Zuo et al., 2005). These data, along with theoretical interpretations (Chklovskii et al., 2004; Poirazi and Mel, 2001; Stepanyants and Chklovskii, 2005) are strong evidence for spine dynamics as a potential mechanism driving architectural plasticity.

B. Changes in spine density and synapse number

While the above studies looked directly at movement and morphological changes as they occurred, other studies have looked at the effects of motility indirectly by comparing the density of spines and their morphological distribution between control and learning conditions. In a trace eye-blink conditioning task in rats, it was found that the density of spines in the basal CA1 dendrites of the hippocampus – an area that is known to be important for encoding such memories – was greater after conditioning (Leuner et al., 2003). Interestingly, when the acquisition of this association was blocked using a pharmacological agent that interferes with the formation of long-term memories, this

spine density increase was blocked as well. Spatial training of rats, which is known to produce an increase in their subsequent ability to learn in spatial tasks, also produces an increase in the density of spines in the hippocampus (Moser et al., 1997). Other tasks like odor discrimination training (Knafo et al., 2001), visual stimulation, and even space flight (Yuste and Bonhoeffer, 2001), have been found to produce spine density increases in the appropriate brain regions in rats. A case can thus be made that experience-dependent plasticity in dendritic spines may facilitate architectural reorganization of neural circuits in response to functional demands.

In addition to the studies that have examined spine changes, other studies have looked directly at changes in synapse number in response to learning. For instance, Chang and colleagues (Chang et al., 1991) showed that long-term potentiation, a cellular model of learning, increased synaptic numbers in two-year-old rats *in vitro*. Other studies report an increase in the cerebellar synapse density in rats following classical eye-blink conditioning experiments (Black et al., 1990; Kleim et al., 2002), and synaptogenesis in the hippocampus following spatial training of rats in the Morris water maze task, a classic spatial learning experiment (Ramirez-Amaya et al., 1999). Such results are not restricted to rodents (for instance, see Stewart and Rusakov, 1995, for similar effects in chicks). Experimental evidence for direct sensory-stimulus-dependent synapse formation in adult animals was first reported in rodent whisker barrels, where it was shown that localized increases in both synapse number (35%) and spine density (25%) followed specific whisker stimulation (Knott et al., 2002; Zito and Svoboda, 2002). Thus, several lines of evidence establish the occurrence of synaptogenesis, and potentially architectural

changes, in adult neuronal tissue following physiologically relevant stimuli and learning paradigms.

C. Neurogenesis

In traditional neuroscience, the idea that neurons may be added continually after birth was not considered seriously (Gross, 2000). Since the early 1960s, this view began to gradually change when Altman and colleagues (Altman, 1962; Altman and Das, 1965) showed evidence for new neurons in several brain regions of adult rats (neocortex, olfactory bulb, dentate gyrus), and cats (neocortex). Since then, evidence for neurogenesis has accumulated in adult songbirds (Goldman and Nottebohm, 1983; Nottebohm, 1985; Paton and Nottebohm, 1984), the dentate gyrus of rats (Stanfield and Trice, 1988), adult mouse hippocampus (Kempermann et al., 1997), and the dentate gyrus and olfactory bulb of macaque monkeys (Kornack and Rakic, 1999). Recent studies have even reported the addition of new neurons in the neocortex of macaque monkeys throughout adulthood (Gould et al., 1999). The results in the neocortex are still controversial since some researchers have expressed doubt about them based on objections to the techniques used to establish neurogenesis (Nowakowski and Hayes, 2000; Rakic, 2002). In humans, it has been found that new neurons are added in the dentate gyrus (Eriksson et al., 1998), but not the olfactory bulb (Sanai et al., 2004). The latter study points to the presence of a substantial number of adult neural stem cells – cells that can potentially generate neurons – in a region of the forebrain called the subventricular zone, that intriguingly appear not to produce neurons in the adult human brain. The above evidence indicates that neurons are indeed added to adult neuronal circuits, although this addition appears to be less prevalent in humans.

Neurogenesis, like synaptogenesis and spine density changes, has been correlated with learning experiences. For instance, trace eye-blink conditioning and spatial learning in animals lead to an increase in the number of hippocampal neurons through an extension of neuronal lifetimes (Gould et al., 1999). There appears to be a critical period following cell production such that learning occurring in this period increases neuronal lifespan. In parallel, stressful experiences that result in a downregulation of cell proliferation in the dentate gyrus (Gould and Gross, 2002) are implicated in lower performance in hippocampally dependent learning tasks, suggesting a causal link between the two. Several conditions that increase neurogenesis (enriched environments, increased estrogen levels, wheel running, etc.) in mice and rats also enhance performance (Gould and Gross, 2002). Similarly, increases in social complexity have been found to enhance the survival of new neurons in birds (Lipkind et al., 2002). Finally, it has been found that the physiological properties of adult-generated granule cells in the dentate gyrus of the hippocampus resemble those of granule cells in young rats (Overstreet-Wadiche et al., 2006). This suggests that adult-generated neurons may share some properties with embryonic and early post-natal neurons in their ability to extend axons, form new connections more readily, and make more synapses. These characteristics may make adult neurogenesis an attractive “feature,” rather than a developmental “bug” in neuronal circuits.

In summary, there is now a large body of evidence that suggests that spine motility, spinogenesis, synaptogenesis, and, more recently, neurogenesis are all active mechanisms for implementing architectural plasticity in neuronal circuits in response to real learning and memory needs faced by organisms.

1.3 Architectural plasticity and representation construction

Formal learning theory. Formal learning theory (FLT) deals with the ability of a learner to arrive at a target concept based on examples of the concept. Three typical features of FLT models are that the learning algorithm searches through a predefined space of candidate hypotheses (concepts), it is expected to learn the concept exactly, and no restrictions are placed on the actual time taken by the learner to arrive at the target concept. FLT is therefore interested in “exact” and “in-principle” learnability, and the expectation is that generalization – a measure of performance on novel examples – is achieved. The classical formulation of FLT is discussed in the context of language learning by Gold (Gold, 1967). The key insight from formal work on language learning is that the learner must utilize a highly restricted set of all possible concepts in order to have even the possibility of generalizing. In other words, far from employing a general learner, from this perspective a language learning system must be meticulously tailored to the problem at hand, either by the designer in the case of artificial systems, or presumably by evolution in the case of biological learners.

PAC learning. In the early 1980s, formal learning theory underwent a substantial change from Gold’s limit-based framework to a model of PAC learning (probably-approximately-correct learning, (Valiant, 1984)). The PAC model relaxes two of the three key requirements of formal learning theory. The impractical assumption of infinite time horizons is eliminated and the stringent restriction of exact learning relaxed. In short, PAC learning deals not with in-principle learnability, but with learnability in polynomial time, and not with exact learning, but with approximate learning. Formally, a concept is PAC-learnable if the learner arrives with probability $1-\delta$ at a hypothesis that classifies all

the examples correctly with probability $1-\epsilon$, for arbitrarily small ϵ and δ . Nevertheless, the hypothesis space is still fixed a priori. A fixed hypothesis space yields such problematic theoretical issues as Fodor's paradox (Fodor, 1980), which states that nothing can be learned that is not already known; hence nothing is really learned. The idea here is that no hypothesis that is more complex than the ones in the given hypothesis space can be evaluated and hence learned. Therefore, all concepts need to be available in the hypothesis space before the search begins.

Constructive learning and architectural plasticity. Constructive learning (Piaget, 1970; Piaget, 1980; Quartz, 1993; Quartz and Sejnowski, 1997) addresses this issue of a fixed hypothesis space. The central idea of Piagetian constructivism is the construction of more complex hypotheses from simpler ones. This issue is dealt with more formally by Quartz (Quartz, 1993; Quartz and Sejnowski, 1997). Constructivist learning models deal directly with the issue of increasing hypothesis complexity as learning progresses (Shultz et al., 1995; Westermann, 2000). Activity-dependent architectural plasticity can be viewed as a mechanism that implements constructivist learning. Constructive neural networks offer a clear way of viewing learning and development as constituting a “plasticity continuum.” Synaptic weight change may be a form of plasticity that occurs at fast timescales, whereas architectural changes occur on slower timescales. Further, all evidence suggests that many of the developmental processes of structural plasticity underlie learning in mature animals.

Baum (Baum, 1988) showed that networks with the ability to add structure during the process of learning are capable of learning in polynomial time any learning problem that can be solved in polynomial time by any algorithm whatsoever (Quartz and

Sejnowski, 1997), thus conferring a computational universality to this paradigm. Interestingly the bias-variance tradeoff (Geman et al., 1992), can be broken by constructivist learning, by adding hypotheses incrementally to the space in such a way as to keep variance low while reducing bias. Further, in the context of neurobiology, the burden of innate knowledge is relaxed. Given a basic set of primitives (in the form of mechanisms and physical substrate), construction of a network occurs under the guidance of experience within genetic constraints. Finally computational arguments show that it is unlikely that evolution has prepared brain networks in human children for all of the various learning problems to which they might eventually be exposed (Sirois and Shultz, 1999). It is far more likely that brain networks will need to be constructed and their architectures modified as novel as unexpected learning problems arise.

1.4 Summary of the remainder of the thesis

In the remainder of this thesis, we first describe a novel and unified scheme for characterizing dendritic spine dynamics (chapter 2). We then investigate the effects of disrupting structural constraints at synapses on spine dynamics and show that early structural changes can predict later, more drastic ones that may be involved in architectural plasticity (chapter 3). With computational modeling, we then provide an explanation for how environmental pressures can mediate behavioral adaptation in barn owls via architectural plasticity (chapter 4). We also discuss explicitly the extra power that architectural plasticity accords a neuronal network, when compared to just synaptic plasticity. We end with a discussion of all the results (chapter 5). Detailed summaries of chapters 2, 3, and 4 are below.

A. Characterization of spine motility

Dendritic spines display an astonishingly wide variety of structural changes. No methodology exists in the literature to approach these changes in a systematic manner, to quantify various forms of motility in hundreds of spines, and to compare their behavior across treatments. In this chapter, we propose a unified scheme for characterizing spine motility that is robust with respect to various sources of noise.

B. Regulation of spine dynamics and synaptic function by N-cadherin.

Structural changes at synapses are thought to be a key mechanism for the encoding of memories in the brain. Recent studies have shown that the growth and retraction of dendritic spines, the sites of excitatory synapses, accompany bidirectional changes in synaptic plasticity. Little is known, however, about the morphological changes that lead up to spine loss and synapse elimination. Also, though spine dynamics have been studied separately at timescales from seconds to days, the relationship between structural changes at different timescales is unknown. Here, we examine the progression of structural changes that culminate in spine elimination by acutely disrupting the synaptic adhesion molecule, N-cadherin, in mature synapses of cultured hippocampal neurons. We show that morphological dynamics in the same spines are independently modulated at two different timescales (“fast” – minutes, and “slow” – hours) and that N-cadherin disruption induces spine loss. We demonstrate for the first time that earlier structural changes induced by N-cadherin disruption, namely enhanced motility and reduced length, are predictive of later spine fate – spines with the former changes are significantly more likely to be subsequently lost. We also uncover some of the intracellular responses and biochemical mechanisms that accompany effects. Our results provide insight into the moment-to-moment regulation of synaptic architecture by N-

cadherin. Furthermore, we show that subtle changes in the stochastic dynamics of spines reveal the structural precursors of synapse elimination, thereby suggesting that some forms of morphological dynamics may be potential readouts for subsequent rewiring in neuronal networks.

C. Modeling architectural plasticity in the auditory localization system of barn owls

Auditory localization behavior in barn owls is mediated by the integration of topographically encoded visual and auditory space maps. In juvenile owls, disruption of the audio-visual map alignment by the application of glasses that laterally shift the visual input results in behavioral adaptation over the course of several weeks. It has been reported in literature that this adaptation is produced by architectural plasticity in the neural circuits encoding the space maps. It is known that this plasticity is guided by visual input in a topographic manner, and that the error signal is embedded in the firing dynamics of neurons in the inferior colliculus. In this work, we use leaky integrate-and-fire neurons to model the key elements in the auditory localization circuit of barn owls. We demonstrate that a Hebbian spike-timing dependent learning rule, coupled with an activity-dependent mechanism that promotes growth, can account for the essentials of circuit-level plasticity associated with prism experience. We point out the importance of inhibition in both the normal functioning of this circuit, and prism-induced plasticity, and comment on potential mechanisms for activity-induced growth.

Chapter 2. Characterization of spine motility

Dendritic spines are highly dynamic structures (Fig. 2-1) and display morphological changes and the movement over timescales from seconds to days. These dynamics are collectively referred to as spine motility and have been the topic of intense research over the past several years. A central issue in studying motility is the development and use of consistent methods to characterize and quantify it. Several methods exist in the literature; however, they have their limitations. Here, we review the state of the art and then present a unified scheme for characterizing spine morphological dynamics. This scheme serves as an assay system that can be used to reliably compare, between treatments, the behavior of large numbers of spines.

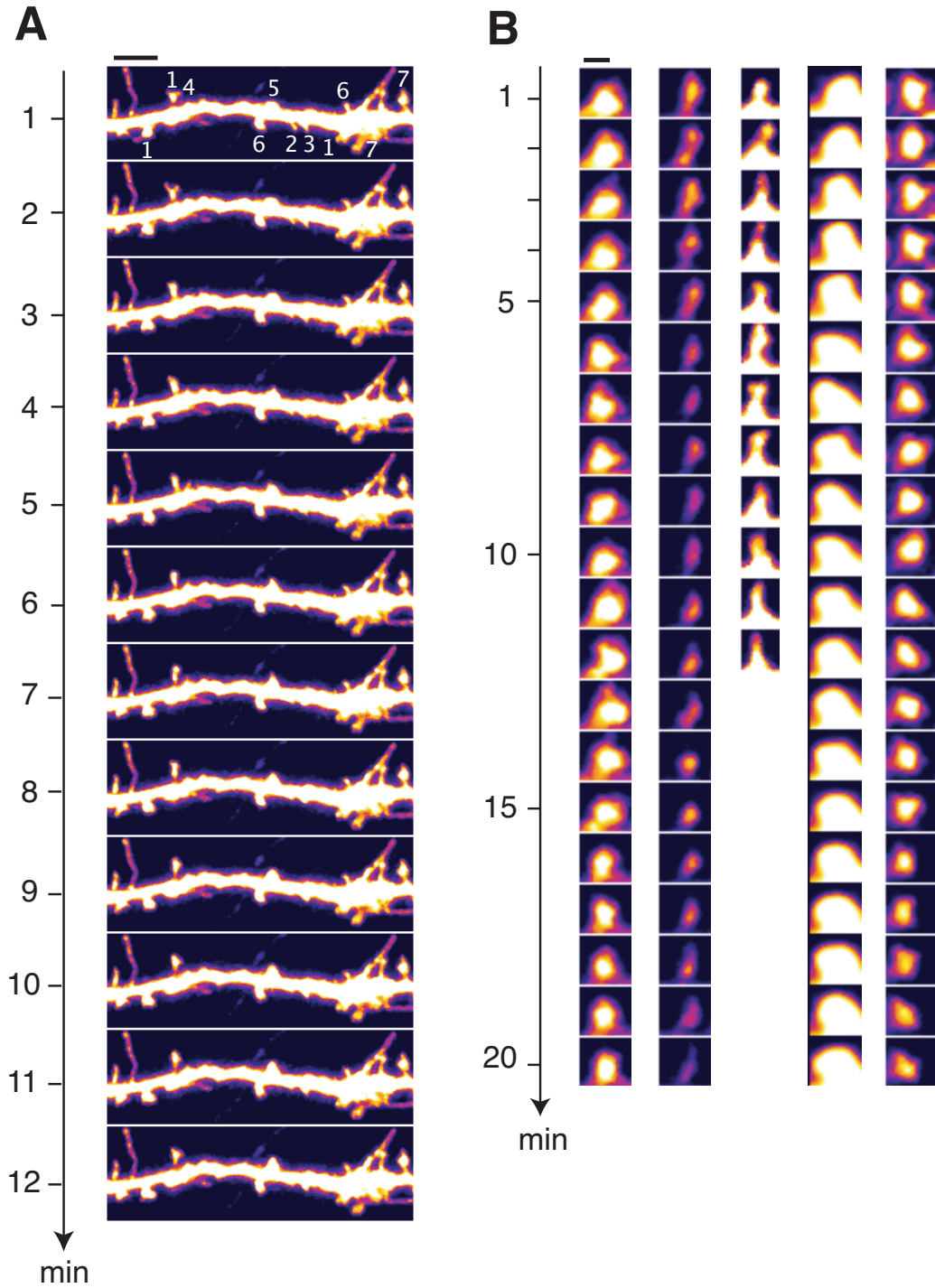


Figure 2-1. Morphological dynamics (“motility”) of dendritic spines.

(A) Time-lapse images of a dendrite expressing EGFP with spines showing different forms of motility: changes in position (1, 5), shape (1, 6), and size (2, 3, 4, including spine loss (2) and gain (4)). Some spines display no discernible changes (7). Scalebar = 2

μm . **(B)** Time-lapse images of five individual spines showing subtle forms of spine motility. Scalebar = 1 μm . All images are acquired once every minute. Intensity of the cell-filling fluorophore EGFP is pseudo-colored with the “fire” look-up table in IMAGEJ.

2.1 Spine quantifiers in the literature

Following is a brief chronological list of methods and measures that have been used in the literature to respectively describe and quantify spines and their motility.

- **>1960.** Various: Calculated spine numbers and densities per unit dendrite length in different studies.
- **1970.** A. Peters and I. R. Kaiserman-Abramov (1970): Classified spines into thin, stubby, and mushroom or cup-shaped.
- **1992.** K. M. Harris’ group (Harris et al., 1992): Pioneered the use of serial electron microscopy to analyze spines based on spine length (L), head diameter (d_h), neck diameter (d_n), and subcellular composition to classify spines into stubby (Type I), mushroom (Type II), and thin (Type III, see chapter 1 for details of classification, and also Harris, 1999; Sorra and Harris, 2000 for their discussion on the subcellular structure of spines).
- **1995.** D. A. Rusakov and M. G. Stewart (1995): Proposed a scheme for automatically determining dendritic and total spine length using 3D reconstructions.
- **1996.** S. J. Smith’s group (Dailey and Smith, 1996): Computed filopodial lengths, and presented time-lapse images. Categorized dynamics by counting the number of spines that were stable, that disappeared, that appeared, and that were transient.
- **1998.** A. Matus’s group (Fischer et al., 1998): Computed spine length and “major” width (largest width in a direction perpendicular to the length). Plotted their ratio for

- individual spines as a function of time. Used the Mann-Whitney U test (for rank sum) to statistically compare spine lengths in live versus fixed tissue.
- **1999.** K. Svoboda's group (Maletic-Savatic et al., 1999): In addition to quantifying the number and density of synapses, computed instantaneous lengths (L_t), and used successive (signed) length differences ($\Delta L_t = L_t - L_{t-1}$) as a measure of spine dynamics.
 - **1999.** R. Yuste's group (Dunaevsky et al., 1999): Proposed a motility index defined as $M = (\text{accumulated area} - \text{smallest area})/\text{average area}$. Used the Mann-Whitney U test (for rank sum) to statistically compare values of the index before and after treatment.
 - **2000.** A. Matus's group (Fischer et al., 2000): Defined shape factor as $S = 4 \cdot \text{area}/\text{perimeter}$, and used it to look at the shape evolution of spine heads. With this they characterized how far spine heads were from being spherical or circular. This was done on a few individual spines.
 - **2001.** M. Sheng's group (Sala et al., 2001): Characterized spine shape with length and major width (largest width in a direction perpendicular to length). Plotted them separately with respect to time and compared cumulative distributions over many spines between neurons of two different ages (7 and 18 days *in vitro*).
 - **2002.** W. B. Lindquist's group (Koh et al., 2002): Presented an automated method for detecting spines, computing their morphological parameters and volumes, and performing shape classification on them from both static and time lapse images. The strength of this work is the development of an automatic detection and classification scheme in 3D.

For motility characterization, most investigators have looked at the time traces of various shape and size quantifiers for individual spines. Statistics have generally been applied only to spine numbers and densities. Large-scale statistical comparisons across many spines, and between more than two conditions, are challenging and have rarely been done. Changes in spine position have not been explicitly and rigorously quantified, and shape quantifiers used thus far in the literature have not been sophisticated. The only exceptions in the above cases have been the work of Dunaevsky et al., 1999, where they present a likely candidate for a unified motility measure¹⁰ and apply statistics on data from 15 spines to distinguish between “before” and “after” conditions, and Svoboda’s group, where they examine several thousand spines to study ongoing spine loss and gain. There is, however, ample scope for further development of motility quantification.

2.2 Unified scheme for characterizing motility – size, position, timescale, and shape

We propose that a unified view of spine motility can be obtained by considering changes in four independent dimensions, namely – size, position, timescale, and shape (Fig. 2-2A). We quantify size by the area or volume, position by the center-of-mass, timescales by imaging spines at sampling rates ranging from seconds to days, and shape using elliptic Fourier functions (EFFs) (Fig. 2-2A). Both the use of center-of-mass to describe instantaneous spine position and the use of EFFs are novel techniques in the spine motility field. In theory, changes can occur to a structure along any one of these dimensions independently of the others. In experiments, changes occur in more than one

¹⁰ The authors refer to this measure as the motility index. An interesting application for it is in quantifying changes in position and movement that occur between two or more spines. For examples of such motility, and the first explicit discussion of this issue, see Dunaevsky et al., 1999.

of these factors simultaneously and the net result is motility.¹¹ Below, we systematically describe how we acquire data, how we quantify various forms of motility, and how we compare data from spine populations; these steps are summarized in (Fig. 2-2B). Each of these steps is optimized to draw reliable conclusions from large numbers of spines.

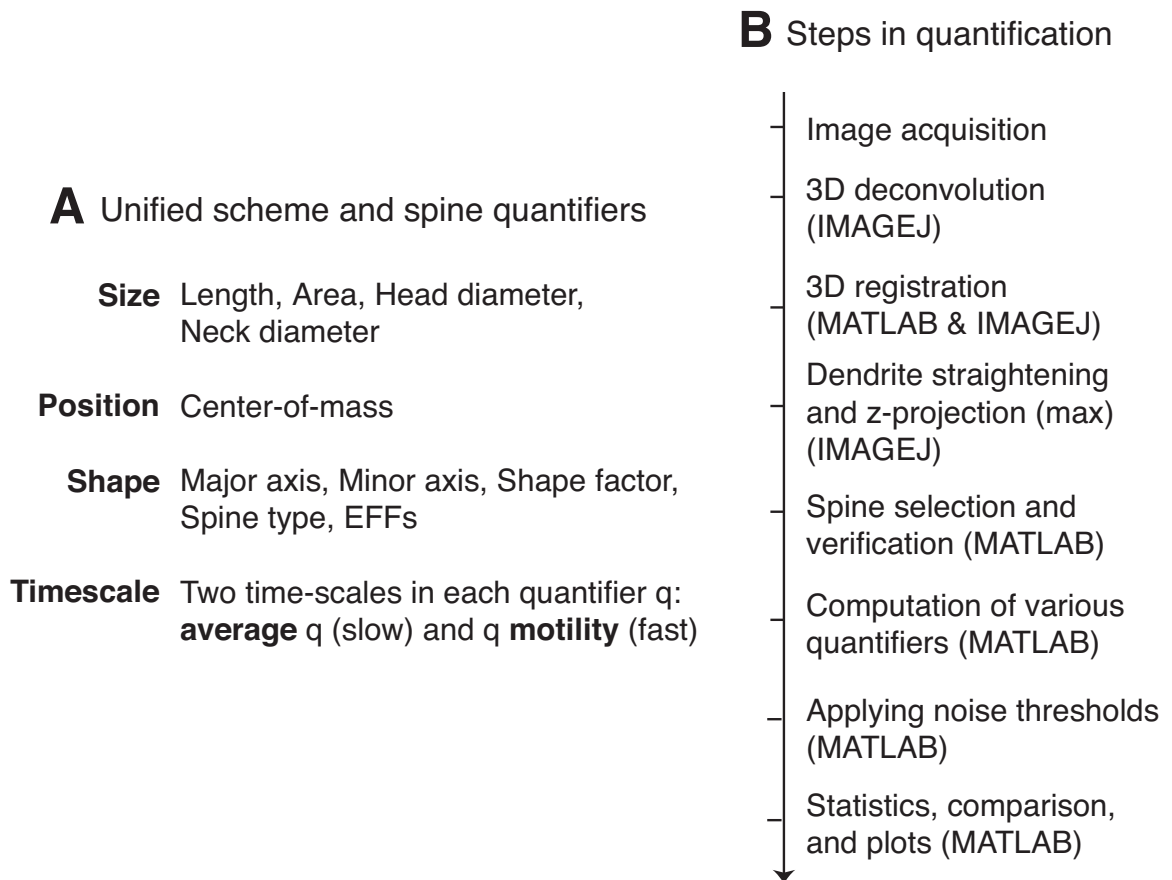


Figure 2-2. Unified scheme and summary of steps for characterizing spine motility.

(**A**) Unified scheme for spine motility quantification, and list of individual quantifiers in each spine motility “dimension.” (**B**) Summary of steps for characterizing spine motility from time-lapse images.

¹¹ Note that elongation, shrinking, genesis, and retraction of spines are just expressions (combinations) of these three dimensions.

A. Preprocessing: live imaging to spine verification

Imaging, deconvolution, and registration. Time-lapse images of neurons overexpressing EGFP were acquired as z-stacks on an inverted LSM 510 Meta (Zeiss) microscope. Image stacks were 3D deconvolved in IMAGEJ (NIH, “Iterative Deconvolve 3D” plugin (Dougherty, 2005)) using a theoretical estimate of the 3D PSF (IMAGEJ, “Diffraction PSF 3D” plugin). No further filtering was performed. Stacks at all time-points were registered to the first stack. The z-projection (maximum) of the stack at each time-point was obtained, and from this, dendrites were straightened in IMAGEJ. The images at this stage are referred to as *raw* images in the text.

Spine selection and verification. For spine *selection* purposes, custom code written in MATLAB (The Mathworks Inc.) was used that combined these raw images into a single stack. The resulting image is referred to as the *t-projection* below. The code then allowed the user to interactively draw individual boxes around each purported spine. All dendritic protrusions in the imaged field of view that resembled spines were selected, thereby minimizing bias. Using the t-projection for this purpose facilitated the selection of those spines as well that were not present at all the time-points. The coordinates of each purported spine’s box were used to extract time-lapse spine images from the raw images. These were used to *verify* visually whether or not the selected protrusion was a spine, and only those spines were accepted for further analysis for which the contributions of extra-spinal sources of movement (like movement of the dendrite due to changes in dendritic position over time, or movement of the entire cell due to experimental errors in the positioning of the dish on the microscope) were minimal. The confounding effects of any residual extra-spinal movement on “real” spine motility were

corrected for using appropriate noise thresholds as discussed below. The verified spines were then rotated appropriately to achieve vertical orientation.

B. Acquisition protocol

Although spine dynamics have been studied separately at different timescales by researchers, these different timescales have not been studied simultaneously, and therefore, the relationship between changes at different scales is unknown. In order to address this, we designed an image acquisition protocol (Fig. 2-3A) to acquire spine images at two different timescales. Each acquisition “time-point” consisted of five z-stacks imaged once every minute with a confocal microscope, representing the fast timescale, and time-points themselves were acquired hours apart, representing the slow timescale (Fig. 2-3A).

C. Size, position, and shape

After preprocessing the images, selecting and verifying spines, we not only monitored spine loss and gain (Fig. 2-3B), but also computed several spine quantifiers (covering the three dimensions of size, position, and shape) like length, area, center-of-mass, spine type, major axis, head diameter (minor axis) for each spine at each instant using custom codes in MATLAB. The use of EFFs for shape quantification is described in section F below. For these above calculations, thresholded images were used so that the confounding effects of EGFP intensity distributions on estimating spine morphology were minimized. Thresholds were automatically determined using a modified Otsu’s method. The instantaneous centerline (“backbone”) of a spine was estimated from the thresholded image by successively computing the midpoint of all non-zero pixels in each horizontal line, from the bottom of the vertical spine image, to the top. Instantaneous

spine length (L_t) was calculated as the arc length of this centerline. The instantaneous center-of-mass was calculated as $\mathbf{x}(t) = (x_c(t), y_c(t)) = (\sum_{i=1}^{N(t)} x_i(t)/N(t), \sum_{i=1}^{N(t)} y_i(t)/N(t))$, where $(x_i(t), y_i(t))$ are the positions of all non-zero pixels in the thresholded spine image at time t and $N(t)$ is the total number of non-zero pixels at that time.

D. Two timescales in each quantifier

We then characterized fast and slow dynamics of each spine morphological quantifier. Slow timescale dynamics were evaluated for each quantifier (for instance spine length) was calculated as the *average* value of that quantifier (*average* length) over the five samples within each time-point. Fast timescale dynamics in a quantifier was computed as the sum over the five samples of the absolute value of the successive differences in the quantifier. For instance, length motility at each time-point was calculated as $\sum_{t=2}^5 (L_t - L_{t-1})$, and center-of-mass *motility* within each time-point is calculated as $\sum_{t=2}^5 |\mathbf{x}(t) - \mathbf{x}(t-1)|$. Fig. 2-3, C1 and C2 show the fast and slow *length* dynamics in a single spine, referred to as length *motility* and *average* length, respectively.

E. Comparing groups of spines

The diversity in spine dynamics in control neurons, evident even in nearby spines on the same dendrite, makes the reliable detection of experimental effects challenging. We found that comparing the *probabilities* of change between treatment and control was a robust method for detecting treatment effects that are not revealed by comparing population *means*. To this end, for instance, in a group of 10 control spines (Fig. 2-3D1), the probabilities of change in average length (slow length dynamics) are calculated as the fractions of spines that show an increase, no change, or decrease (Fig. 2-3D2) in length with respect to baseline measurements. In subsection F below, we discuss how to

determine what “no change” constitutes, by estimating the contribution of various noise sources to motility characterization.

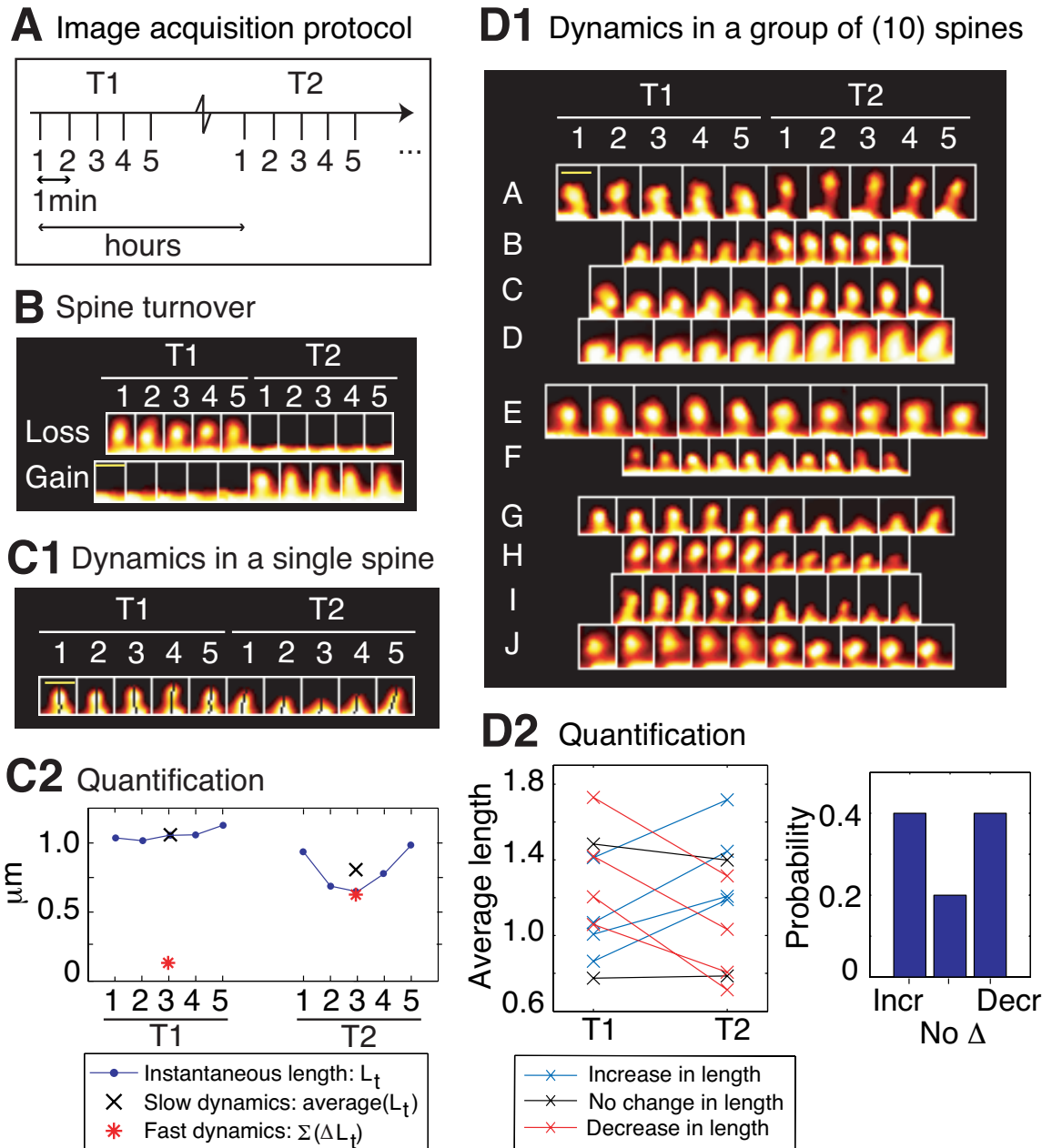


Figure 2-3. Quantifying spine dynamics.

(A) Image acquisition protocol. Each *time-point* (e.g., T1 or T2) consists of five image stacks taken once every minute (*fast* timescale). Different time-points (T1 or T2) are more than an hour apart (*slow* timescale). (B) Time-lapse images of two example spines

from a control neuron that show spine loss (top image) and gain (bottom image), i.e., spine turnover – the most extreme form of spine morphological change. **(C)** Characterizing morphological dynamics in a single spine at the two timescales, with spine length as the example quantifier. **(C1)** Time-lapse images of an example spine from a control neuron acquired at the two time-points. The automated centerline generated to compute spine length at each instant is indicated as a one-pixel-wide black curve (see Methods). **(C2)** Instantaneous length (L_t , blue circles); *slow* length dynamics, or average length (average $\langle L_t \rangle$ within each time-point, black cross); and *fast* length dynamics, or length motility ($\sum |\Delta L_t|$ within each time-point, red asterisk). The spine in (C1) shows a decrease in *average* length (slow timescale), but an increase in length *motility* (fast timescale). **(D)** Characterizing dynamics in a group of spines, with average length (slow length dynamics) as the example quantifier. **(D1)** Time-lapse images of 10 example spines A-J from a control neuron, in which four spines A-D show an increase in average length, two spines E-F show no significant change, and four spines G-J show a decrease, with respect to T1. To determine the magnitude of change in the value of a quantifier that can be considered significant, we have experimentally measured noise thresholds that estimate the extent of change that can occur due to various sources of noise (see Fig. 2-5). **(D2)** (Left panel) Average lengths of spines A-J at the two time-points T1 and T2. (Right panel) Probabilities of change in the average length of spines A-J at time-point T2 with respect to time-point T1, calculated as fractions of spines. In the rest of the paper, dynamics in spine groups are characterized with probabilities, and comparisons between treatment and control are made with respect to these probabilities. All spines in this figure are from control neurons; T1 was the baseline time-point taken before control treatment, and T2 was the time-point 75 minutes after it. Scalebars in yellow = 1 μm .

F. Noise sources – correcting for them or estimating their contributions

Confocal microscopy (see Yuste et al., 2000) is an established tool for high-resolution fluorescent imaging (Fine et al., 1988; Michalet et al., 2003; White et al., 1987). Fluorescence markers have been used for over half a century now, and the ability to target them to specific proteins and specific areas of cells has revolutionized imaging

(see Lippincott-Schwartz and Patterson, 2003; Miyawaki et al., 2003 for reviews). Further, GFP-based fluorescence has been used specifically for spine motility studies in hippocampal tissue since 1998 (Fischer et al., 1998). Nevertheless, specific to spine motility studies, there is potential data contamination by various sources of noise and this needs to be addressed. Noise effects are especially pertinent for our studies given the quantifiers we define and the desire to detect relatively subtle effects. We list below the sources of noise and discuss the means we have implemented to correct for them.

Lens-induced blurring. Any image obtained through a set of lenses results in a blurred image due to diffraction effects. This increases the sensitivity to noise and decreases the effective resolution in all three spatial directions. To correct for this, 3D deconvolution was performed during preprocessing, as described above.

Spurious movement. As we are interested in the fine movements of small structures in neural tissue, any extraneous, or large-scale, movement of either the dish itself, or of dendritic processes, is a source of error. We minimized dish movement during imaging by securing the dish on the microscope stage with fixtures. Dish movement and movement of dendritic processes between time-points (extraspinal movements) was corrected for to a large extent post-acquisition with 3D image registration and verification as described above. The confounding effects of any residual extra-spinal movement on “real” spine motility were corrected for using an estimated noise threshold that included spurious movement (Fig. 2-4).

GFP diffusion. Since the signal (image) is dependent on the presence of GFP in various parts of the cell, one source of noise is the spontaneous change in the distribution of GFP (due to intracellular diffusion) that has nothing to do with the processes we are

interested in monitoring. We expect that after about 12 hours of viral expression (which is the duration of viral expression in our protocol), macroscopic GFP distributions are stable in the cells. However, ongoing diffusion within tiny compartments like spines can confound quantification, particularly the estimation of fast dynamics. We estimated the contribution of diffusion and residual extra-spinal movement to motility by imaging spines before and after the application of cytochalasin D (Cyt-D), a drug that interferes with actin polymerization and is known to block spine dynamics (Fischer et al., 1998) (Fig. 2-4A). Therefore, any dynamics observed post-Cyt-D provides a reliable estimate of the noise in the quantification of motility.

Spurious change in quantifier value. In order to estimate probabilities of change (as described in subsection E above), we need to know reliably whether or not there was a change. For this, we must estimate the magnitude of change that can occur due to noise. The most likely contributor to spurious change is shot noise. Shot noise occurs when electrons are spontaneously emitted by the photomultiplier tube (PMT) in the absence of real excitation.¹² Thermal effects are the most common cause of shot noise. To estimate the contribution of shot noise alone, we imaged fixed tissue obtained after the fixation and immunostaining of GFP-expressing neurons. Two time-points were taken post-fixation and various quantifiers of fast and slow dynamics were computed at each time-point. The difference between the values of a quantifier at the two time-points for every spine was calculated and the distributions plotted. The 95-percentile value of this distribution was chosen as a reasonable estimate of spurious change in that quantifier.

¹² PMTs transduce photons from the sample that impinge on them to a current representing the intensity.

Fig. 2-4B estimates the noise threshold for change in center-of-mass motility, and Fig. 2-4C, in length motility.

Photobleaching. Finally, photobleaching is a critical issue in fluorescent imaging (see Lippincott-Schwartz et al., 2003). Fluorescent probes work by absorbing light at a particular frequency and emitting light at a lower frequency (Stokes shift, (Hibbs, 2000)). This happens when electrons in the dye molecule are excited to a higher state upon absorption of the excitation spectrum and then emit lower frequency photons as they return to their ground state. Not all the light absorbed by a dye molecule is used to produce fluorescence – there are concomitant heat losses. More importantly, electrons do not always return to the ground state from the excited state. There is a small probability (~0.03) that the energy is used to create chemical reactions which can affect the properties of the dye and render it dull and unable to fluoresce. This is called photobleaching. Although the probability of this interstate conversion is very low, the fluorophore can remain in this unusable state for a long time. Thus there can be a loss of signal. Especially, as we are interested in morphology determination over time, loss of the usable fluorophore due to bleaching can be indistinguishable from the actual shrinkage of a spine. We minimized photobleaching by using low-intensity laser light (0.5%). Further, GFP has a very tight crystal structure with the residues responsible for fluorescing being buried deep in an α -helix surrounded by β -barrels (Hibbs, 2000; Sullivan and Kay, 1999). This structure renders the fluorophore fairly resistant to bleaching.

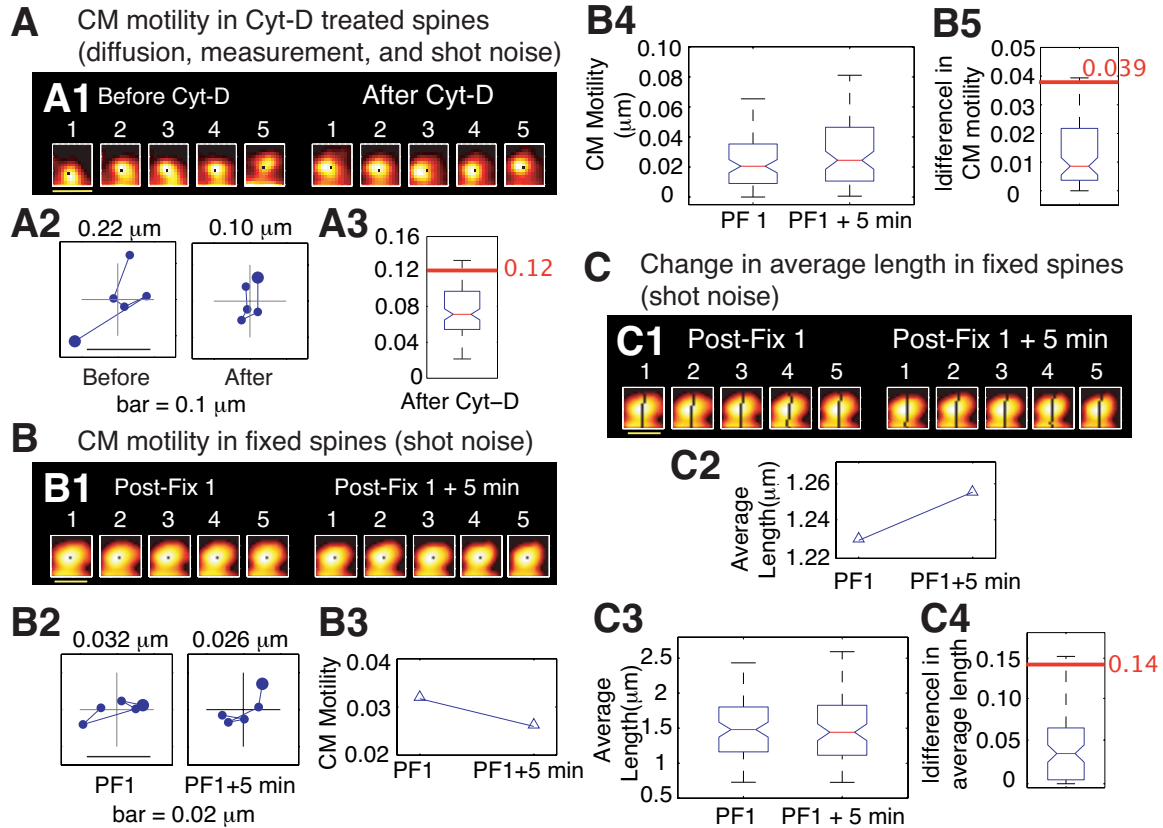


Figure 2-4. Estimating noise-floors.

(A) Estimate of noise in the determination of center-of-mass motility of spines using cytochalasin D. This estimate includes the contribution of any residual, post-registration movement from extra-spinal sources (e.g., dendrite movement, dish movement, etc, see text for details). (A1) Time-lapse images of a representative spine from a neuron expressing EGFP before, and 20 minutes after, treatment with Cyt-D (2 μM). (A2) Each panel shows the locus of successive instantaneous center-of-mass positions over the five minutes within a time-point (after translational normalization to center the locus at the origin). The large dot represents the position of the spine at the first minute within that time-point. The locus in each panel gives a visual indication of the extent to which the spine is motile. The center-of-mass motility value (net movement) of the spine within a time-point is indicated in microns. Cyt-D application causes a reduction in center-of-mass motility, as expected. (A3) Box plot showing the distribution of center-of-mass motility after cytochalasin D treatment ($n=229$ spines). The 95-percentile value in this distribution

(0.12 μm) was chosen as the noise threshold. **(B)** Estimate of spurious *change* in center-of-mass motility (predominantly due to shot noise, see text for details). **(B1)** Time-lapse images of a representative spine at two time-points that are both obtained after fixing neurons expressing EGFP and immunostaining them for EGFP. **(B2)** Loci of the instantaneous center-of-mass positions of the example spine (B1) within each of the two time-points (left and right panels, respectively). The numbers in microns indicate total movement at that time-point. The difference between these two values is small, as expected. **(B3)** Center-of-mass motility of the example spine (B1) at the two time-points. **(B4)** Box plots showing the distributions of center-of-mass motility values at the two time-points after fixation ($n=128$ spines). **(B5)** Box plot of the distribution of the absolute difference between the center-of-mass motility values measured at the two time-points. The 95-percentile value of this distribution (0.039 μm) noise was chosen as the noise threshold for change in center-of-mass motility. **(C)** Estimate of spurious *change* in average length of spines. **(C1)** Time-lapse images of the example spine shown in (B1) with the instantaneous centerlines. **(C2)** Average length of the spine at the two time-points. **(C3)** Box plots showing the distributions of spine average length values at the two time-points after fixation ($n=128$ spines). **(C4)** Box plot of the distribution of the absolute difference between average length values measured at the two time-points. The 95-percentile value of this distribution (0.14 μm) noise was chosen as the noise threshold for change in average length.

G. Advanced shape quantification with EFFs

Determining EFFs from spine image. When Fourier series (Oppenheim et al., 1999) are obtained from the parameterized x and y coordinates of a closed contour, the resulting coefficients are called elliptic Fourier functions (EFFs (Lestrel, 1997; Mysore, 1999; Zahn and Roskies, 1972)). A great advantage of using EFFs is the ability to achieve smooth reconstruction of sampled, polygonal boundaries and to summarize shape with a sparse approximation. In our case, the object whose shape we wish to summarize is a spine, and the pixellated contour of the spine forms the closed boundary that will be

parameterized by arc length along the boundary. If the spatial coordinates of a contour pixel i are (x_i, y_i) , then we can collect all the pixel coordinates as walk along the contour, having started at pixel i_0 and returning to it. The collection of coordinates is now an ordered set, ordered by the parameter arc length, s . The contour can now be described with two piece-wise continuous, parameterized functions: $x_i = u_i(s)$ and $y_i = v_i(s)$, $i=1$ to N . The top-left and top-right panels of each subfigure in Figs. 2-5 (and 2-6) show, respectively, in cyan, $u_i(s)$ and $v_i(s)$ for the spine shown in the bottom-right panel. Fourier series can now be fitted to $x_i = u_i(s)$ and $y_i = v_i(s)$ and the Fourier coefficients (or EFFs) obtained. For each curve u_i and v_i , there are $\sim N+1$ coefficients, corresponding to frequencies ranging from zero to the maximum spatial frequency in the curve.

Using EFFs for spine-shape characterization. With these coefficients, reconstructions with increasingly better accuracies are achieved by using progressively more and more coefficients during the reconstruction process (shown going from Fig. 2-5A to F and Fig. 2-6A to F). Once reconstructed versions of x_i and y_i are obtained, they can be plotted separately (in red, in the top two panels of each sub-figure), or together, showing the reconstructed contour in 2-D (shown in red in the bottom two panels of each sub-figure). If just the first EFF is used, then the resulting 2-D reconstruction will correspond simply to the mean; on the 2-D plane it is a point corresponding to the center of mass (bottom panels in Fig. 2-5A and Fig. 2-6A). As the number of coefficients used is increased, the reconstruction begins to resemble the original contour more. A plot of the error in reconstruction (blue line, root mean squared error between the original contour and the reconstructed contour calculated point by point) as a function of the number of coefficients used is shown in Fig. 2-7 for the two spines previously described.

The horizontal, black dash-dashed line is a threshold for acceptable error (set arbitrarily at 4%). The x-axis is the percentage of coefficients used, and the frequencies included increase with the percentage of coefficients. The yellow, dashed ellipses show differences in the evolution of error, with corresponding differences in the spectral energy (green line). EFFs can be used to summarize shape in many ways. One is by comparing the evolution of the error and energy curves. Another is by using a norm to quantify the difference between the coefficients-vector. A third is to ask what frequencies are represented if only those coefficients which contribute maximally to 90% of the spectral energy, or which result in a 10% error in reconstruction. Thus, either multivariate or univariate EFF summaries can be used to distinguish differences between spine shape over time, or across spines. Here, the spine in Fig. 2-6 has spinules (tiny projections from spine heads), which are represented in higher frequencies. In comparison with the spine in Fig. 2-5, this is evident if we compare the error profiles (Fig. 2-7) – the error reaches the threshold at a higher frequency (greater % of coefficients used) because of an earlier plateau. Such differences can be systematically characterized and subtle changes in spine shape detected by understanding the patterns corresponding to different spine shapes. Noise estimates can be obtained as they have been for other quantifiers thereby separating real shape change from the spurious. We have custom code that automatically outputs EFFs given a gray-scale image of a spine.

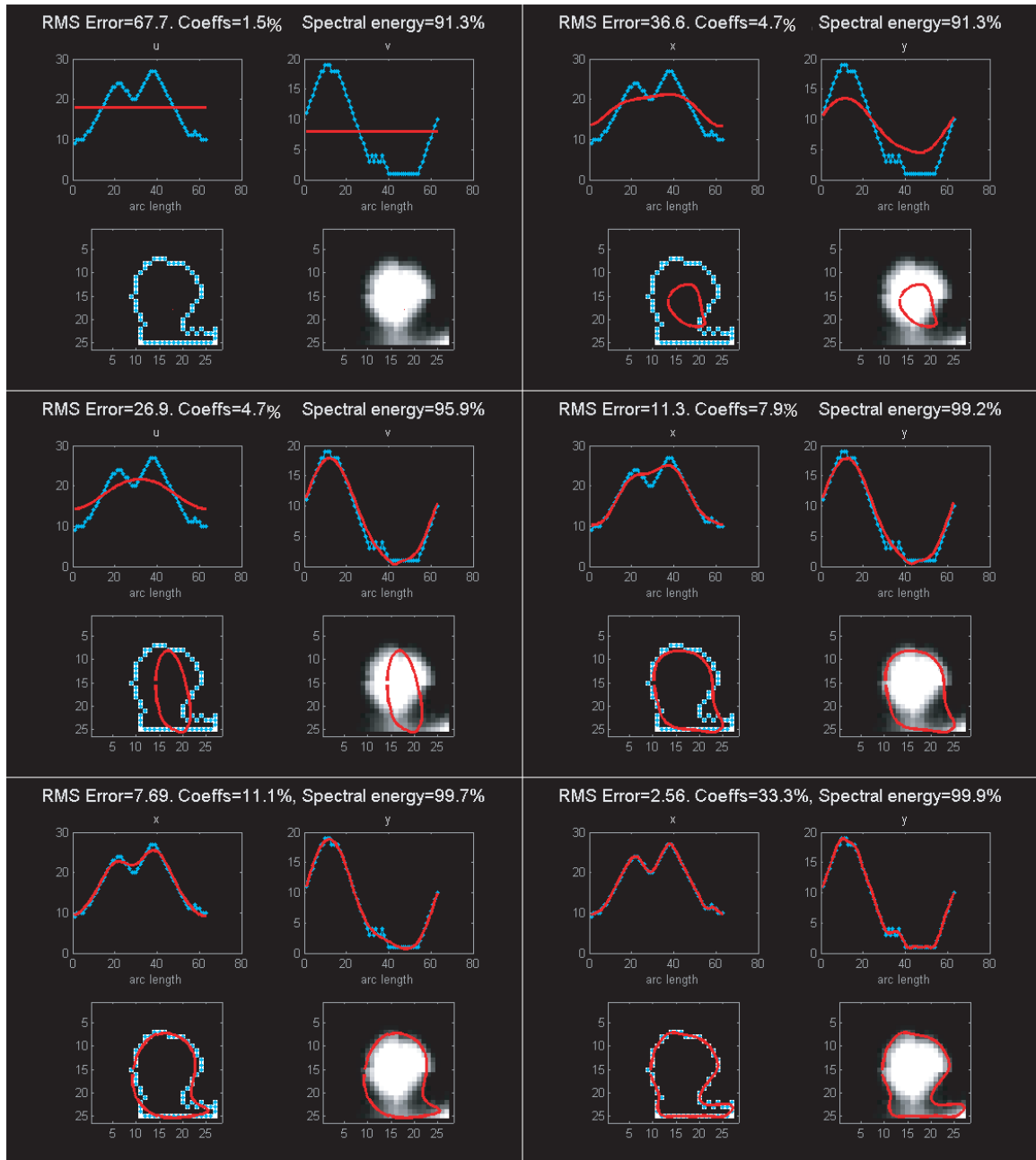


Figure 2-5. Summarizing spine shape with EFFs – example 1.

(A)–(F). In each sub-figure, there are four panels. The bottom-right panel shows a gray-scale image of the spine whose shape is being analyzed. The bottom-left panel shows the contour of the spine as a closed curve in cyan. The contour is obtained from the thresholded version of the gray-scale image. The top two panels show in cyan the x and y coordinates, respectively, of the contour of the spine parameterized by arc length (s). These coordinates ($x = u(s)$ and $y = v(s)$) are obtained by starting at an arbitrary point on

the contour, walking along it at uniform speed, noting the x and y coordinates of every point on the contour, and returning to the starting point. In all four panels, the red lines represented the summarization or reconstructed approximation of the appropriate quantity. The title of each sub-figure indicates the percentage of elliptic Fourier coefficients (of total) used for reconstruction, the percentage of spectral energy contained in these coefficients, and the root mean squared (RMS) error between the actual and the reconstructed quantities. Note that coefficients are included in an ordered fashion starting from those of the lowest frequency to those of the highest.

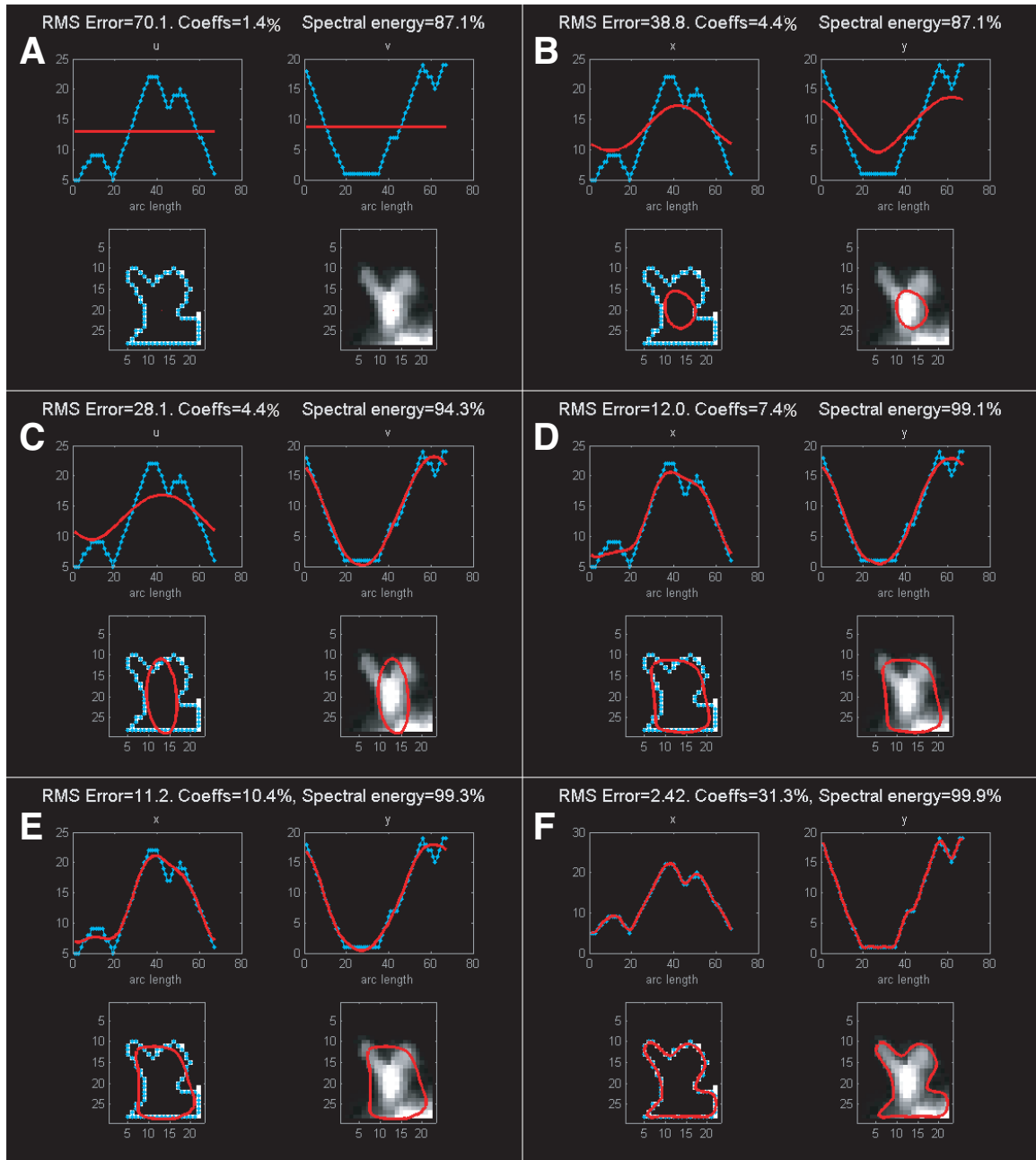


Figure 2-6. Summarizing spine shape with EFFs – example 2.

(A)–(F). As in Fig. 2-5, but for a different spine. This spine has tiny projections called spinules emerging from its head and, as a result, has quite a different morphology from the spine in Fig. 2-5.

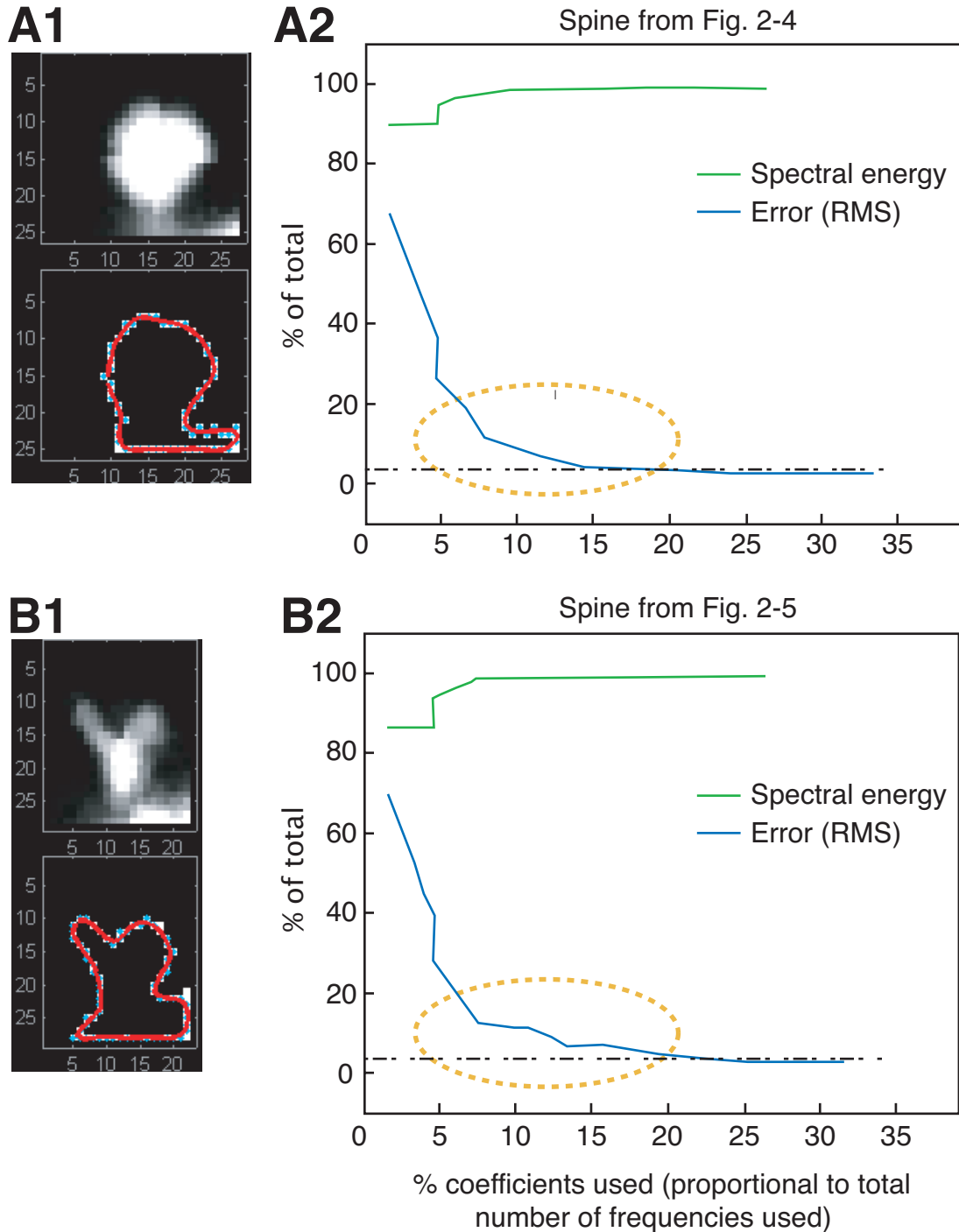


Figure 2-7. Comparing reconstruction errors and EFF frequency spectra of two spines.

(A1) Reproduction of spine shown in Fig. 2-5 along with its reconstructed contour in cyan. (A2) Plotting the cumulative percentage of spectral energy in the EFF coefficients for the spine in A1 (and Fig. 2-5) as the number of coefficients is progressively increased

(green line). The blue line is a corresponding plot in the error (root mean squared, RMS). **(B1)** Reproduction of spine shown in Fig. 2-6 along with its reconstructed contour in cyan. **(B2)** Same as (A2), but for the spine in B1 (and Fig. 2-6). Dash-dashed horizontal lines in A2 and B2 represent an arbitrary threshold (4%) indicating the acceptable error in shape reconstruction. Dashed yellow circles highlight the most visually obvious difference between the RMS error curves for the two spines. Not surprisingly, the spine with spinules (B1, Fig. 2-6) has greater energy content in the higher frequency range as indicated by the fact that the acceptable error threshold is reached more slowly in this case.

2.3 Conclusions

Thus, we calculate the values of various spine quantifiers (e.g., center-of-mass motility and average length values) at each time-point and compare them to the corresponding noise thresholds. The threshold value for real center-of-mass motility was estimated to be $0.12 \mu\text{m}$ (Fig. 2-4A) and that for average length was set to $0.2 \mu\text{m}$. If the calculated values are below their respective thresholds, they are reset to the threshold values.¹³ Quantifier values at each time-point are then compared to baseline, and the nature of change in the value is determined using the noise thresholds for change estimated in Fig. 2-4, B and C. If the observed change for a spine is less than the threshold value ($0.039 \mu\text{m}$ for center-of-mass motility and $0.14 \mu\text{m}$ for length), the spine is considered to have “no-change,” else it is considered to show either an increase or a decrease. Probabilities of change in a quantifier are estimated for each group of 50 spines

¹³ As we are monitoring spines over time, it is possible that the value of a quantifier for any given spine is indistinguishable from noise at some time-points, but is above noise at others. On the one hand it is important to discard only those spines that have quantifier values below noise at *all* time-points. On the other hand, when comparing time-points to determine change in the quantifier, it is also important to ensure that the change is real. This method of resetting quantifier values below the noise threshold to the threshold value allows us to deal consistently with both these issues.

and then these distributions are compared between treatment and control. We also describe a sophisticated spine shape characterization scheme that can detect shape differences. We are thus able to reliably measure gross as well as subtle spine morphological effects above noise.

Chapter 3. Regulation of spine dynamics and synaptic function by N-cadherin

3.1 Introduction

In the face of stable memories, neuronal synapses are in a constant state of flux both biochemically (Inoue and Okabe, 2003; Malinow and Malenka, 2002) and structurally (Dailey and Smith, 1996; Dunaevsky et al., 2001; Holtmaat et al., 2005; Knott et al., 2006; Majewska and Sur, 2003; Trachtenberg et al., 2002; Zuo et al., 2005). Dendritic spines, the post-synaptic sites of most excitatory synapses, show a wide range of morphological changes mediated by the dynamics of the underlying actin cytoskeleton (Fischer et al., 1998). These changes can be described along two general dimensions: (1) timescale – ranging from seconds (Fischer et al., 1998; Korkotian and Segal, 2001) to days (Grutzendler et al., 2002; Holtmaat et al., 2006; Holtmaat et al., 2005; Mizrahi and Katz, 2003; Trachtenberg et al., 2002), and (2) degree – ranging from subtle changes such as in the ruffling of membranes (Fischer et al., 2000; Korkotian and Segal, 2001) to the appearance and disappearance of spines (Engert and Bonhoeffer, 1999; Holtmaat et al., 2006; Maletic-Savatic, 1999; Nagerl et al., 2004; Trachtenberg et al., 2002). The faster and more subtle forms of motility (e.g., head morphing and changes in spine neck size) are thought to regulate calcium compartmentalization (Korkotian and Segal, 2001; Majewska et al., 2000) and protein scaffolding (Dillon and Goda, 2005; Halpain, 2000) and thereby biochemical signaling at the synapse, while the slower and more extreme forms of spine dynamics (e.g., changes in size, appearance and disappearance) are

thought to mediate synaptic and architectural plasticity (Holtmaat et al., 2006; Lang et al., 2004; Matsuzaki et al., 2004; Okamoto et al., 2004; Trachtenberg et al., 2002; Zhou et al., 2004; Zito et al., 2004). Though the contributions of individual molecules to spine morphology have been studied in detail (see Lamprecht and LeDoux, 2004; Tada and Sheng, 2006 for reviews), little is known about whether ongoing structural dynamics provide any information about future changes in the network synaptic structure.

As discussed above, even in control neurons, spines display a wide variety of morphological dynamics. Comparing these ongoing dynamics in control neurons to the effects of a treatment capable of altering them can highlight associations between various forms of spine motility and reveal their regulation. Particularly, the relationships, if any, between changes at different timescales, and any predictive associations therein, can be studied via such comparisons to a stochastic baseline. Towards this end, we hypothesized that interfering with the structural constraints of a synapse (Berardi et al., 2004; Oray et al., 2004), by disrupting synaptic adhesion molecules involved in the maintenance of synaptic structure (Abe et al., 2004; Togashi et al., 2002), would be a direct approach. In particular, we decided to disrupt N-cadherin, a Ca^{2+} -dependent, homophilic, synaptic adhesion molecule (Fannon and Colman, 1996; Redies, 2000; Salinas and Price, 2005; Shimoyama et al., 2000; Takeichi, 1991; Takeichi and Abe, 2005; Uchida, 1996; Wheelock and Johnson, 2003). N-cadherin is implicated in synapse assembly (Benson and Tanaka, 1998; Boggon et al., 2002; Hirano et al., 2003; Jontes et al., 2004; Shapiro, 1999; Togashi et al., 2002), in the formation of synaptic circuits (Redies et al., 1992; Takeichi et al., 1997), and is known to be involved in synaptic plasticity (Benson and Tanaka, 1998; Bozdagi, 2000; Schuman and Murase, 2003; Tanaka, 2000; Tang et al.,

1998) Particularly, the disruption of N-cadherin by the overexpression of a dominant-negative form for 3 days leads to significant changes in spine morphology and synaptic organization (Togashi et al., 2002). Further, the disruption of α N-catenin, a molecule involved in cadherin-mediated adhesion, by gene knockout results in spines that are abnormally motile (Abe et al., 2004). Additionally, N-cadherin is linked to the actin cytoskeleton, the physical effector of motility (Fischer et al., 1998), via intermediary proteins (Hirano, 1992; Ozawa, 1990a), and this linkage is key to its adhesive function (Braga, 2002; Braga, 1997; Fukata and Kaibuchi, 2001; Nagafuchi, 1994). The above evidence suggests that N-cadherin-mediated adhesion can regulate synaptic structure and is therefore a good candidate for the study of spine dynamics. However, exactly what the effects of directly disrupting N-cadherin are on spine dynamics, in mature synapses, and in response to a short-term disruption (as opposed to several days of inhibition), are all unknown.

With this background, we proceed to systematically characterize spine dynamics in the context of direct and acute N-cadherin disruption at mature hippocampal synapses. In addition to investigating the structural consequences, we ask what signaling mechanisms downstream of N-cadherin may be involved in mediating the observed effects.

3.2 Methods

A. Cell culture and infection

Dissociated hippocampal neurons were prepared from post-natal day 2 Sprague-Dawley rat pups and plated at a density of 310-460/mm², as described in Aakalu et al., 2001. Neurons were used following 20-25 days *in vitro*. Twelve hours prior to imaging,

neurons were infected with Sindbis EGFP (in spine dynamics experiments) or Sindbis β -catenin-GFP (in β -catenin dynamics experiments) for 20 minutes and, after a wash, returned to filtered, conditioned growth medium and placed in a 37°C incubator for 10 hours. The growth medium was replaced by HBS (HEPES buffered saline) and allowed to equilibrate for 2 hrs in a 37°C, 5% CO₂ incubator prior to image acquisition.

B. N-cadherin disruption

The 5-mer peptide AHAVD (HAV) is known to interfere with the function of N-cadherin (Chuah et al., 1991; Tang et al., 1998), and its efficacy is enhanced by low extra-cellular Ca²⁺ concentrations (e.g., less than 2 mM) (Tang et al., 1998). We acutely disrupted N-cadherin with a 10 min pulse application of 2 μ M AHAVD (“HAV” peptide) in a zero Ca²⁺ medium containing 1 mM EGTA at 37°C, followed by a wash and replacement of HBS. As control we used a scrambled 5-mer peptide AADHV (“SCR”) at the same concentration. The treatment (or control) was applied after acquisition of baseline images, and at the appropriate time-points further image stacks were acquired.

C. Live imaging

All imaging was performed on an inverted LSM 510 Meta (Zeiss) microscope. Neuronal images were acquired as z-stacks with an oil-immersion objective (Plan Achromat 63x, N.A. 1.4, Zeiss) at a zoom of 2. The x-y-z resolution was 0.07x0.07x0.37 μ m/pixel. Except for the brief periods during image acquisition, neurons were maintained with HBS at 37°C, 5% CO₂ throughout the experiment.

D. Analysis

Preprocessing and analysis was performed as described in detail in chapter 2. Though all the analysis was performed on unfiltered images, for purposes of improved

visualization in the figures, spine images were median (2x2) and mean (2x2) filtered. These images were then pseudo-colored for display so that EGFP intensity in spines was represented with the *hot* colormap in MATLAB in which black corresponds to an intensity of 0, white to 255, and various shades of red and yellow to intermediate intensity values. Data for Figs. 3-1 to 3-4 (relating to the investigation of spine dynamics) are from 690 spines (HAV) and 803 spines (SCR) across three experiments. These spines were segregated randomly into n=14 and n=16, groups respectively, each containing 50 spines. This allowed us a sample size large enough to estimate probabilities but not so large that we would lose statistical power for comparisons. Probabilities of change in a quantifier were estimated for each group of 50 spines and then these distributions were compared between treatment and control. Data for Fig. 3-5 (for β -catenin dynamics experiments) are from 483 spines (HAV) and 465 spines (SCR).

E. Statistical comparisons

All data are plotted as mean \pm SEM. T-tests were used to evaluate the differences between various sampled distributions, and “*” represents significance at $p < 0.05$ for unpaired comparisons (2 groups). Multiple t-tests (> 2 groups) were performed where necessary in all figures after applying a correction for multiple comparisons. Many standard correction schemes exist and, here, we tried two different ones – a conservative Bonferroni approach, and a less conservative, but equally well-accepted, scheme of estimating the false discovery rate (FDR) (Genovese et al., 2002) with an acceptable FDR of 5%. With both approaches, the comparisons that came out as significant were identical. “*” represents significance at $p < 0.05$ after correction. Comparisons that are not significant are not labeled.

F. Electrophysiology

Whole-cell patch-clamp recordings were performed with an Axopatch 200B amplifier on cultured hippocampal neurons bathed in HBS containing in 1 μ M TTX and 20 μ M bicuculline. Whole-cell pipettes (with a resistance of 2.5-5 M Ω) were filled with an internal solution of pH 7.2 containing in mM: 100 cesium gluconate, 0.2 EGTA, 5 MgCl₂, 2 ATP, 0.3 GTP, 40 HEPES. Neurons with pyramidal-like morphology were voltage-clamped at -70 mV, and series resistance was left uncompensated. Membrane parameters and series resistance were monitored at the beginning and end of each recording and only cells with less than 20% change in series resistance were included for analysis. Mini analysis software (Synaptosoft) was used to manually detect minis. The data are from 8-9 neurons in each condition, from 7 independent experiments paired for HAV and SCR treatments.

G. Immunoprecipitation

After the appropriate treatments (HAV or SCR), neuronal cell lysates were precleared overnight with rabbit IgG. They were then incubated for 4 hours with either rabbit anti- β -catenin (Zymed) or rabbit anti-IgG, and with 40 μ L protein-G beads (SIGMA). The beads were spun down, separated from the supernatant, boiled, and then loaded onto 7.5% SDS-PAGE gels. SDS-PAGE was performed at 80 mV for 4 hours. Proteins were transferred overnight to PVDF membranes, and then probed for several proteins successively, with intermediate acid-washing steps when necessary. The data are from three independent experiments.

H. Immunofluorescence

Sample preparation. Neurons were treated with HAV or SCR peptides for 10 minutes, then allowed to recover in conditioned growth medium at 37°C for 30 min, 75 min, or 150 min. They were then antibody live-labeled by first rinsing with ice-cold zero Ca^{2+} HBS containing 1 mM EGTA and incubated on ice for 30 min in mouse anti-surface-N-cadherin antibody (produced and purified in the lab by Dr. Chin-Yin Tai, 1:50 dilution in HBS/0 Ca^{2+} /EGTA). After rinsing, they were fixed with 4% PFA/4% sucrose/PBS-MC on ice for 10 min, permeabilized with 0.1% Triton-X-100/2% BSA /PBS-MC for 10 min, rinsed, blocked in 2% BSA for 20 min, and incubated with rabbit anti-beta-catenin (1:500, Zymed) primary antibody for an hour. Neurons were then incubated in a mixture of goat anti-mouse Alexa 488 (1:1000) and goat anti-rabbit Alexa 546 (1:1000) secondary antibodies for an hour. Cells were lightly fixed again (2% PFA/2% sucrose/PBS-MC) for 5 min. Zenon Alexa Fluor 633 Mouse IgG_{2a} (Invitrogen) was then coupled to mouse anti-bassoon primary antibody following the suggested protocol and cells were incubated in this conjugate for 30 min at room temperature. Prolong gold anti-fade reagent (Invitrogen) was applied to preserve fluorescence for longer periods, and neurons were sealed between glass-slides to ready them for imaging.

Imaging post-fixation. Imaging was done on an inverted LSM 510 Meta (Zeiss) microscope using an oil-immersion objective (Plan Apochromat 63x, N.A. 1.4, Zeiss) at a zoom of 1. Pyramidal neurons were selected based on their surface N-cadherin staining (Benson and Tanaka, 1998), and image z-stacks were acquired in three colors (excitation laser lines– 488 nm, 546 nm, and 633 nm) using multi-track imaging with appropriate filter sets (multi-track imaging minimizes bleed-through across channels, and when we checked each pair of channels, there was no noticeable bleed-through with the acquisition

parameters used). Appropriate filter sets were used for collection. For analysis, dendrites were straightened, 3D deconvolved, and watershed filtered in IMAGEJ to improve puncta separation. These images were then analyzed using custom code written in MATLAB to determine puncta sizes, volumes, and intensities in 3D. Fig. 7 is based on data from 32-46 dendrites for each treatment, at each of the time-points.

I. L-cells aggregation assay

L-cells were transfected with N-cadherin using Lipofectamine 2000 (Invitrogen) and a gentamycin-resistant stable line was created after a month of passaging. L-cells were plated onto 10 cm dishes in DMEM complete and allowed to reach confluency for two to three days. They were then trypsinized, counted, and approximately 500 μL of cell suspension (at $0.95\text{-}1.07 \times 10^6$ cells/100 μL) was used for each of three treatments – 2 μM HAV, or 2 μM SCR, or HBS. After a 10 min incubation at 37°C, they were rinsed with and suspended in DMEM complete. Immediately, 10 μL of cell suspension from each sample was mounted onto slides. This represented time $t=0$. The samples were all placed in a 37°C shaker at 500 rpm. At each of $t=30, 75, 150,$ and 180 min, cell suspensions were plated onto slides as before and imaged in DIC on an inverted LSM 510 Meta (Zeiss) microscope using an air objective (10x Plan-Neofluar, N. A. 0.3, Zeiss) at a zoom of 0.7. The extent of aggregation was quantified (Nguyen and Sudhof, 1997) as N_0/N_t , where N_t was the number of cells not in aggregates at each t . Data are from three independent experiments.

3.3 Results: fast and slow spine dynamics are precursors of spine loss

To study different forms of structural dynamics in dendritic spines and their relationships to one another, we conducted high-resolution time-lapse confocal imaging of hippocampal dendrites and spines before and after the acute disruption of the Ca^{2+} -dependent cell-adhesion molecule, N-cadherin. We hypothesized that interfering with synaptic adhesion (Abe et al., 2004; Togashi et al., 2002) would lead to changes in spine dynamics. This allowed us to examine whether fast spine dynamics, observed within minutes, might predict morphological changes observed over the time course of hours. To address this, we acquired images of spines at two different timescales as described in chapter 2 (Fig. 2-4): the fast timescale was over minutes, and the slow over hours. We have determined the contribution of noise (diffusion, extra-spinal movement, and shot noise) to our measurements (Fig. 2-5) and established that we can detect subtle changes in spine morphological quantifiers above noise.

A. More spines are motile after N-cadherin disruption

As N-cadherin is involved in the structural stability of synapses (Goda, 2002; Takeichi and Abe, 2005), we asked whether disrupting N-cadherin-mediated adhesion would lead to increased spine movement. We perturbed surface N-cadherin with the function-interfering HAV peptide (AHAVD, Chuah et al., 1991; Tang et al., 1998) and then monitored the fast and slow dynamics of individual spines at 75 and 180 min after this treatment. We first examined rapid changes by analyzing the fast center-of-mass dynamics (center-of-mass *motility*) of individual spines (Fig. 3-1). This measure of motility is influenced by lateral and protrusive spine movements and is a general quantifier of positional dynamics in spines. In HAV-treated cells, more spines showed an

increase in center-of-mass motility at 75 min than in control peptide-treated cells (scrambled AADHV peptide, SCR, Fig. 3-1C). Surprisingly, this effect was no longer observed at 180 min. There was no significant difference at baseline between the center-of-mass motility distributions of HAV and SCR spines, and additionally, length *motility* and area *motility* were unaffected by cadherin disruption (data not shown). To check whether the effects on center-of-mass motility observed at 75 min could be due to a preferential effect of HAV on GFP diffusion, we performed fluorescence recovery after photobleaching (FRAP) experiments on GFP-expressing neurons at 75 min after the application of either HAV or SCR (Fig. 3-1D). FRAP experiments help estimate rates of diffusion of a fluorophore (in this case GFP). Since the recovery rates of GFP after HAV or SCR treatments are indistinguishable (Fig. 3-1D2), we can rule out any confounding effects of HAV on GFP diffusion. These results show a preferential regulation of fast center-of-mass dynamics in spines by N-cadherin disruption.

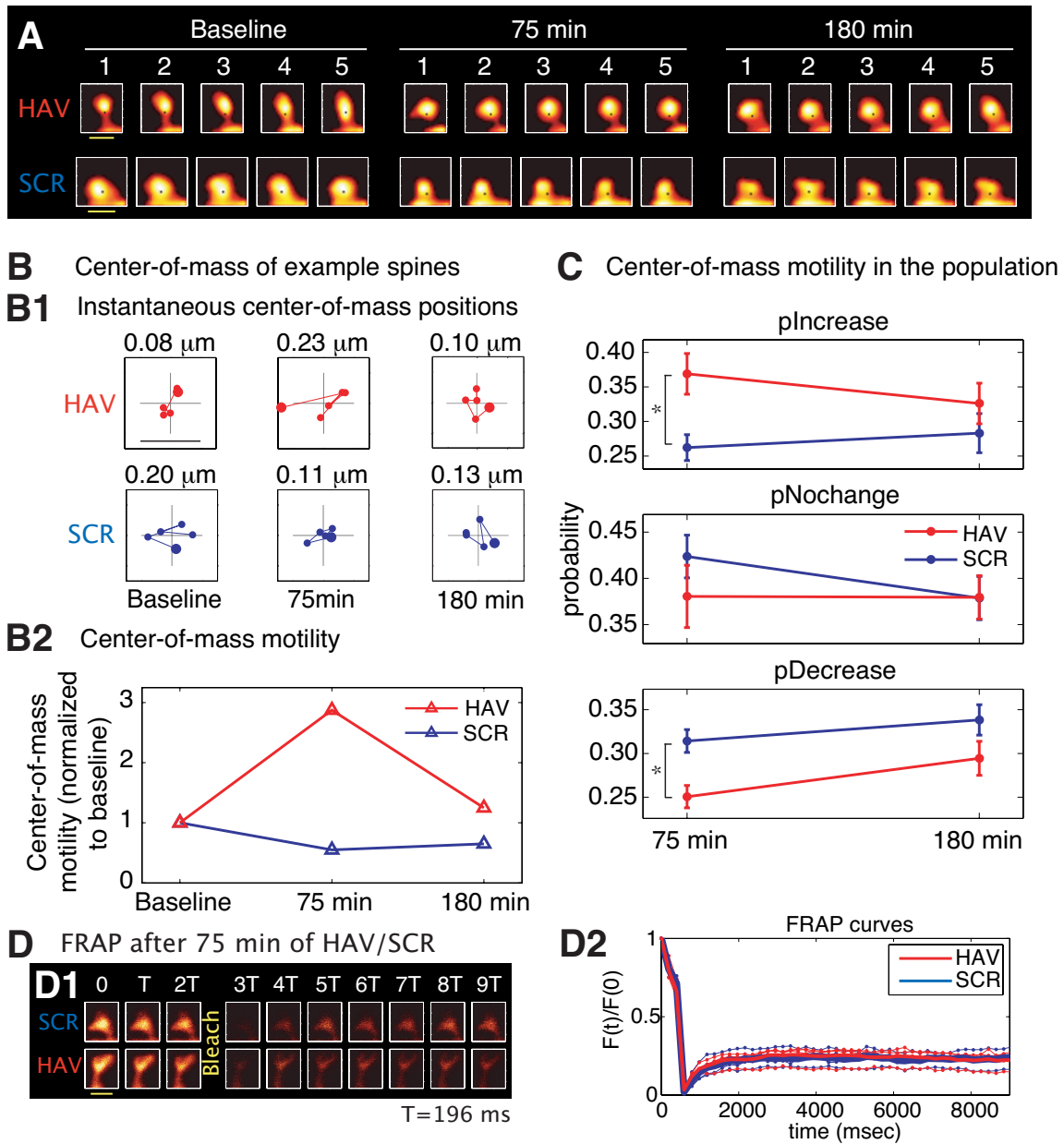


Figure 3-1. More spines show an increase in center-of-mass motility after surface N-cadherin disruption.

(A) Time-lapse images of representative persistent spines from neurons treated with AHAVD (HAV) and AADHV (SCR) acquired at baseline, 75 min after treatment, and 180 min after treatment. The black dot superposed on each image represents the center-of-mass of the spine at that instant as computed from the thresholded image (see Methods). Scalebar = 1 μm . (B) Center-of-mass calculations for the example spines shown in (A). (B1) Each panel shows the locus of successive instantaneous center-of-mass positions over the five minutes within a time-point (after translational normalization

to center the locus at the origin). The large filled circle represents the position of the spine at the first minute within that time-point. The locus in each panel gives a visual indication of the extent to which the spine is motile. The center-of-mass motility value (net movement) of the spine within a time-point is indicated above the panel. The scalebar = 0.1 μm and applies to all panels. **(B2)** Center-of-mass motility of the example spines is plotted normalized to baseline. There was no significant difference at the baseline time-point in the center-of-mass motility values between the HAV- and SCR-treated spine populations. **(C)** Summary data showing the probabilities of increase (pIncrease), no change (pNochange), and decrease (pDecrease) in the center-of-mass motility of all persistent spines. The motility value of a spine at each time-point was compared to that at baseline to determine the nature of change. Probabilities of change were estimated from groups of 50 spines (see Methods). Data in this and subsequent figures are based on approximately 1500 spines from HAV- and SCR-treated cells. **(D)** Fluorescence recovery after photobleaching (FRAP) at 75 min after either HAV or SCR treatment. **(D1)** Time-lapse images of representative spines from HAV- and SCR- treated cells showing FRAP. **(D2)** Individual FRAP curves from four spines for each of the two treatments (red dots – HAV, blue dots – SCR), along with the average FRAP curves for each treatment (thick solid lines). The average curves for HAV and SCR spines were nearly identical. Scalebar = 1 μm .

B. More spines shrink in length after N-cadherin disruption

We next examined if N-cadherin disruption had an effect on slow spine dynamics (Fig. 3-2). We found that more spines showed a reduction in slow length dynamics (*average length*) 75 min after N-cadherin disruption (Fig. 3-2C). Again, as with center-of-mass motility, this effect was not observed 180 min post-treatment (Fig. 3-2C), and there was no difference between the average length distributions of HAV- and SCR-treated spines (data not shown). These data show that N-cadherin disruption preferentially produces a decrease in average length (slow timescale) and an increase in center-of-mass motility (fast timescale). Together with the absence of an effect on other

spine quantifiers at the fast and slow timescales, these data establish that (1) different aspects of spine structural plasticity can be separately regulated, and that (2) this regulation can be exerted independently at two different timescales.

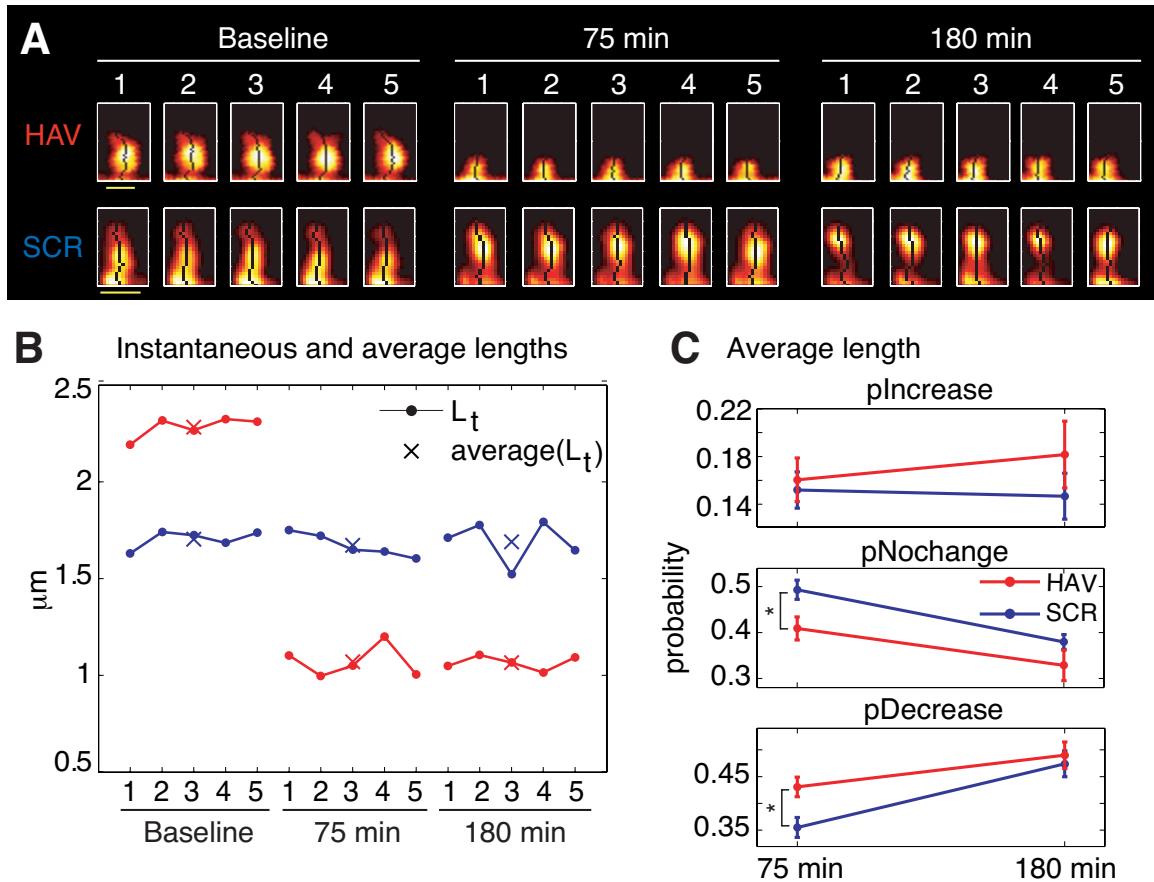


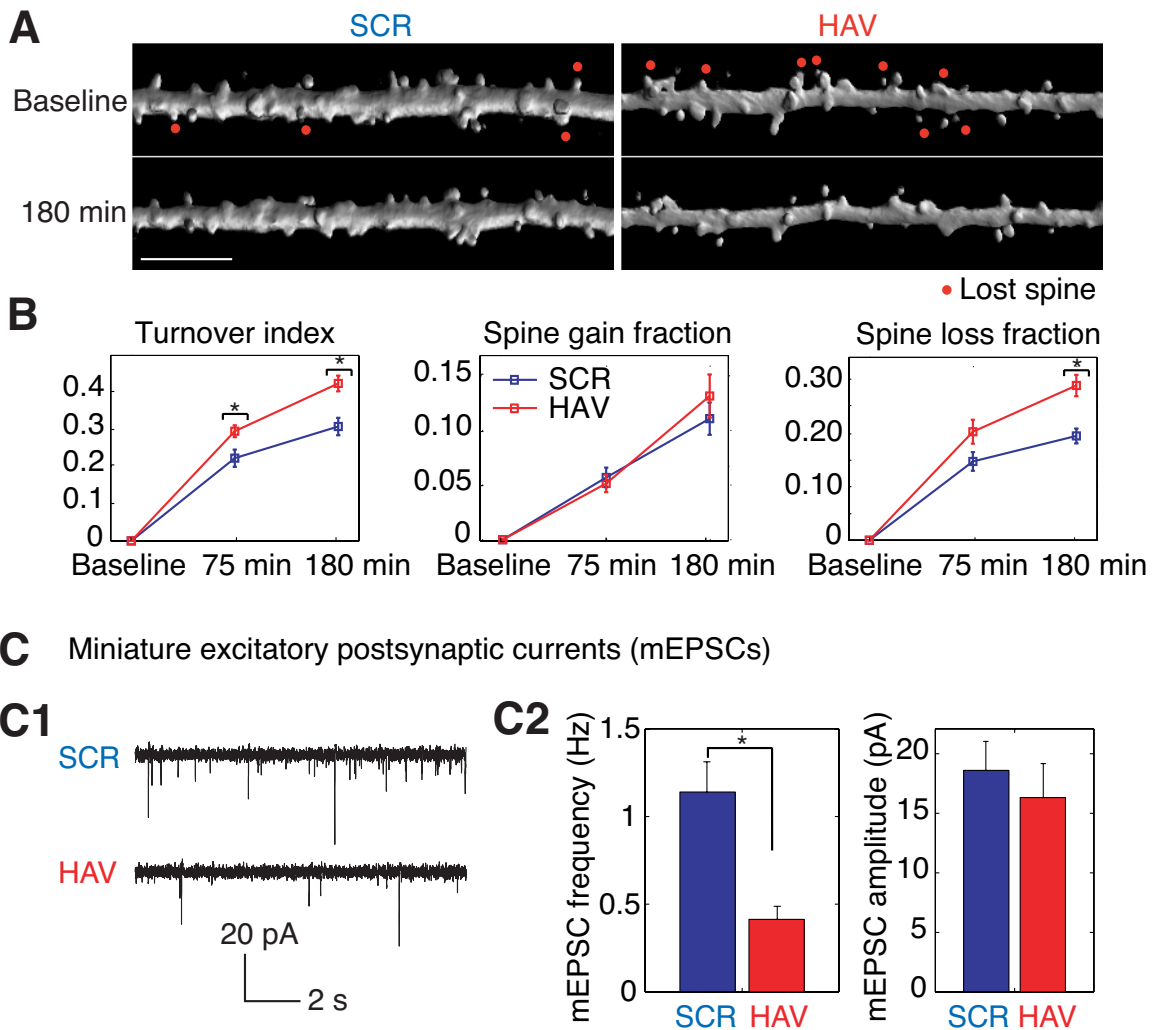
Figure 3-2. More spines shrink in length after surface N-cadherin disruption.

(A) Time-lapse images of representative persistent spines from HAV- and SCR-treated neurons. The single-pixel curve superposed on each image represents the instantaneous centerline of the spine generated using a thresholded version of the raw image (see Methods). Scalebar = 1 μm . (B) Instantaneous and average lengths of example spines shown in (A). (B1) Instantaneous lengths are denoted by filled circles, and average lengths at the three time-points by "X". (C) Summary data from all the spines showing the probabilities of increase (pIncrease), no change (pNochange), and decrease (pDecrease) in the average length. These are calculated by comparing the average length of a spine at each time point to that at baseline (see chapter 2, section 2E for details).

C. N-cadherin disruption induces spine loss and synapse elimination

In addition to changes in spine motility, it is possible to observe the growth of new spines or the complete retraction of preexisting ones. N-cadherin disruption

produced drastic effects on spines (Fig. 3-3). Spine turnover (spine turnover fraction = (spines lost + spines gained)/number of initial spines) was significantly greater than in control beginning at 75 min (Fig. 3-3B, left panel). When spine turnover was split up into its component loss and gain fractions, there was no significant change in the gain fraction (Fig. 3-3B, middle panel); however the spine loss fraction was significantly greater at 180 min post-treatment (Fig. 3-3B, right panel). These data show that acute N-cadherin disruption at mature hippocampal synapses induces spine loss and suggest a commensurate elimination of existing functional synapses. To examine whether functional connectivity between neurons is altered by N-cadherin disruption, we measured the frequency and amplitude of miniature excitatory post-synaptic currents (mEPSCs) recorded under whole-cell voltage clamp conditions. We found that HAV treatment significantly reduced mEPSC frequency without altering mean mEPSC amplitude (Fig. 3-3C). The above results indicate that spine loss induced by N-cadherin disruption is associated with the elimination of functional synaptic contacts.

Fig. 4.**Figure 3-3. Acute disruption of surface N-cadherin induces spine loss.**

(A) Time-lapse images of representative, 3D reconstructed dendrites from neurons expressing soluble EGFP, obtained before (baseline) and 180 minutes after treatment. Left and right panels show SCR- and HAV-treated dendrites, respectively. Scalebar = 5 μ m. (B) Summary data showing, from left to right, spine turnover index ((loss+gain)/total), spine loss fraction, and spine gain fraction. (C) Examining miniature synaptic events (mEPSCs) with voltage-clamp recordings to determine functional effects. (C1) Sample mEPSCs from HAV- and SCR-treated cells recorded at 30 min after treatment. (C2) mEPSC frequency and amplitude plots.

D. Increased spine motility and shorter spine length after N-cadherin disruption predict later spine loss

Functional disruption of N-cadherin leads to changes in the average length and center-of-mass motility behavior of spines at 75 min and increased spine loss at 180 min. To examine whether early changes in spine behavior are linked to later loss, we compared the joint probability distributions governing center-of-mass motility behavior of spines at 75 min and spine fate at 180 min, between treatment (HAV) and scrambled control (SCR) groups. We found that the relationships between early spine behavior and later spine fate were significantly altered by treatment (Fig. 3-4). Interestingly, after HAV treatment, spines with increased center-of-mass motility were preferentially lost when compared to spines with other center-of-mass motility behavior (Fig. 3-4, A1 to A2, and C). Similarly, when we examined the joint probability distributions of average length at 75 min and spine fate at 180 min, we found that spines that first decreased in length were preferentially lost at the later time-point (Fig. 3-4B1 to B2, and C). Together, these data show an increased correlation between early and late spine changes when compared to control and suggest directed structural effects of surface N-cadherin disruption: An early increase in motility and a decrease in length are structural precursors of later spine loss.

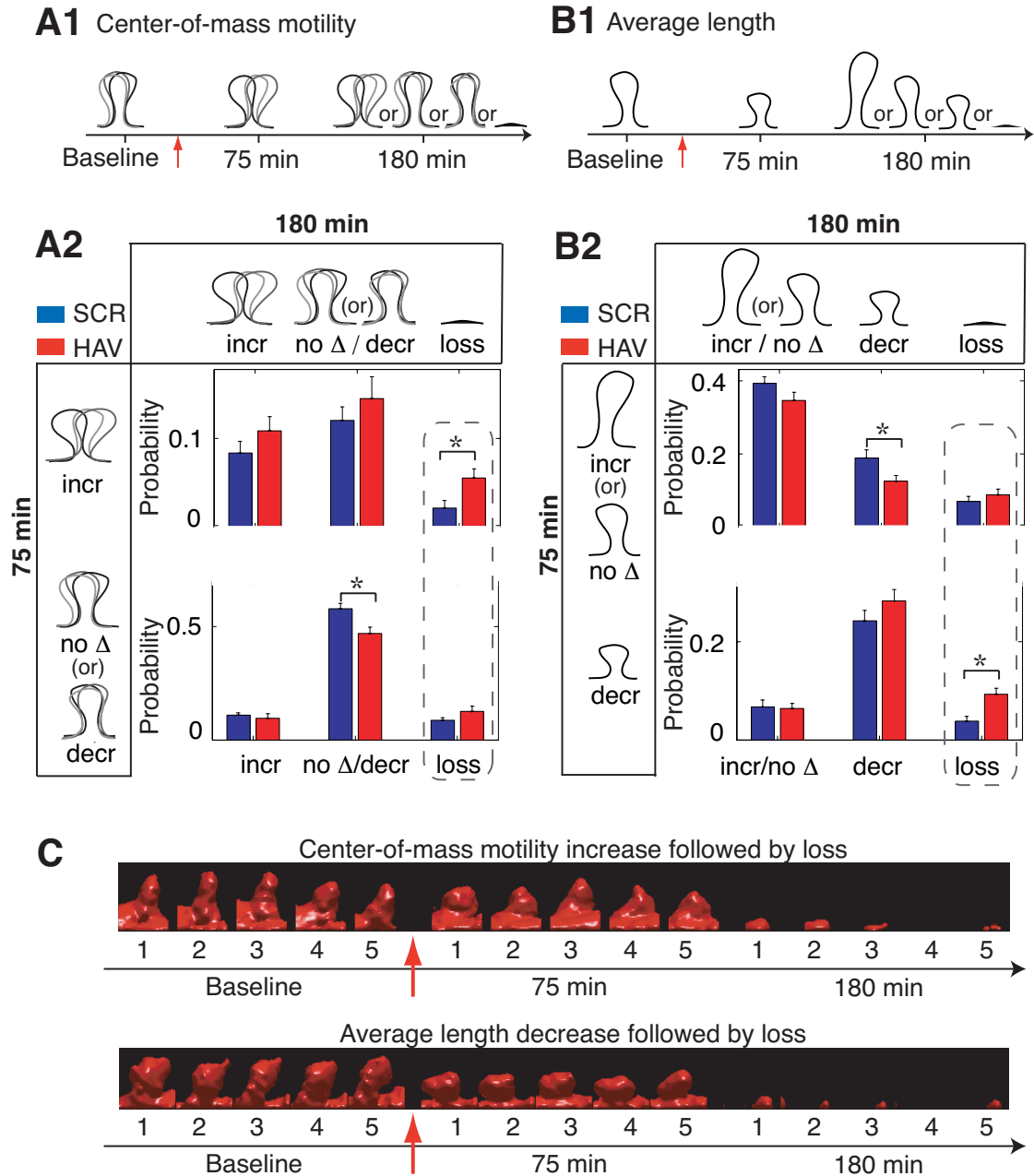
Fig. 5.

Figure 3-4. Increased spine motility and shorter spine length at early time-point after N-cadherin disruption predict later spine loss.

(A1) Schematic showing a spine with an increase in center-of-mass motility at 75 min and its possible states (with respect to center-of-mass motility) at 180 min. (A2) Joint probability distribution between center-of-mass motility at 75 min and spine fate (with respect to center-of-mass motility) at 180 min. The possible states of a spine at 75 and 180 min yield a joint distribution with 2x3 states in total. This distribution for HAV-

treated spines is significantly different from that of SCR-treated spines (control) as indicated by “*” (see Methods). The dashed box highlights the comparisons of interest and points to the increase with respect to control in the fraction of spines that first show an increase in center-of-mass motility and are then lost. Note that the fraction of spines that show other center-of-mass motility (no change or decrease) at 75 min and are then lost is not different between treatment and control. **(B1)** Schematic showing a spine with decrease in average length at 75 min and its possible states (with respect to average length) at 180 min. **(B2)** Joint probability distribution between average spine length behavior at 75 min and spine fate 180 min; 2x3 states in total. The joint distributions of HAV- and SCR-treated spines are significantly different. Further, spines that show a decrease in length at 75 min are preferentially lost at 180 min after HAV treatment – dashed box. We tested for correlations between average length and center-of-mass motility at 75 min and found no significant difference between HAV and control spines (data not shown). **(C)** (Top panel) Time-lapse, volume-rendered images of an HAV-treated spine that showed an increase in motility at 75 min and was subsequently lost at 180 min. (Bottom panel) Volume-rendered images of an HAV treated spine that first decreased in length and was then lost. Red arrows indicate the 10 min application of treatment at time $t=0$ min.

3.4 Results: Subcellular effects of acute N-cadherin disruption

In the above experiments we observed significant structural and functional changes in spines as a result of surface N-cadherin disruption. We next investigated the signaling consequences of this disruption downstream of N-cadherin. β -catenin is an important intracellular binding partner of N-cadherin (Ozawa, 1990a) and it mediates the association of N-cadherin to the actin cytoskeleton via α -catenin (Hirano, 1992; Nagafuchi, 1994). The binding of β -catenin to N-cadherin is known to be regulated by changes in the phosphorylation of its tyrosine residues (particularly, Tyr-654 (Roura, 1999)), and this, in turn, modulates cadherin-mediated surface adhesion (Müller, 1999;

Ozawa, 1998). It has been shown that synaptic activity can regulate the distribution of β -catenin at synapses, most likely by affecting the phosphorylation of Tyr-654 (Murase et al., 2002), with consequences to synaptic function and structure. β -catenin is also known to regulate the assembly of synaptic vesicles via the recruitment of PDZ proteins (Bamji et al., 2003). Finally, β -catenin is involved in the regulation of dendritic structure (Yu and Malenka, 2003). For these reasons, β -catenin is a prime candidate in any investigation of signaling mechanisms downstream of N-cadherin.

A. N-cadherin disruption produces a biphasic response in spine β -catenin

To uncover the effects of surface N-cadherin disruption on β -catenin inside the cell, we performed time-lapse imaging on cells expressing a β -catenin-GFP construct (Fig. 3-5). We examined β -catenin's distribution before and after the application of HAV or the SCR peptide. Interestingly, there was a biphasic response in the distribution of β -catenin (Fig. 3-5A and B). We found that after HAV treatment, more spines than in control showed an initial increase (~ 30 min) in β -catenin levels. Fig. 3-5A and B show representative spines from HAV- and SCR-treated cells, and Fig. 3-5C shows the population response in terms of probabilities of change, as a function of time. Subsequently, this difference between treatment and control was abolished suggesting that the initial increase in the probability of β -catenin accumulation in spines was followed by an increase in the probability of exit from spines.

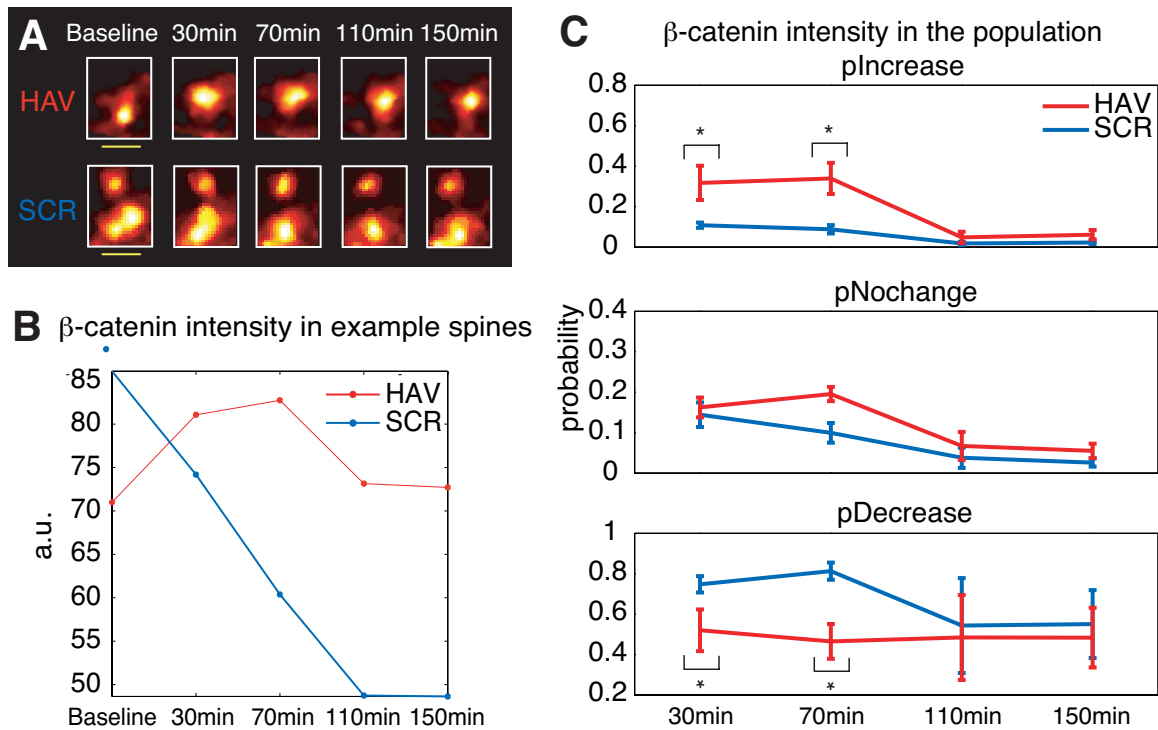


Figure 3-5. β -catenin-GFP shows a biphasic response in spines after surface N-cadherin disruption.

(A) Time-lapse images of β -catenin-GFP signal in examples spines from HAV- and SCR-treated neurons. Scalebar = $1\mu\text{m}$. (B) Total intensity of β -catenin-GFP in example spines. Comparison between the baseline intensity distributions of all HAV- and SCR-treated spines yielded no difference (data not shown). (C) Summary data showing the probabilities of increase, no change, and decrease in β -catenin-GFP signal in spines. These are calculated by comparing the β -catenin-GFP signal at each time-group to that at baseline.

B. N-cadherin disruption reduces binding of β -catenin to N-cadherin, but not to other binding partners

β -catenin is known to have an overall stabilizing effect on spines. For instance, Murase et al. (2002) show that when the phosphorylation of β -catenin's tyrosine 654 is prevented (Y654F mutant), β -catenin accumulates in spines and increases its association with N-cadherin. In addition, there is an increase in mEPSC frequency. Here, in spite of the initial increase in β -catenin in spines, we see a shortening of spines and a reduction in

mEPSC frequency. How can we reconcile these apparently contradictory findings? We hypothesized that surface cadherin disruption may lead to a reduction in the ability of β -catenin to bind to N-cadherin. If true, this can explain the observed instability despite the increase in spine β -catenin (recall that Murase et al. show an increased N-cadherin- β -catenin association in the Y654F mutant). To test whether the binding N-cadherin and β -catenin is affected, we immunoprecipitated β -catenin from neuronal cell lysates after either HAV or SCR treatment. We then probed for N-cadherin and also for other binding partners of β -catenin (Fig. 3-6). Additionally, we probed for tyrosine-phosphorylated β -catenin. We found that N-cadherin disruption caused a reduction in the binding of N-cadherin to β -catenin (Fig. 3-6). However, the binding of β -catenin to its other intracellular partners was increased and there was also an increase in the tyrosine phosphorylation of β -catenin (Fig. 3-6). Thus the HAV-induced disruption of surface N-cadherin interferes specifically with the binding of β -catenin to N-cadherin. In view of this, the increase in tyrosine phosphorylation of β -catenin (Fig. 3-6), the reduced mEPSC frequency (Fig. 3-3C), and the spine shortening that we observe here do not contradict the prior observations of Murase et al. (2002) if indeed β -catenin binding to N-cadherin is necessary for the functional and structural stabilization reported. Interestingly, these data suggest that β -catenin movement in and out of spines is perhaps independent of tyrosine phosphorylation, while its binding to N-cadherin and its longer-term accumulation in spines is not.¹⁴

¹⁴ This suggests a “capture model” over a “directed movement” model to explain the data reported in Murase et al., 2002.

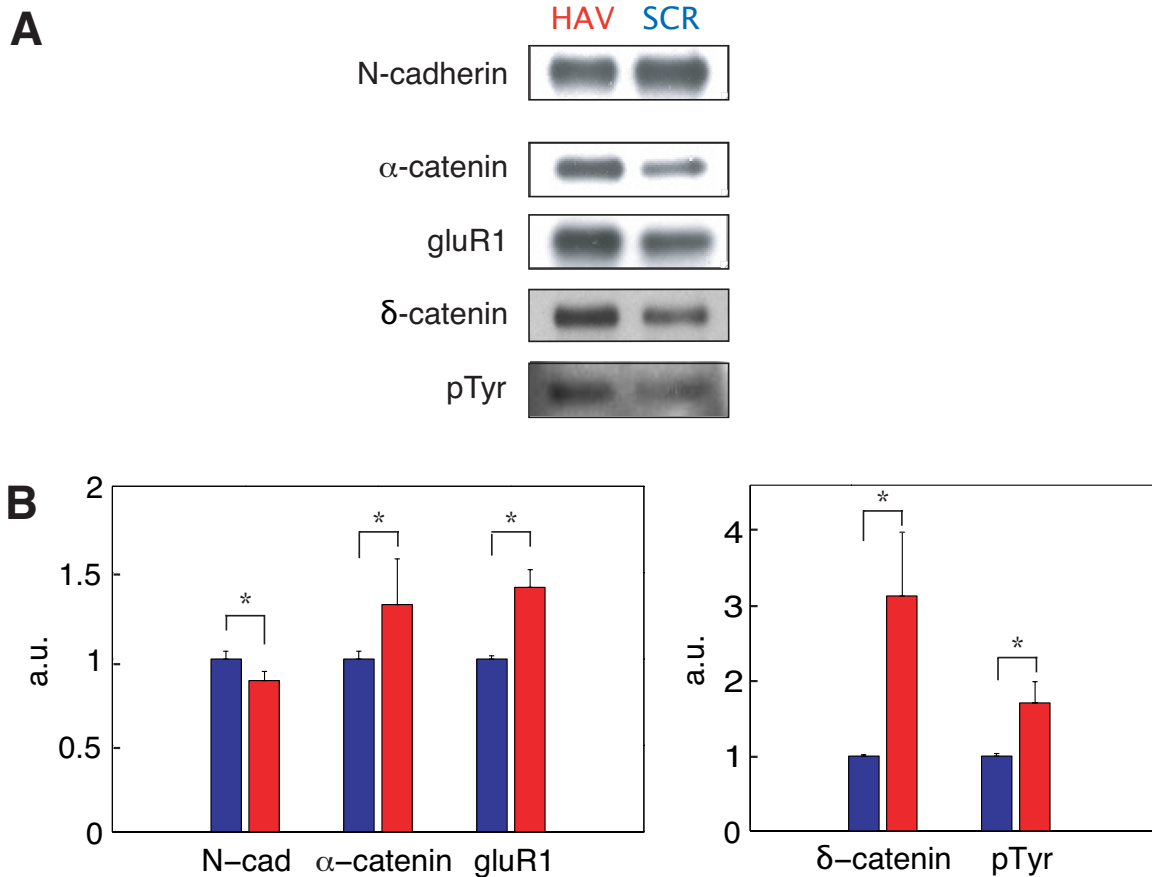


Figure 3-6. β -catenin binding to N-cadherin is preferentially reduced 30 minutes after surface N-cadherin disruption.

(A) Representative blot of β -catenin immunoprecipitation followed by probing with antibodies against α -catenin, gluR1, N-cadherin, δ -catenin, tyrosine-phosphorylated β -catenin, and β -catenin. (B) Summary data of protein amounts normalized to immunoprecipitated β -catenin.

C. N-cadherin disruption produces biphasic responses in endogenous β -catenin and surface N-cadherin

We have established that there is a biphasic response of overexpressed β -catenin following N-cadherin disruption. Could this be simply an overexpression artifact or can we see the same effect on endogenous β -catenin as well? Also, what is the effect of N-cadherin disruption on surface N-cadherin distribution? To address these questions, we performed immunofluorescence experiments on HAV- and SCR-treated neurons at

different time-points (30, 75, and 150 min) using antibodies against (surface) N-cadherin, β -catenin, and bassoon, a pre-synaptic marker (Fig. 3-7). We calculated the number of puncta per μm , mean puncta volume, and mean puncta intensity for each of the proteins (Fig. 3-7B1 to 3). Consistent with the data from the overexpression experiment (Fig. 3-5), we found a biphasic response in endogenous β -catenin puncta number as a result of HAV treatment – with respect to control, there was an initial increase in the number of puncta per μm at 30 min followed by a subsequent decrease at 150 min (Fig. 3-7B2, top panel). The volume and intensity of β -catenin puncta were lower than in control at 150 min after HAV treatment (Fig. 3-7B2, middle and bottom panels). Further, we found that surface N-cadherin puncta were smaller and less intense at 30 min following treatment, but larger and more intense at 150 min (Fig. 3-7B1, middle and bottom panels). These data suggest an initial reduction in the disrupted (non-functional) surface N-cadherin, followed by a replacement of cadherin (presumably functional) to previously existing surface sites, but not to new sites (Fig. 3-7B1, top panel).

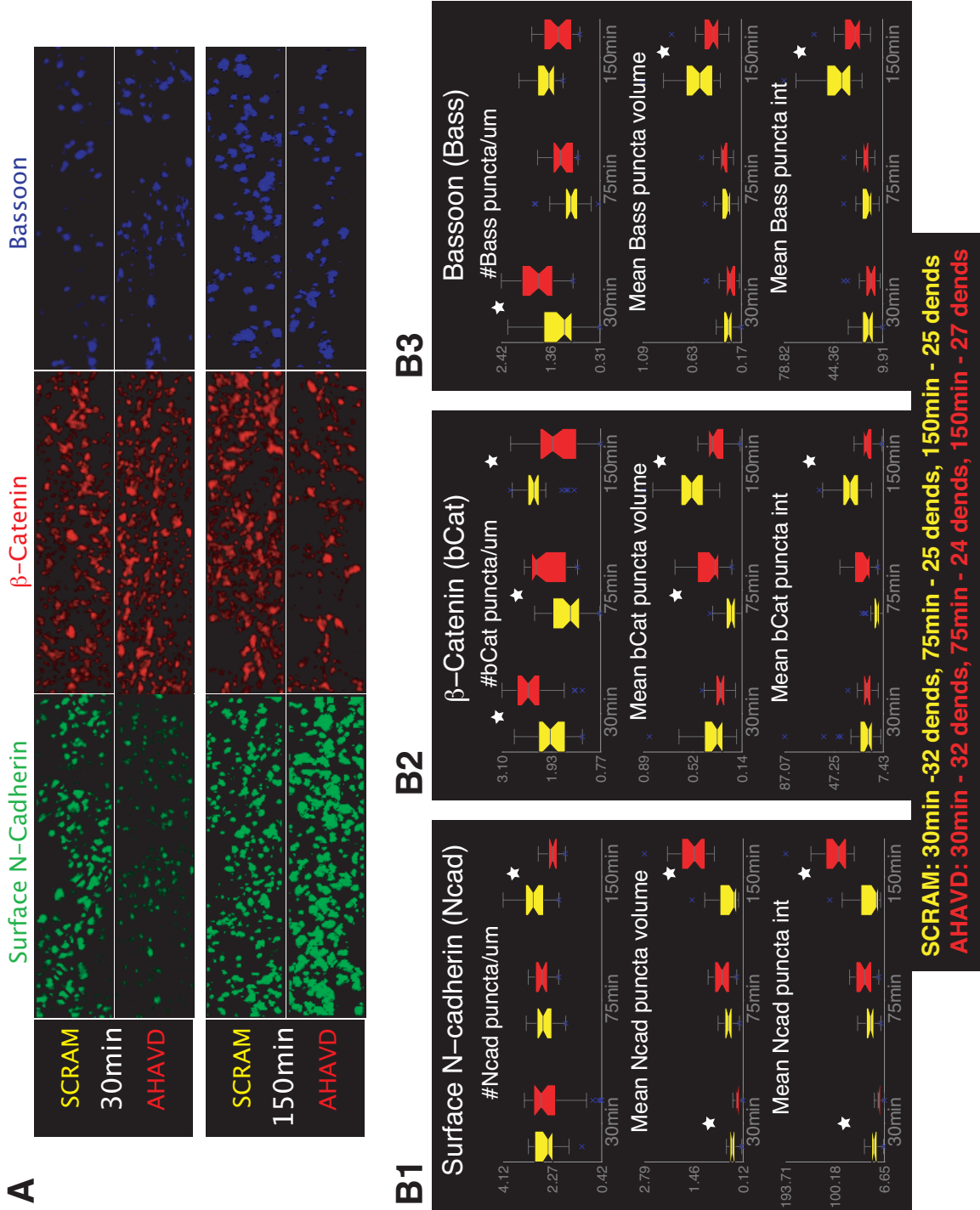


Figure 3-7. N-cadherin disruption produces a biphasic response in endogenous β -catenin and N-cadherin.

(A) Representative dendrites showing protein distributions at 30 and 150 min after either HAV or SCR treatments. N-cadherin, β -catenin, and bassoon puncta are shown in green,

red, and blue, respectively. **(B)** Summary data of puncta number, volume, and intensity of N-cadherin, β -catenin, and bassoon over time, shown with box-plots.

D. N-cadherin disruption produces long-lasting effects on N-cadherin-mediated adhesion in L-cells

It is clear that intracellular signaling mechanisms are activated as a result of N-cadherin disruption by HAV treatment. However, do the observed long-term structural effects on spine dynamics represent a persistent HAV-initiated effect on adhesion or just an effect of intracellular signaling downstream of adhesion? To address this question, we performed aggregation assays on L-cells that stably expressed N-cadherin (Fig. 3-5) and monitored the effect of HAV on N-cadherin-mediated adhesion. When previously plated L-cells were released, dissociated and then allowed to re-aggregate following either HAV, SCR, or vehicle (HBS) treatment for 10 min, we found that HAV-treated cells exhibit dramatically impaired re-aggregation at 180 min (Supp Fig. 2A and B). This suggests that a brief disruption of cadherin function can have long-lasting, destabilizing effects on N-cadherin-mediated adhesion, contributing, at least in part, to prolonged structural effects on neuronal spines.

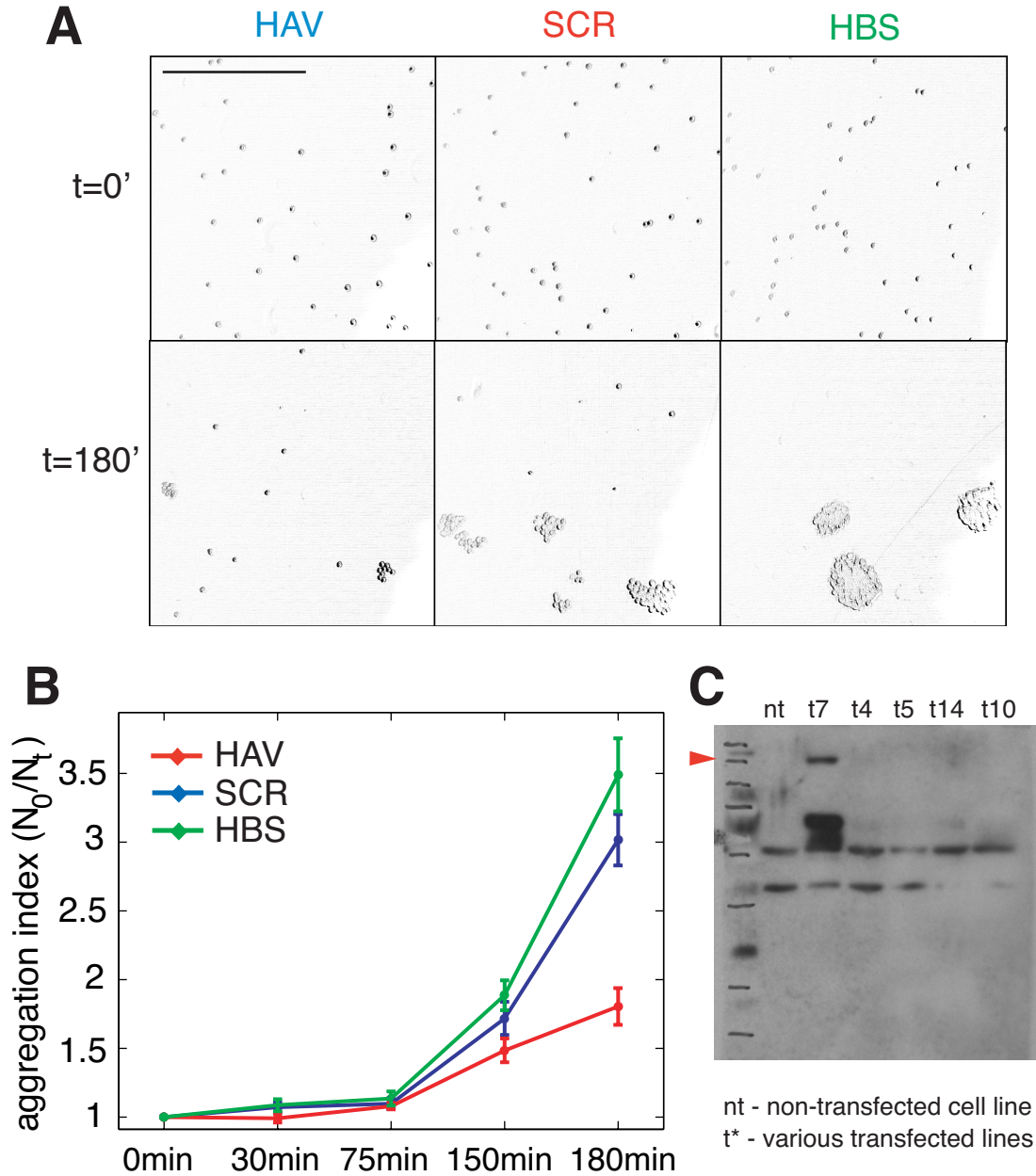


Figure 3-8. N-cadherin disruption by 10 min HAV treatment causes long-lasting effects on cadherin-mediated adhesion.

(A) DIC images of L-cells plated onto slides at different time-points, after being treated with HAV, SCR, or HBS for 10 minutes (see methods). Scalebar = 650 μ m. (B) Plot of the aggregation efficiency of L-cells as a function of time, measured as N_0/N_t (see methods). A higher N_0/N_t value indicates greater adhesion. HAV – red, SCR – blue, HBS – green. (C) Western blot showing cell lysates from various stable lines probed for N-cadherin. Only one transfected line (t7) shows successful incorporation of N-cadherin as

indicated by the red arrowhead corresponding to the size of N-cadherin. Cells from line t7 were used for all L-cell experiments.

3.6 Conclusions

Thus, we observe significant structural and functional changes in synapses after an acute disruption of N-cadherin using the HAV peptide. Spines first shrink in length, exhibit greater motility, and are subsequently lost. This is accompanied by synapse elimination, as indicated by the drop in mEPSC frequency. Intracellularly, the distribution of β -catenin is altered in a biphasic manner. This suggests a role for β -catenin as a post-synaptic stabilization factor. In the experiments described here, β -catenin is unable to effect this stabilization, perhaps because of the reduced availability of N-cadherin for association. Experiments in heterologous cells suggest that the significant structural effects we see are the result, at least in part, of the direct effects of loss of N-cadherin-mediated adhesion.

On the one hand, these results show, for the first time, that structural plasticity in the form of synapse elimination induced by N-cadherin can be predicted by earlier changes in fast and slow spine dynamics. Such a relationship between timescales, and between forms of structural plasticity, is novel and suggests a concerted regulation of structural dynamics. Additionally, these data begin to shed light on the signaling mechanisms that are triggered as a result of acute disruption of functional N-cadherin. Taken as a whole, our work strongly suggests that N-cadherin is a key cell-adhesion molecule responsible for the structural and functional integrity of mature hippocampal synapses.

3.7 Future directions

A. Structural compensation in response to N-cadherin disruption

We have shown that at 180 min after HAV treatment, spine loss is still greater than control. It has been shown in the literature (Togashi et al., 2002) that after chronic (3Day) N-cadherin disruption via the overexpression of the dominant-negative form, spines are elongated (they resemble filopodia) though there is no change in their density. Given these data, it is plausible that at some point between 3 hours and 3 days after N-cadherin disruption there is a recovery in spine number via new spine addition. The increase in the incidence of filopodia-like protrusions (Togashi et al., 2002) is consistent with this hypothesis since filopodia are thought to be precursors of spines (Dailey and Smith, 1996). This idea of spine-density recovery can be tested by performing longer time-lapse experiments after acute N-cadherin disruption in neurons infected with a lentiviral GFP construct, as opposed to a Sindbis GFP construct.

B. Functional recovery after N-cadherin disruption

Our electrophysiology data show a reduction in mEPSC frequency 30 min after HAV treatment. What are the longer-term functional effects of N-cadherin disruption? Can one see a recovery of synaptic function as well, and if so, how long does it take? In general, it will be interesting to understand what long-term compensatory mechanisms are employed by the cell in order to recover from surface N-cadherin disruption.

C. Correlating structure-function changes at synapses after N-cadherin disruption

While we have investigated structural and functional effects separately, it will be very informative to perform experiments where these aspects can be studied in parallel. One approach is to infect cells with EGFP (to monitor spine dynamics) and, in addition,

to load them with FM 4-64 (a fluorescent indicator of pre-synaptic activity, see Sara et al., 2005). Two-color, time-lapse imaging in this scenario will allow us to correlate pre-synaptic activity at individual synapses, with instantaneous changes in morphology (see Colicos et al., 2001). A key insight that these experiments will yield is whether the observed mEPSC reduction is due largely to pre-synaptic causes (for instance, due to reduction in release probability), or whether there is a post-synaptic component as well (spines that have shortened and shrunk away from the pre-synaptic terminal are unable to detect release events as well as before). Loading can also be performed at different time-points (across cells) to see if new, active pre-synaptic terminals are formed over longer periods. Additionally, loading-destaining experiments can reveal changes in kinetics of release at pre-synaptic sites (Sara et al., 2005).

D. Changes to synaptic protein distributions after N-cadherin disruption: detailed investigation

What other changes occur in synaptic protein distributions? We have uncovered the regulation of surface N-cadherin, β -catenin, and bassoon through immunofluorescence experiments at several time-points. It will be of great interest to study changes in the distributions of proteins like gluR1, gluR2, and NR1 that critically influence synaptic function.

E. Uncovering the signaling mechanisms in detail

What is the mechanism that produces all the observed changes? We have shown that β -catenin is involved in intracellular signaling, and that there is a direct lack of adhesion as well. However, how do these signals ultimately produce the observed changes in spine structure, number, synaptic protein distributions, and synaptic function? What is the meaning of the biphasic spine response observed in β -catenin? One approach

to answer this question is to perform two-color, time-lapse imaging experiments in neurons expressing a bicistronic viral vector with β -catenin-GFP and EGFP. This will allow us to monitor the relationship between β -catenin dynamics and spine dynamics.

Additionally, given the role of the Rho family of small GTPases in regulating spine dynamics (Bonhoeffer and Yuste, 2002; Lamprecht and LeDoux, 2004; Tashiro and Yuste, 2004), and their links to the N-cadherin adhesion complex (Anastasiadis and Reynolds, 2001; Fukata and Kaibuchi, 2001; Magie et al., 2002; Okabe et al., 2003), investigating their recruitment will be a step in the right direction. Uncovering the signaling mechanisms involved will be critical to a fuller understanding of the regulation by N-cadherin of synapse structure and function.

F. What is unique about the spines that are lost?

Here, we have shown a 30% loss of spines in response to cell-wide N-cadherin disruption. What makes these spines more susceptible to loss, and how/why are the others protected? Unpublished data in the lab indicate that more than 90% of spines have functional synapses in the mature hippocampal neurons in our cell-culture system; thus, an absence of pre-synaptic terminals does not explain the spine loss. We examined spine type at the baseline time-group and found no relationship with subsequent loss, ruling it out as a determining factor. Therefore, differences either in the distribution of other cell-adhesion molecules at synapses (see Yamagata et al., 2003), or in the biochemical signaling (as discussed in E above) are likely factors that determine differences in response to N-cadherin disruption, and these possibilities can be explored.

G. Predicting structural dynamics

We have shown here, for the first time, that there is a progression of structural events in response to N-cadherin disruption, and that early structural events can predict later ones. If such analysis is systematically extended to several other treatments that produce structural effects, it may be possible to extract general rules linking earlier spine dynamics to, for instance, later synapse elimination. Information of this kind (for instance, see Knott et al., 2006) will greatly enhance our understanding of the role of spine dynamics in neuronal function.

H. Why do neighboring spines display widely different dynamics?

We have discussed in this chapter and in chapter 2 that spines display morphological dynamics across a wide spectrum, and that neighboring spines can behave very differently. What, intrinsically, is the reason for this difference? One approach to get at the answer is to systematically correlate the composition of every spine with its motility. Correlative light and electron microscopy¹⁵ (Cabirol-Pol et al., 2000; Dunaevsky et al., 2001) with immunogold labeling (Phend et al., 1995; Phend et al., 1992), though a difficult technique, can successfully address this question – a central one in the field of spine motility.

I. Spine twitching: moment-to-moment regulation of synaptic efficacy?

The idea that spines may twitch and that this may happen via actin cytoskeletal dynamics was suggested prominently by Crick about two decades ago (Crick, 1982). The author proposed that this fast-timescale movement may underlie fast, but transient, changes in synaptic efficacy. Thus far, this idea has remained untested. Appropriate technology to perform correlative structure-function experiments at a timescale of tens of

¹⁵ See Neuhoff et al., 1999 for EM protocol in cultured neurons.

milliseconds may now be available to test this hypothesis explicitly in an attempt to further our understanding of the function of spine motility. Structural imaging of a GFP- or GFP-actin-filled spine can be combined with either perforated-patch electrophysiological recordings (for instance, Matsuzaki et al., 2004) or calcium imaging (for instance, Majewska et al., 2000) in response to two-photon uncaging of MNI-glutamate (Matsuzaki et al., 2004). This will allow a correlation of the moment-to-moment spine morphology with its functional efficacy. Though not an easy experiment, it has the potential of yielding insight into another central question in the spine motility field; namely, the function of spine motility.

Chapter 4. Modeling architectural plasticity in the auditory localization system of barn owls

4.1 Introduction

Whereas most neurobiological and neural computational studies of plasticity focus on changes in the efficacy of existing synapses, structural plasticity is an important but relatively poorly understood capacity of many nervous systems. This relative neglect is due, in part, to the lack of biologically well-characterized model systems of structural plasticity. One model system for which there is a wealth of detailed data is the auditory localization system in barn owls. While the states of the midbrain pathway involved in auditory localization are well characterized before and after the behavioral adaptation induced by prismatic visual experience, and the nature of the error signal driving plasticity is known, it is not clear how the error signal drives the network to the post-adaptation state. In this work, we propose an explanation that is based on known computational principles, that satisfies neurophysiological constraints, and is consistent with observed experimental data. Below, we first present the key experimental data that we wish the model to capture, briefly discuss other modeling efforts in the literature and their shortcomings, present the details of our model, show results, make specific predictions, and end with directions for future work.

4.2 Key experimental observations

Spatial localization of auditory information is an essential ability for the survival of barn owls. Whereas many animals can localize sounds soon after birth (Field et al., 1980) indicating the hard-wiring of at least a part of this system (Brainard and Knudsen, 1998; Knudsen et al., 1991), experience, in addition to intrinsic programs, plays an important role in shaping and modifying the auditory localization pathway in barn owls. The interaural time difference (ITD) is a primary auditory cue used by barn owls to localize sound in the horizontal direction, and it is defined as the delay (time difference) between the arrival of sound at the two ears (Knudsen, 2002). Unless the sound source is positioned symmetrically with respect to the two ears, the signal has to travel different distances to reach the near ear versus the far ear, resulting in a non-zero ITD.¹⁶ Both the spatial location of the sound source with respect to the head position and its frequency content affect the value of the ITD.

One of the pathways in the barn owl brain that processes ITD information is the midbrain pathway (Knudsen, 2002) shown in Fig. 4-1, where auditory inputs are colored orange and visual in blue. In this pathway, cue information arrives in a frequency-dependent manner at the central nucleus of the inferior colliculus (ICC) and flows through the external nucleus of the inferior colliculus (ICX) to the optic tectum (OT). The ICC has a tonotopic, or frequency-dependent, organization, and ITD information from various frequency channels of the ICC is combined to form a topographic, map-like representation of auditory space in the ICX. Neurons in the ICX have well-defined auditory receptor fields in the sense that they respond best to sound inputs from well-

¹⁶ A rule of thumb linking the spatial angle to the ITD value: $1^\circ \sim 2.5\mu\text{s}$

defined locations in space. The ICX neurons project to the deep layers of the optic tectum (OTD) topographically, thereby conferring OTD neurons with the same receptor fields and conveying topographic information about auditory space (Knudsen, 2002). Interestingly, the superficial layers of the OT (OTS) encode a similar topographic map of *visual* space mediated by visual input from the retina and forebrain. It has been found that the auditory and visual maps of space are aligned and integrated in medial layers of the optic tectum (OTM), and this is achieved through projections from both the OTD (auditory) and the OTS (visual) into the OTM (Knudsen and Brainard, 1995). Additionally, OTM neurons project back to the ICX, thereby conveying instructive visual information to the auditory maps (Knudsen, 2002).

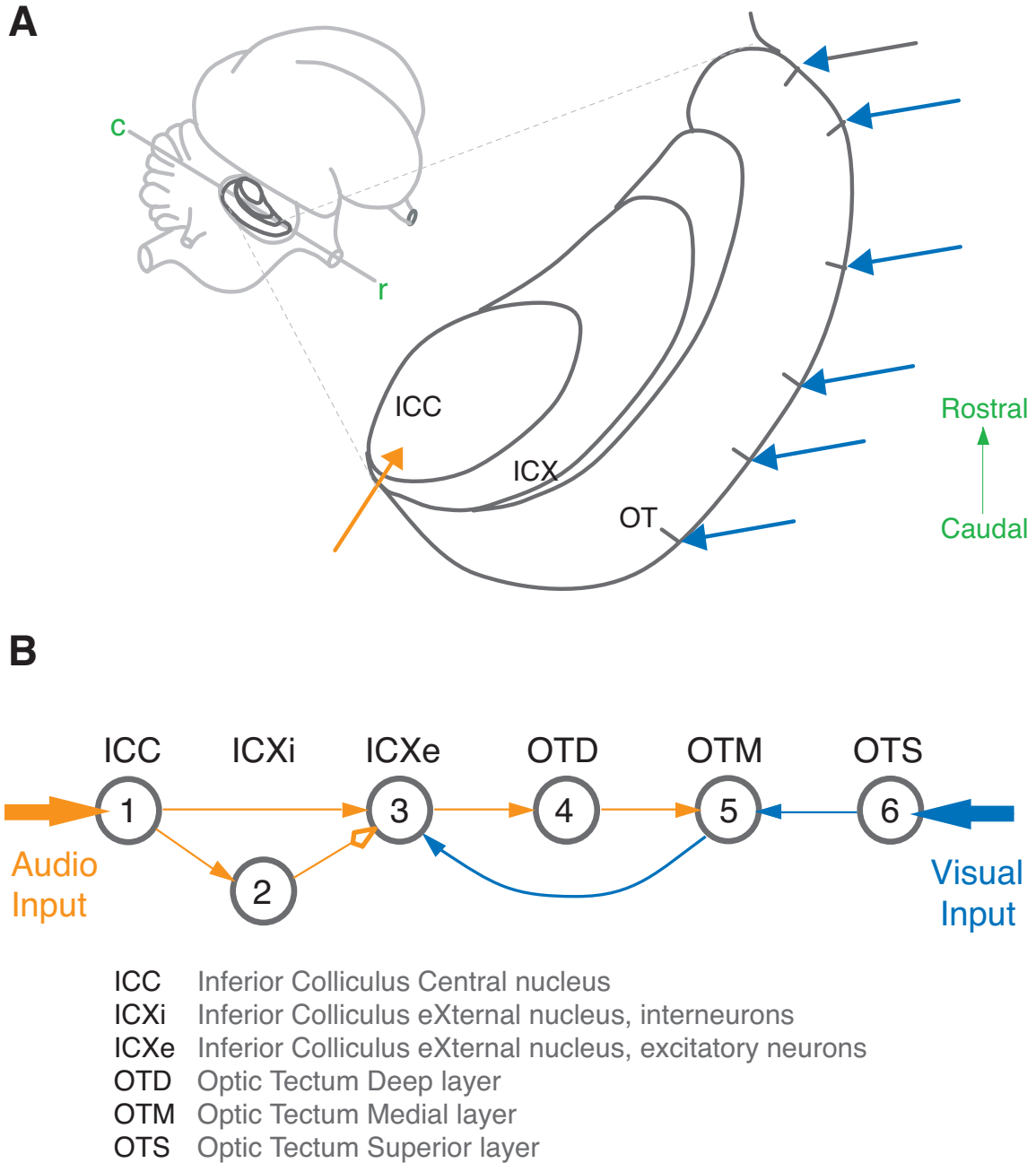


Figure 4-1. Midbrain ITD pathway in barn owls.

(A) Schematic of the midbrain ITD processing pathway in a normal juvenile owl. (B) The functional circuit is represented schematically with neurons as circles, excitatory connections as arrows with filled heads, and inhibitory ones with open heads. ICXi and ICXe refer respectively to inhibitory and excitatory neurons in the ICX layer. Each “row” of neurons is assumed to represent stimuli from one spatial location, and multiple rows encode for the entire space. While topographic projections in the brain are not cleanly

one-to-one as shown here, this assumption simplifies both the understanding and the modeling, while capturing the essence of the network architecture.

Visual displacement experiments have explored the nature of information processing in the midbrain pathway and have shed light on the mechanisms by which plasticity occurs in response to external demands. These experiments involve the use of prismatic spectacles to disrupt auditory-location associations by displacing the visual input along the azimuth by a predetermined amount (Brainard and Knudsen, 1998). For instance, when an owl fitted with glasses that produce a ten-degree rightward shift looks straight ahead, it receives visual information centered at ten degrees to the left, rather than at zero degrees, or straight ahead. As a result, whereas a normal owl can visually localize a sound-source placed at zero degrees by looking straight ahead, one fitted with a right-shifting prism has to learn to rotate its head to the right by the appropriate amount, in order to localize the same source.

It has been found that juvenile owls (< ~180 days of age) display a remarkable ability to behaviorally adapt to (up to a 23° shift) and compensate for prism experience within the course of several weeks (Knudsen, 2002). Removal of prisms after adaptation results in gradual recovery of normal orienting behavior. On the other hand, adult owls adapt poorly to prism experience (Knudsen, 1998). Interestingly, shifted-back juvenile owls that are subsequently fitted with prisms as adults do show adaptability, but only up to the adjustments they had originally displayed (Knudsen, 1998). Recent evidence (Linkenhoker and Knudsen, 2002) also shows that the capacity for behavioral plasticity in adult owls can be increased with incremental training; that is, where the adults experience prismatic shifts in small increments.

Detailed investigations have led to insights about many aspects of the neural implementation of this adaptation. Particularly interesting is the fact that learning in response to chronic prism experience is mediated by structural changes in the neural architecture – new axonal branches grow and synapses are formed between the ICC and the ICX neurons (DeBello et al., 2001) in such a way that the auditory receptor fields of the ICX (and all the downstream neurons) shift, and thereby compensate for the effect of prisms (detailed discussion below, Fig. 4-4). However, the auditory receptor fields of the ICC neurons remain unchanged. This site of plasticity is restricted to the synapses between the ICC and ICX (but see also (DeBello and Knudsen, 2004), where it has been shown that plasticity can occur at the OT as well, at a later stage in development).

What causes this shift in the receptor fields? Visual information has been shown to serve as a topographic instructive signal, or “error” signal, that mediates the changes in the circuit (Hyde and Knudsen, 2001). Interestingly, the “error” is encoded in the firing dynamics of the ICXe neurons (Gutfreund et al., 2002). In normal owls (Fig. 4-2), presentation of a purely auditory stimulus (just the orange, open square in Fig. 4-2A, and just the orange arrows in Fig. 4-2B) resulted in an ICXe burst in the neurons encoding for that special location (in Fig. 4.2B, neuron #9 fires, indicated by its orange shading), and this burst has an onset delay of approximately 15 ms (“auditory response”). However, presentation of a purely visual stimulus¹⁷ (just the blue, filled square in Fig. 4-2A, and just the blue arrow in Fig. 4-2B) from the same location produced a response in the ICXe that has an onset delay of about 90 ms (“visual response”). As the spatial location of this visual stimulus was the same as that of the auditory stimulus earlier, neurons in the same

¹⁷ This is done in the presence of bicuculline in anesthetized owls so as to open the GABA-inhibited gate that, in awake birds, is thought to be opened by attention.

topographic pathway (i.e., same row in the schematic diagram) were involved in the processing, and neuron #9 fired. A visual response in an ICXe neuron will be shown henceforth by blue shading of the corresponding neuron (not shown in Fig. 4-2B, but see Fig. 4-3). Interestingly, when audio and visual stimuli were simultaneously presented (Fig. 4-2A, both the orange, open square and the blue, filled square are present), and the location of the auditory stimulus was continuously varied around the fixed location of the visual stimulus (blue, filled square is kept fixed; orange, open square is moved along the arc representing the frontal auditory hemifield of the owl), the ICXe neurons coding for the spatial location of the visual input produced just the “visual response” when the two inputs were spatially disjoint (not shown), but produced just the “auditory response” (orange shading of neuron #9 in Fig. 4-2B) when the two stimuli were colocalized (both the orange and blue pathways are activated) (Gutfreund et al., 2002). Thus, with spatially coincidental audio-visual input in normal owls, there are hardly any visual responses at all; there are just the auditory responses.

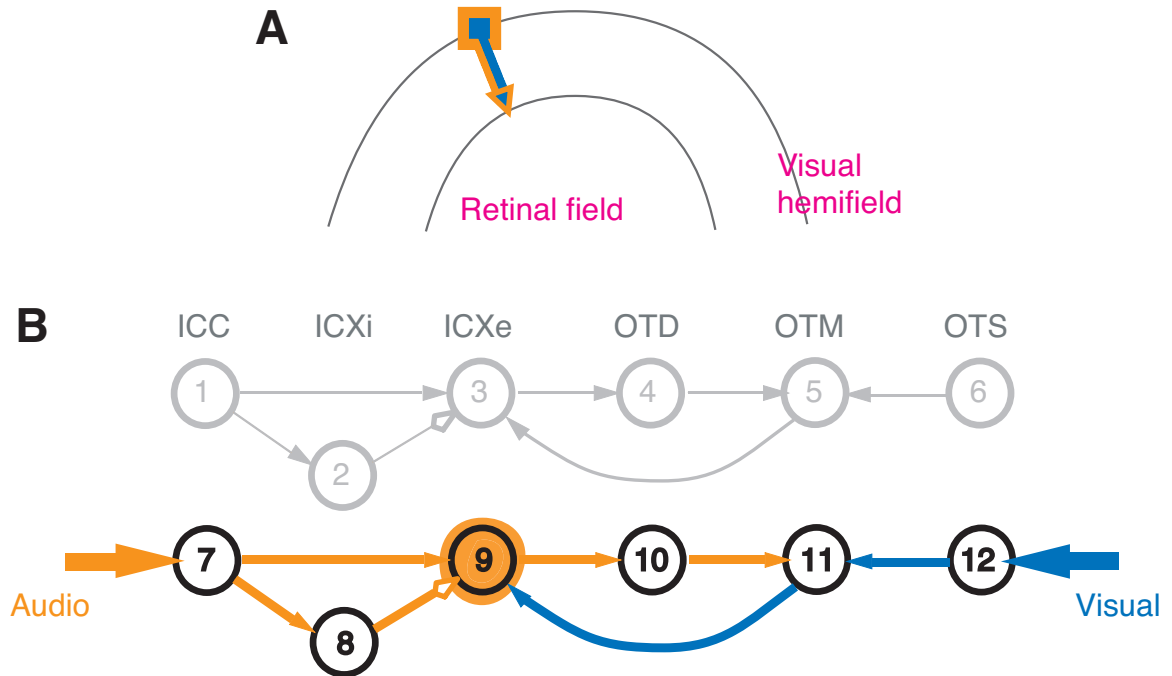


Figure 4-2. Simultaneous presentation of spatially coincidental audio-visual input to normal owl.

(A) Visual and retinal hemifields of a barn owl are schematically shown. The owl's head is at the center of these concentric semi-circles. Audio input represented as the orange, open square, and visual input as the filled, blue square. (B) Schematic showing multiple rows of neurons, each encoding for a different spatial location. When colocalized audio and visual inputs are simultaneously presented, ICXe neuron #9 fires just the auditory response (15 ms delayed bursting response, orange shading), not the visual response (90 ms delayed spiking).

The above results suggest that in prism-fitted owls, visual responses (firing with a 90 ms delay) constitute the error signal driving plasticity (Gutfreund et al., 2002). Consequently, when visually displacing prisms are fitted onto owls, and spatially coincident, but prismatically misaligned audio-visual stimuli are presented, the ICXe neurons in juvenile owls presumably began to show the “visual response” (Fig. 4-3), thus triggering signals that ultimately lead to structural and functional plasticity. In Fig 4-3,

the prism is depicted as a thick yellow line between the stimuli and the brain of owls, and the prism-induced shift in visual input is depicted as a refraction of the blue line (visual input). In the absence of coincident audio input at neuron #1, there is a visual response in ICXe neuron #3 (blue shading). On the other hand, since ICXe neuron #9 receives just the audio input (as before), it displays an auditory response (orange shading).

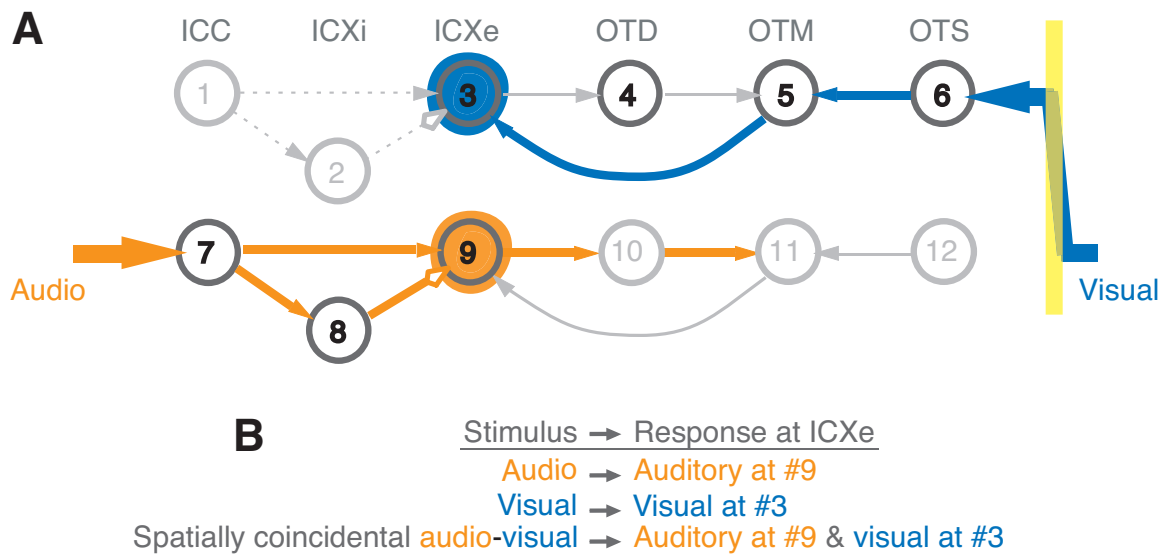


Figure 4-3. Schematic of the network immediately after prism-fitting.

(A) ICXe neuron #9 continues to receive the auditory information and to display the “auditory response” (orange shading), whereas the visual information from the same spatial location now arrives after prism-induced refraction at ICXe neuron #3, which displays the “visual response” as a result (blue shading). (B) Summary of network responses to various stimuli immediately after prism-fitting.

After several weeks, once the juvenile owl has adapted to the prism, the state of the network and its responses to stimuli are known to be as depicted in Fig. 4-4. Simultaneous and spatially coincident audio-visual inputs are shown as orange and blue squares, respectively (Fig. 4-4A). Due to the appropriate growth of new connections

between the ICC and the ICX (Fig. 4-4B), the receptor fields are matched once more, and audio-visual input arrives at ICXe neuron #3, resulting in just an auditory response (orange shading), and the visual response at neuron #3 is now quenched. Thus, after adaptation, the functioning of the network is as it was before the prism, with an absence of visual responses to audio-visual input.

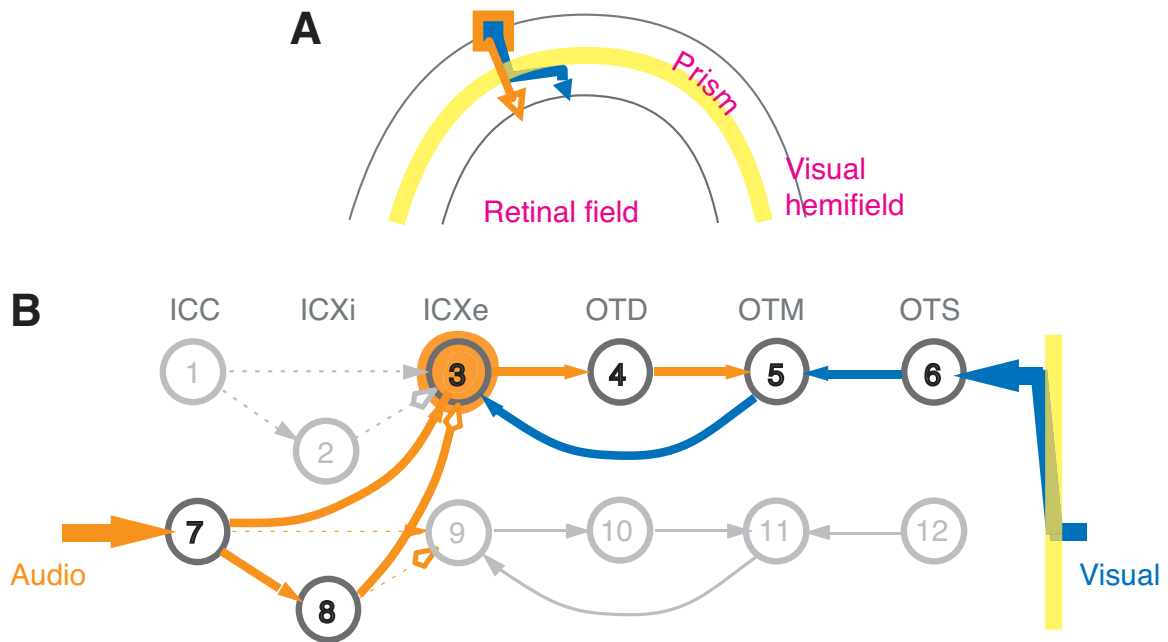


Figure 4-4. Schematic of the network after structural plasticity and behavioral adaptation to chronic prism exposure.

(A) Spatially colocalized audio (orange, open square) and visual (blue, filled square) stimuli are misaligned due to the prism (thick yellow arc), as seen by the refraction of the visual input (blue arrow). (B) New axons grow and synapses form between the ICC and the ICX, such that the auditory receptor fields of the ICXe neurons are shifted appropriately to match those at the ICC. Refracted visual input and redirected audio input arrive once again at the same neuron (#3), resulting in just the auditory response (orange shading).

Thus the “before prism” (Fig. 4-3) and “after prism” (Fig. 4-4) states of the auditory localization network are known. In order to understand prism-induced plasticity, the key question that remains to be answered is how the network goes from the former to the latter. Are the out-of-place visual responses that are not usually seen during the normal functioning of the network sufficient to drive the network to the post-prism state? If so, how? Given what we know about the working of neurons, and the physiological rules of plasticity, is there a consistent computational explanation for prism-induced plasticity? In the following sections, we show that the answers to all these questions are affirmative.

4.3 Modeling efforts in the literature

Various aspects of the auditory localization system in the barn owl have been studied in the context of modeling. Rosen et al. (1994) deal with the question of providing a computational explanation for prism-induced and ear-plug-induced plasticity. Gelfand et al. (1988) and Rucci et al. (1997) deal with audio-visual stimulus integration and motor response production in the auditory localization system. Pouget et al. (1995) deal specifically with the question of the site of plasticity (pre-synaptic to the ICX). All these models employ a connectionist framework with individual neurons modeled after linear (Gelfand et al., 1988) or non-linear (Pouget et al., 1995; Rosen et al., 1994; Rucci et al., 1997) activation units, and with no internal dynamics. Beyond a superficial resemblance to neurons, these models are not physiological. With the exception of Rosen et al., all the other models assume that the error signal is globally generated by foveation errors, whereas it has been shown (Hyde and Knudsen, 2001) to be a topographic template signal. Pouget et al. and Rucci et al. use reward-based learning schemes, for

which no evidence exists to date in the optic tectum or the inferior colliculus in the owl. Rosen et al. use the backpropagation learning scheme, which is considered in the field to be biologically implausible. In Gelfand et al., a correlation-based learning rule was used, but plasticity was found to occur between the ICX and OT neurons, and this is contradictory to experimental data (Knudsen, 2002). Until recently (Gutfreund et al., 2002), it was not known that the visually driven error signal does indeed arrive at the ICX neurons and that it is in the dynamics of the ICX activity that the error is embedded. Consequently, none of the above models account for this.

While these models are most relevant to our work, other studies exist that look at information-theoretic formalisms for audio-visual map registration and the plasticity therein (Atwal, 2004), and *de novo* development of an ITD-based representation of auditory space in the laminar nucleus (an early station in the ITD processing pathway) using an “axon-mediated spike-based learning rule” (Kempster et al., 2001).

Our goal in this work is the delineation of neurobiologically consistent computational mechanisms that can reconstruct the basal network activity and produce prism-induced plasticity, with a focus on the treatment of the visual error signal. Our first step in this modeling effort was a connectionist model with sigmoidal activation units and a Hebbian-like learning rule (Shultz et al., (in press)). The work here presents the second step in this modeling effort, with neurons that possess internal activation dynamics, and a spike-timing dependent rule for learning. As we show below, dynamics are critically important in most aspects of learning in the owl’s midbrain circuits, and spike-timing dependent plasticity, together with the error signal, automatically restricts the site of plasticity appropriately.

Spike-timing dependent plasticity (STDP) implements a learning rule that is a temporally asymmetric extension of the instantaneous, correlation-based synaptic modification idea of Hebb. Essentially, if a pre-synaptic neuron fires before its post-synaptic partner, then the synaptic coupling between these two cells is enhanced, whereas if the pre-synaptic cell fires after the post-synaptic one, then the coupling is weakened. There is a large body of experimental evidence that suggests that such a rule operates in various neural systems (reviewed in Bi and Poo, 2001). It has also been studied in neuronal models and its validity for investigating plasticity in spiking neurons established (Kepecs et al., 2002; Song et al., 2000).

4.4 Model

A. Assumptions

The model of network architecture that we use for the normal barn owl localization system is shown in Figs. 4-1 and 4-2 (Knudsen, 2002). As our focus is on understanding prism-induced plasticity in this system, and not on its *de novo* development, our starting point is the default network with the appropriately tuned neurons in the different layers. We make the simplifying assumption that ICC responses are purely ITD dependent (as opposed to being both frequency and ITD dependent). This does not critically affect the investigations in this paper. Further, for simplicity, we assume that neurons have all-or-none tuning curves, whereas in reality tuning curves are necessarily broader. Other than potentially affecting the magnitudes of individual synaptic conductances required for our results (see subsection D below), this does not impose any serious limitations on the conclusions drawn here. Each projection in the model is associated with a conduction delay, assumed to be between 0.5 and 1.5 ms. The

onset delays of auditory and visual responses at the ICXE neurons can be reasonably assumed to be processing delays that occur prior to the arrival of information at the OTS. They are implemented by introducing a 70 ms delay in the visual-processing pathway, and a 6 ms delay in the auditory-processing pathway. Input to the network is represented as the activity of ICC and OTS neurons. This activity is assumed to be in the form of 333 Hz spike trains lasting 25 ms.

B. The roles of inhibition

Inhibition plays three key roles in the functioning of the localization system. Firstly, there is a GABA_A-sensitive gate (presumably attentionally modulated) that blocks visual activity from arriving at the ICXE in anesthetized birds (Gutfreund et al., 2002). For simplicity, we do not include an explicit gate in the model, and this does not affect the results. Secondly, feedforward GABA_A inhibition serves to functionally inhibit new pathways in the early stages of learning, and the innate pathways in the post-adaptation phase (see Knudsen, 2002). Thus the balance of excitation and inhibition is modified over the course of learning to express one pathway predominantly over the other. Thirdly, we propose that the suppression of the ICXE visual response upon the presentation of aligned audio-visual input in normal owls is brought about by delayed and long-lasting feedforward inhibition. A good candidate mechanism for this is the action of GABA_B receptors. In the current model, synapses are represented as conductances with single-exponential time constants. It is therefore inconvenient to have both GABA_A and GABA_B dynamics at the same synapse. We choose to go with GABA_B-like inhibition as it is critical to the appropriate emergence of the error signal. Since the role of GABA_A is in the modulation of the excitation-inhibition balance as the network adapts, we have

omitted this in the current version of the model, without serious consequences for the validity of the results.

C. Neuron and plasticity model

Individual neurons are modeled after leaky integrate-and-fire units with conductance-based synapses. The membrane potential $V_j(t)$ of neuron j is updated as per

$$\tau_m \frac{dV_j(t)}{dt} = (V_{rest} - V_j(t)) + g_j^{exc}(t) * (E_{exc} - V_j(t)) + g_j^{inh}(t) * (E_{inh} - V_j(t))$$

with $V_{rest} = -70$ mV, $E_{exc} = 0$ mV, $E_{inh} = -70$ mV, $\tau_m = 5$ ms, and the spike-initiation threshold $V_{thr} = -54$ mV (Song et al., 2000). This version of the model is deterministic and we do not include any noise in the inputs. Synapses are indexed by their pre- and post-synaptic neuron labels, i.e., a synapse from neuron i onto neuron j is represented as (i,j) . $g_j^{exc}(t)$ and $g_j^{inh}(t)$ are the instantaneous excitatory and inhibitory conductances of neuron j (measured in units of the leakage conductance of the neuron; hence dimensionless), with τ_{inh} and τ_{exc} being the associated decay constants. The conductances are updated with STDP using the following equations (adapted from Song et al., 2000).

Synaptic conductances jump upon the arrival of a pre-synaptic spike following

$$\begin{aligned} g_j^{exc}(t) &= g_j^{exc}(t-1) + \delta_{ij}^{exc}(t) g_{i,j}^{peak}(t) \\ g_j^{inh}(t) &= g_j^{inh}(t-1) + \delta_{ij}^{inh}(t) g_{i,j}^{peak}(t) \end{aligned}$$

$\delta_{ij}^{exc(inh)}(t) = 1$, if (i, j) is an *exc(inh)* synapse and a spike from i arrives at (i, j) at time t

Synaptic conductances decay exponentially with time as

$$\tau_{exc} \frac{dg_j^{exc}(t)}{dt} = -g_j^{exc}(t), \quad \text{and} \quad \tau_{inh} \frac{dg_j^{inh}(t)}{dt} = -g_j^{inh}(t)$$

STDP counters that keep track of relative arrival times of pre- and post-synaptic spikes decay exponentially with time as

$$\tau_- \frac{dM_j(t)}{dt} = -M_j(t), \quad \text{and} \quad \tau_+ \frac{dP_{i,j}(t)}{dt} = -P_{i,j}(t)$$

STDP potentiation and depotentiation counters jump following

$$M_j(t) = M_j(t) - \alpha_{ij}^{exc(inh)}(t)A_-; P_{i,j}(t) = P_{i,j}(t) + \delta_{i,j}^{exc(inh)}(t)A_+;$$

$$\alpha_j^{exc(inh)}(t) = 1, \text{ if } (i, j) \text{ is an exc(inh) synapse and } j \text{ fires at time } t$$

STDP mediated synaptic potentiation occurs as

$$g_{i,j}^{peak}(t) = g_{i,j}^{peak}(t-1) + \alpha_j^{exc(inh)}(t)P_{i,j}(t)G^{peak_exc(inh)}, \quad \forall i, j$$

STDP mediated synaptic depotentiation occurs as

$$g_{i,j}^{peak}(t) = g_{i,j}^{peak}(t-1) + \delta_{ij}^{exc(inh)}(t)M_j(t)G^{peak_exc(inh)}, \quad \forall i, j$$

We permit inhibitory synapses to undergo plasticity as well, unlike in (Song et al., 2000).

The maximum peak conductances for excitatory synapses and inhibitory synapses are denoted as G^{peak_exc} and G^{peak_inh} , respectively. A_- and A_+ determine the amount by which synaptic weights change for each appropriate spike-pair, and τ_- and τ_+ are the associated decay constants. We assume that STDP effects from successive spike-pairs add linearly (Kepecs et al., 2002).

D. Choice of parameter values

The synaptic decay constant for excitatory synapses, τ_{exc} , is chosen to be 5 ms. Inhibitory synapses are endowed with a $\tau_{inh} = 100$ ms and a time to peak of 15 ms, in order to qualitatively model the action of GABA_B receptors. G^{peak_exc} and G^{peak_inh} are chosen to be 0.3 leakage-conductance units (Song et al., 2000). These values are an order of magnitude larger than in Song et al. (2000) because we need to ensure that pre-synaptic spikes at a single synapse are capable of eliciting post-synaptic spikes.

Consequently, A_+ and A_- are an order of magnitude lower with $A_+ = 0.0005$ and $A_-/A_+ = 1.05$ (several synapses between each pair of cells, and many-to-one anatomical projections will allow for lower values of $G^{peak_exc(inh)}$, and higher A_+ and A_- (within the range used in Song et al., 2000). It has been reported that with regards to plasticity, synapses in the innate pathway behave differently from synapses newly formed as a result of chronic prism experience (Knudsen, 2002). Particularly, the innate pathway persists in a fully adapted owl, although it is functionally inhibited. In order to account for this, the minimum values of peak conductances of innate synapses are set to be about half of $G^{peak_exc(inh)}$. Also, the A_+ value for these synapses is set to 0.001 (twice the value of newly formed synapses), with α being the same.

4.5 Results and predictions

All plots are generated with parameter values specified earlier. The neurons that will mainly interest us are the ICXe neurons #9 and #3. In the normal network, let the auditory and visual receptor fields of the appropriate neurons #1 through #6 be at spatial location A, and those of neurons #7 through #12 be in a neighboring location B that is 10 degrees to the right of A.

A. Responses in a normal network

Fig. 4-5 (top two panels) shows the voltage and spike traces in response to auditory input from location B (i.e., a spike train at neuron #7). The bottom two panels show responses to just visual input from location B (equivalent to a spike train at neuron #12). The auditory and visual responses have the correct latencies as clearly seen in the spike traces. Since the network is assumed to consist of point-to-point projections, neurons #1 through #6 do not respond to a stimulus presented to neuron #7. In response

to simultaneous, colocalized audio-visual input from location B in a normal network (equivalent to spike-train input to both #7 and #12), we see in Fig. 4-6 that ICXe neuron #9 displays just the auditory response. The visual input arriving at #9 through the OTM (#11) is successfully countered by the delayed inhibitory action of the auditory input. As seen in the third panel from the top, STDP does not produce any long-term changes to peak synaptic conductances.

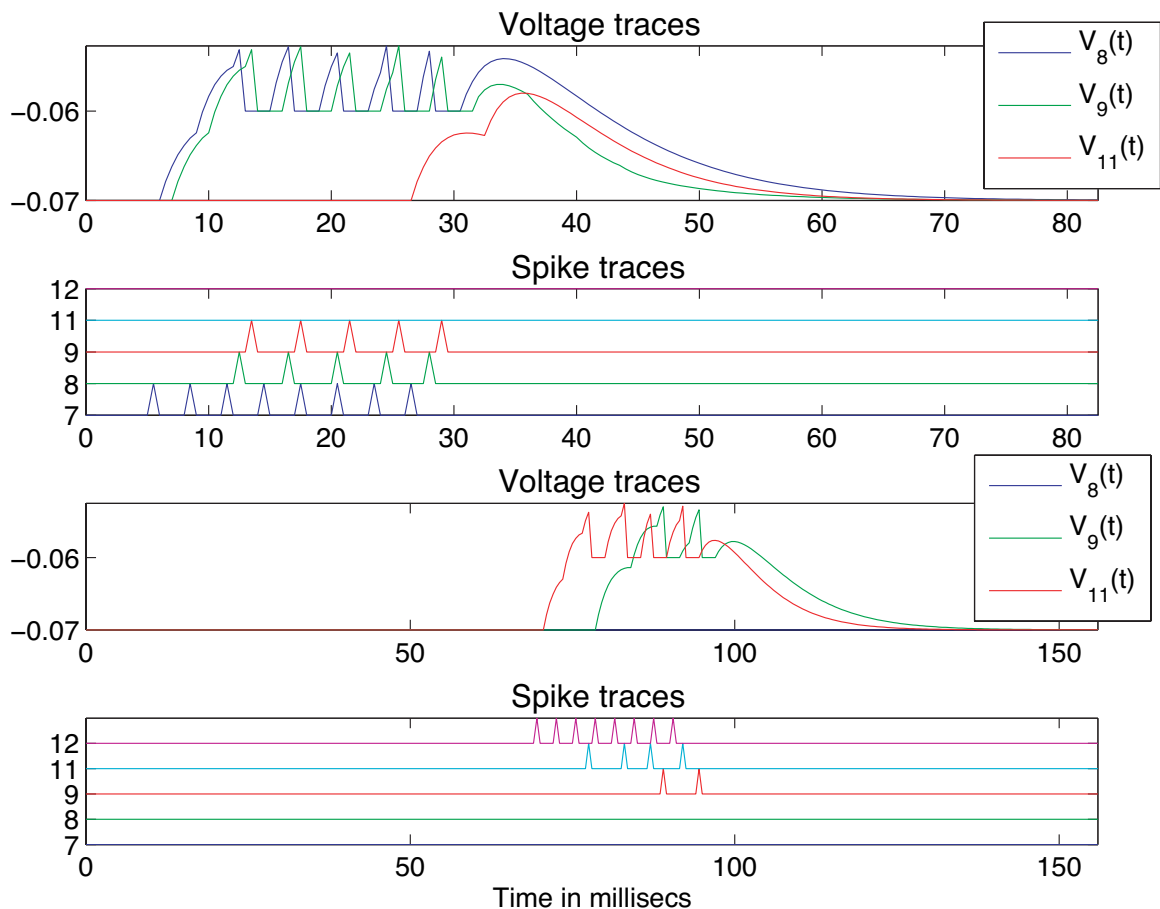


Figure 4-5. Plots of membrane potentials, and spike traces in a normal network when presented with unimodal stimulus.

Network response when just auditory input (top two panels), or just visual input (bottom two panels) is presented.

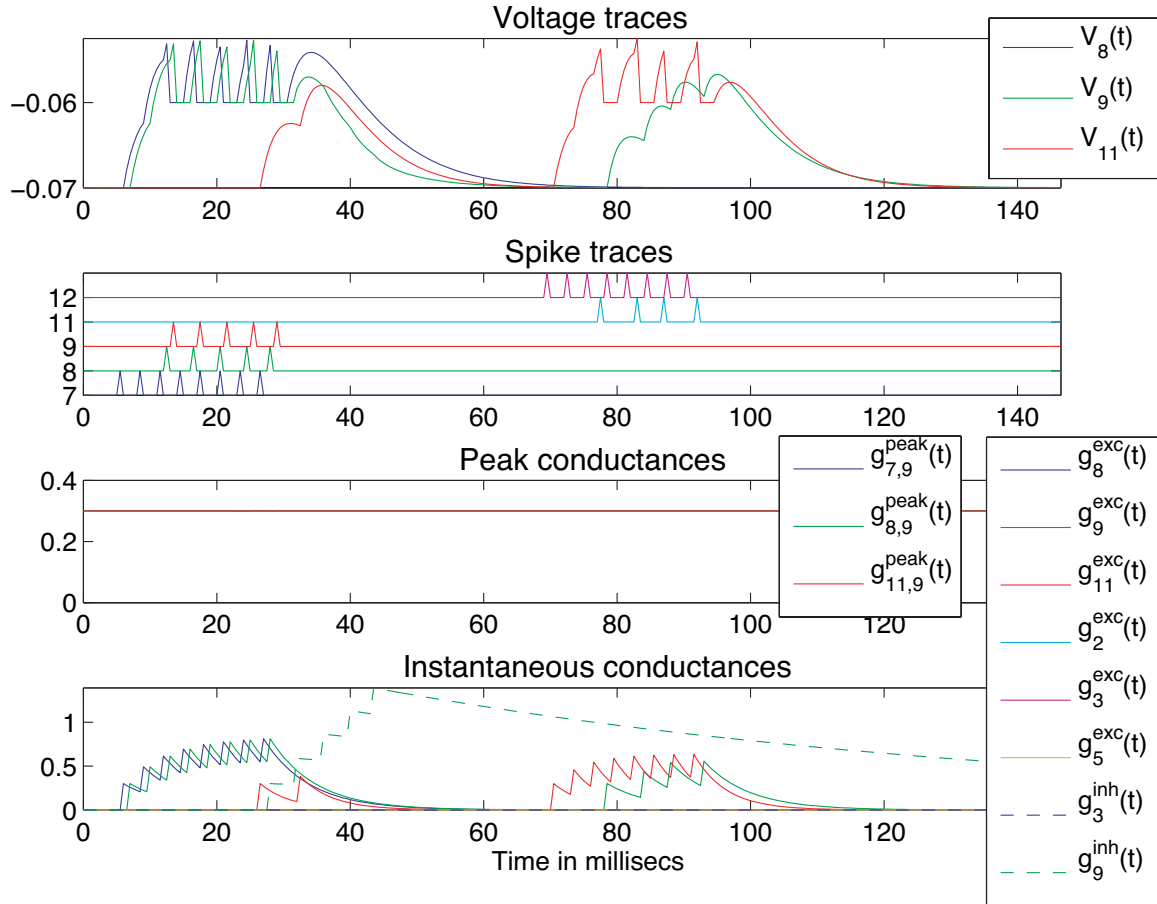


Figure 4-6. Results with synchronous and spatially coinciding audio-visual input to a normal network.

Along with voltage and spike traces, peak and instantaneous conductance traces are shown as well in response to audio-visual input.

B. Plasticity upon exposure to prism

Let prismatic spectacles that produce a 10-degree right shift be applied to the system. The top two panels in Fig. 4-7 show the results of simultaneous audio-visual presentation from location B. Auditory input arrives at neuron #7 as before; however, visual input now arrives at neuron #6 instead of neuron #12 because of prism-induced refraction. The response of ICXe #9 (which effectively receives just the auditory input) is just the auditory response, whereas that of ICXe #3, which receives just the visual input, is the “error signal.”

The next aspects to consider are structural and functional plasticity, which involve two qualitative steps. The first is axogenesis and synapse formation. The second is the potentiation, depotentiation, and pruning of the appropriate synapses in an activity-dependent manner so as to respond adaptively to prism experience.

We propose that modulation of the release of a diffusible factor, in the ICXe neurons that display the error response, is a plausible mechanism to implement the first step. Some candidate factors are arachidonic acid, neurotrophin-3, substance P, nerve growth factor (NGF), brain-derived neurotrophic factor (BDNF), and nitric oxide. These factors have been implicated in activity-dependent growth in several systems (Cohen-Cory and Fraser, 1995; Lessmann et al., 2003; Schmidt, 2004). We further suggest that the signal that might trigger this modification in synthesis and/or release is precisely the visual response. Close examination of the auditory and visual responses of single neurons (Fig. 4B, D, and F in Gutfreund et al., 2002) indicates that not only do the two responses differ in onset delay, but they also differ in their temporal firing pattern. The auditory response shows an initial burst, which is absent in the visual response. Since the only signal that appears to encode error is this visual response, the increased onset delay in this response could indicate the presence of an error, and facilitate STDP, whereas the abnormal firing pattern could encode the signal for diffusible factor release modulation.¹⁸

For the second step, synapses (7,3) and (8,3) need to be potentiated to produce functional adaptation, while innate synapses (1,3) and (2,3) need to get depotentiated. We propose that both are possible through STDP. The misaligned audio-visual input, as seen in the top two panels of Fig. 4-7, can produce potentiation since this input causes the

¹⁸We say “release modulation” because growth can be achieved either by the release of a trophic growth factor, or by the inhibition of the release of an anti-proliferating (like NO).

post-synaptic neuron (#3) to fire after its pre-synaptic partners (#7 and #9). Additionally, we propose that if audio-visual input is first presented at location B, and then immediately afterwards at location A, this results in the post-synaptic neuron (#3) firing before its pre-synaptic partners (#1 and #2), and can thereby produce depotentiation. The third and fourth panels in Fig. 4-7 show the voltage and spike traces in this scenario. How likely is such a sequential presentation of input required for depotentiation?

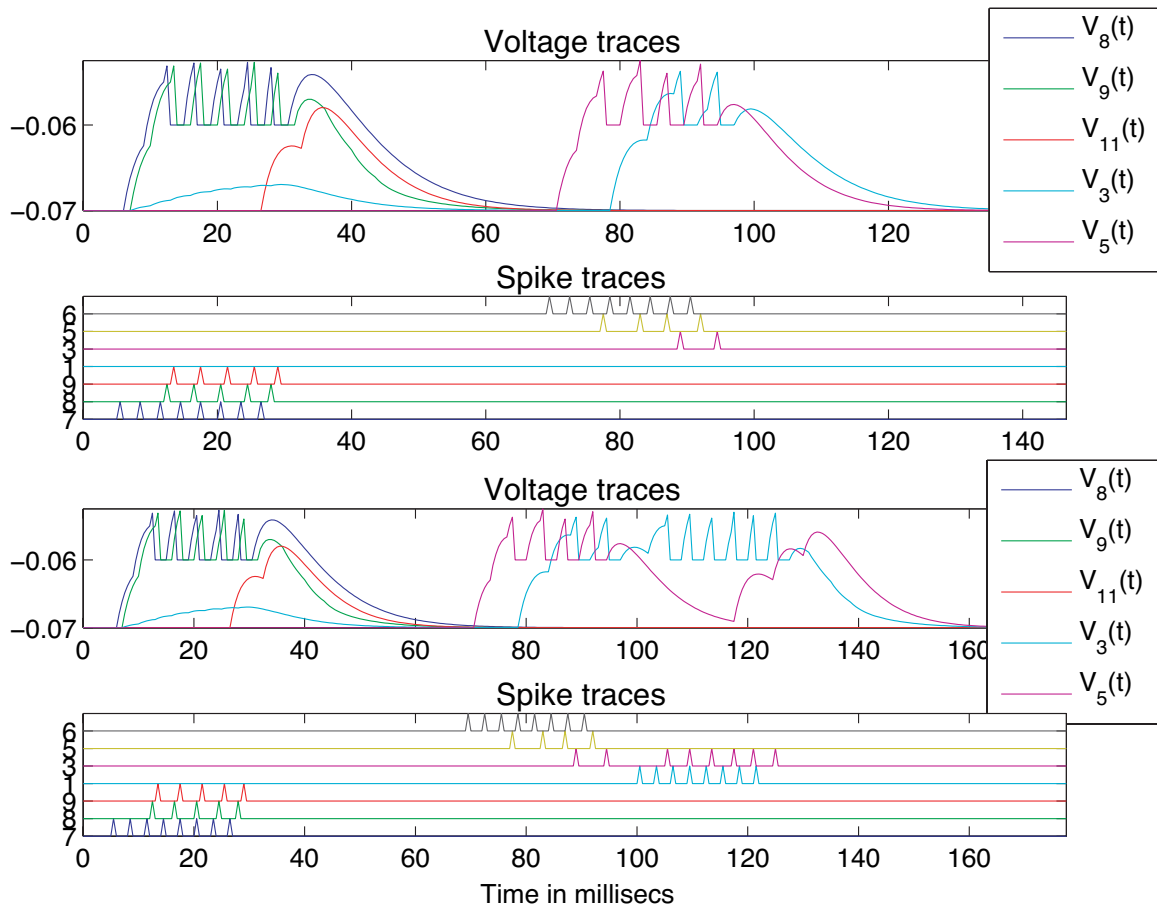


Figure 4-7. Mismatched input – potential and depotentiation of synapses.

Voltage and spike responses to mismatched input that produces potentiation of new synapses (top two panels), and responses to input that produces depotentiation of innate synapses (bottom two panels).

Given the topographic organization of the maps, and the fact that owls constantly move their heads, the conditional probability of input from location A following input from location B is low, but finite ($\leq 1/80$). Putting these arguments together, we present mismatched inputs from location B every 500 ms (which represents the most frequent presentation possible given the constraints imposed by the decay time constant of inhibition). Additionally, once every 80 presentations, this input is immediately followed by mismatched input from location A. The resulting synaptic plasticity is shown in Fig. 4-8, where peak conductances of (7,3) and (8,3) are potentiated, whereas those of (1,3) and (2,3) are depotentiated. Clearly, this plasticity can occur only as long as the error spikes persist. So once (7,3) and (8,3) are potentiated sufficiently such that auditory input at #7 arrives at #3, the visual error response is quenched, and the peak conductances stabilize. This is seen in a leveling off of $g_{7,3}^{peak}$, $g_{8,3}^{peak}$, $g_{1,3}^{peak}$, and $g_{2,3}^{peak}$ close to 5200 seconds in Fig. 4-8. Concomitantly, this can also turn off the processes mediating diffusible factor release modulation. The pruning of the inappropriate new synapses – (13,3), (14,3), and (11,3) in our case – can be also be accounted for in this framework by a combination of inactivity, slow potentiation, and competition.

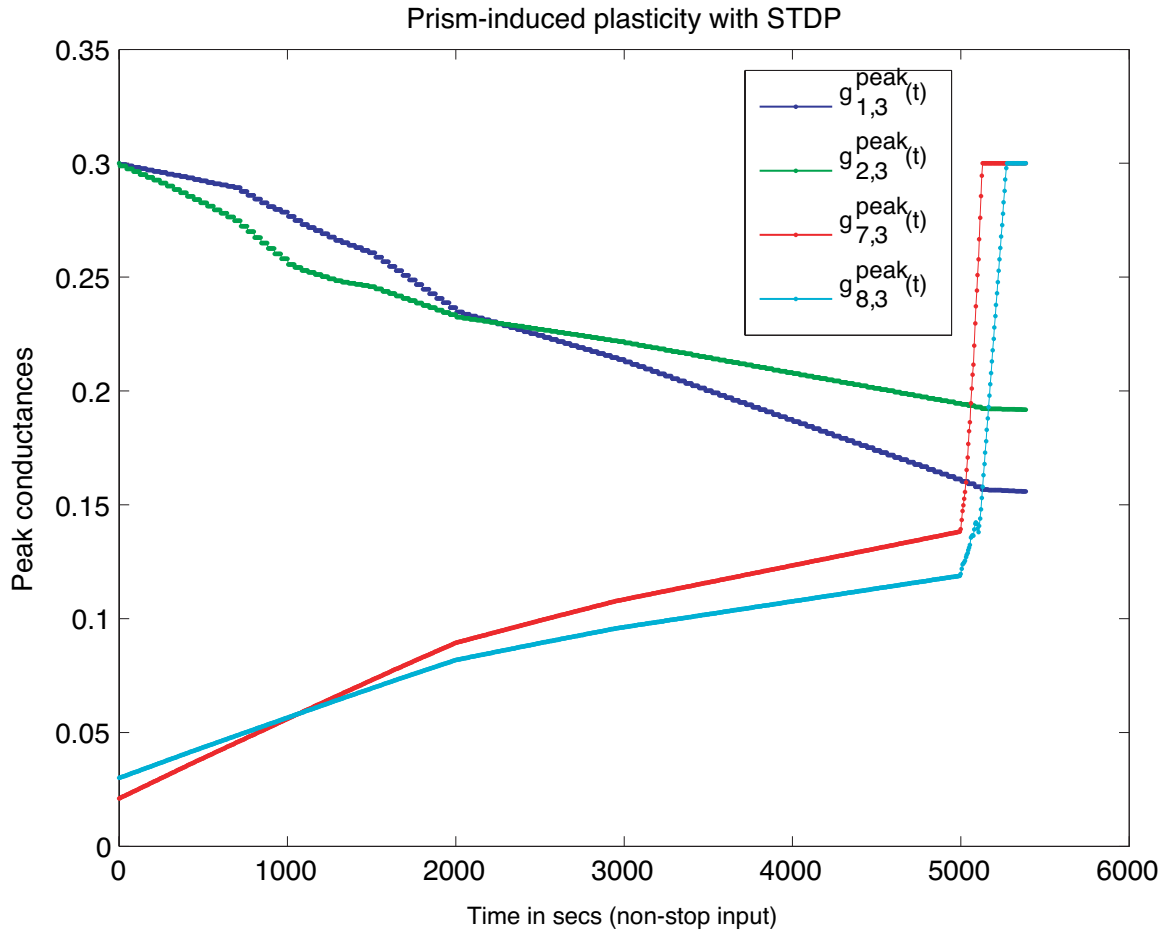


Figure 4-8. Potentiation and depotentiation of synapses.

Potentiation of new synapses (7,3) and (8,3), and depotentiation of innate synapses (1,3) and (2,3).

Given the parameters of the model, the fastest possible evolution of the weights with repeated (non-stop) input from location B occurs in about 5200 seconds (87 minutes) in neurons coding for location B (synapses onto neuron #3). Assuming that there are 80 neurons in each layer coding for 80 degrees of audio-visual space, and that the owl is exposed to adaptive stimuli for 12 hours a day, we estimate that behavioral adaptation will occur in approximately 10 days (which represents the lower bound). Additionally, Fig. 4-8 suggests that in the early stages of prism experience, the innate pathway dominates, whereas after adaptation, the innate pathway still remains, although

functionally inhibited. Experimental data show that adaptation takes about 7 weeks. Though our estimate is much lower than 7 weeks, it still qualitatively agrees with the experimental observation that plasticity is slow, and it represents the first such modeling estimate. This value will be critically affected by factors like A_+ values, other parameter values, actual time of prism exposure per day, and the number of discretized spatial locations coded for.

C. Predictions

We make three specific predictions. Firstly, axogenesis is controlled by the secretion modulation of a diffusible factor by the ICXE neurons. Further, the signal that triggers this event is encoded in the temporal firing pattern of the ICXE visual response. Secondly, the model predicts that in order to produce plasticity in the inhibitory pathway in the network, new connections must grow between the ICXI and ICXE neurons. The alternative of new connections between the ICC and ICXI (Knudsen, 2002) is not favored by the growth mechanism proposed. Thirdly, we predict that GABA_B receptors play a critical role in feedforward inhibition at the ICXI-ICXE synapses. Pharmacological blocking of these receptors should result in the ICXE visual response being manifest in response to aligned audio-visual input in normal owls.

4.6 Conclusions

Here, in our computational modeling of the barn owl auditory localization system, we demonstrate that with just a specification of biologically plausible synaptic parameters and neuronal activation dynamics, a Hebbian learning rule together with a mechanism to induce axo- and synaptogenesis can produce the appropriate network changes – potentiation, depotentiation, and pruning – that accompany prism-induced

behavioral adaptation. The parameters are chosen mainly such that the error-signal response is qualitatively accurate, and so that they are largely physiological (in cases where they deviate, they are easily corrected side-effects of the model assumptions as discussed in section 4.4). Having ensured this, the model is then able to account for other aspects of the data (like the site of plasticity) without being programmed for them explicitly. It also yields specific, testable predictions regarding the details of structural plasticity in the circuit.

4.7 Future directions

A key aspect that remains to be further investigated is the growth initiation mechanism. Whereas the current work has provided hints about how this may be brought about, we believe that a model with channel kinetics and biophysically detailed action-potential generation schemes will accord better control over temporal firing patterns (specifically, the initial burst in the auditory response), and can consequently shed light on the mechanistic details of growth initiation. Additionally, this will also facilitate looking at receptor composition changes (NMDA, AMPA, GABA_A) at individual synapses, which have been reported during the course of plasticity (Knudsen, 2002). Introducing broad tuning curves, a tonotopic organization in the ICC, and direct ITD coding in these neurons will be useful. We emphasize that computational investigations of this model system can lead to valuable insights about mechanisms driving structural plasticity and to experimentally useful predictions.

Chapter 5. General discussion

5.1 N-cadherin, spine dynamics, and structural plasticity

Synapse elimination occurs in the normal lifetime of a synapse (Holtmaat et al., 2005; Trachtenberg et al., 2002; Zuo et al., 2005) and in an experience-dependent manner (Holtmaat et al., 2006; Lendvai et al., 2000; Trachtenberg et al., 2002) *in vivo*. Spine loss and synapse elimination can modulate the functioning of a neuronal network either by weakening synaptic coupling or by altering the network connectivity pattern (Chklovskii et al., 2004; Poirazi and Mel, 2001; Stepanyants and Chklovskii, 2005). Indeed spine loss, among other structural pathologies, is associated with mental retardation (Fiala et al., 2002; Ramakers, 2002). With time-lapse imaging of hippocampal neurons, we have tracked the progression of structural events following acute surface N-cadherin disruption and monitored the events leading up to synapse loss. We show that more spines are first either motile or shorter, perhaps representing spines in different stages of instability following the loss of structural support at synapses. Motility has been suggested as a mechanism by which dendritic protrusions search for pre-synaptic partners (Dailey and Smith, 1996; Jontes and Smith, 2000; Wong and Wong, 2000). The increased motility we observe is consistent with such a scenario following N-cadherin disruption, and the shorter spines may represent the beginning of a withdrawal process following an inability to maintain synaptic contact. Subsequently, there is significant spine loss indicating an ongoing process of synaptic restructuring. While spine loss is statistically significant at 180 minutes, the trend for greater loss is evident even at 75 minutes, supporting the idea

of a graded, stage-wise response to structural disruption with different spines at different stages. While a reduction in spine length immediately preceding spine loss is to be expected, it does not necessitate loss, as evidenced by short spines that later elongate or otherwise persist. Therefore, the significant increase in correlation between early motility increases or spine shortening on the one hand and later loss on the other is indicative of a set of directed structural events following cadherin disruption. Loss may itself represent an intermediate step in a more long-term compensatory response that would involve the generation of filopodia (e.g., Togashi et al., 2002), spines, and then new, functional synapses.

Structural events preceding synapse formation were recently reported (Knott et al., 2006). However, the events preceding synapse elimination have been unknown. We have captured the events leading up to spine loss after N-cadherin disruption by tracking the probability distributions underlying stochastic spine behavior. Changes in these distributions allow us to discern relatively subtle structural effects, and we show that early increases in motility and reduction in spine length are indicators of later spine loss. Such characterization opens the door for understanding in greater detail the experience-dependent evolution of structural plasticity in neuronal circuits.

5.2 Architectural plasticity and representation construction: barn owls and beyond

In chapter 4, we have demonstrated that biophysically plausible models of both neuronal function and synaptic adaptation, together with a mechanism to bring about axo- and synaptogenesis, can produce the appropriate network changes and provide an explanation for behavioral adaptation in the barn owl auditory localization system. The

initial topographic organization of the auditory localization system suggests that structural plasticity may be necessary for the owl to adapt to experimentally induced visual displacement. Indeed, a temporally restricted developmental window for structural plasticity may be the reason adult owls are unable to adapt beyond a few degrees of shift (Brainard and Knudsen, 1998). An interesting question in this context is, what are the implications of this capacity for architectural change to the representational properties of the network in the context of the highly constrained neurobiological framework?

It appears that in this model system, experience-dependent architectural plasticity underlies abrupt qualitative change in the representational ability of the network. Further, this representational change typically increases the functional complexity of a network. Investigating the representational consequences of architectural plasticity necessitates the use of appropriate quantifiers of representational complexity. One way to quantify the “ability” or “complexity” of a network is in terms of its memory capacity (Poirazi and Mel, 2001), defined using a function-counting approach. We apply a similar approach to the midbrain auditory localization network in the barn owl by treating the auditory and visual inputs as the *input* to the network, and the activities of the ICX neurons as its *output*. If we assume for simplicity that every neuron codes uniquely for one degree in the visual (and auditory) field, and that each neuron in one layer projects uniquely to the corresponding neuron in another, then a simple calculation yields that the initial network architecture implements one input-output function, whereas the post-learning architecture (that results after a one-degree prism shift) implements a qualitatively different function. That is, structural plasticity has permitted an increase in the repertoire of localization functions that the network can compute from one to two, while satisfying topographic

projection constraints. According to this calculation scheme, the increase in memory capacity (or function complexity) possible in response to an n -degree prismatic shift in juvenile owls is n . We note here that the ability to grow introduces extra degrees of freedom in the input-output transformations in a manner that is consistent with the shift in the resulting output. That is, if the output units are considered to be linear for simplicity, then the input-output function between a pair of layers is a linear transformation (or a matrix), and the point-to-point nature of the anatomical projections constrain all off-diagonal elements of this matrix to be zero. Synaptic weight modifications just scale the diagonal elements, whereas growth permits the population of appropriate off-diagonal elements, resulting in qualitatively different functions. No amount of diagonal scaling can reproduce the latter effect. As a result, if there is no growth but only synaptic efficacy change, the memory capacity of the network and hence its representational complexity remain constant. This observation is consistent with the hypothesis that a lack of the ability to grow in adult circuits may be the reason adult owls (>200 days old) are unable to adapt to large visual shifts.

Viewed from the perspective of learning theory, the initial network represents the hypothesis space that is explored while learning from examples, and architectural plasticity allows the developing owl to go beyond this original hypothesis space to learn novel functions that are originally outside of this space. In contrast, the mature owl appears not to possess the same degree of architectural plasticity, and so is limited in terms of learning capacity. This highlights a distinct role of architectural plasticity as a form of constructive learning and illustrates why it is fundamentally different from synaptic weight change, which only implements a search within a given hypothesis space.

In conjunction with recent successes in using networks that grow to model cognitive development in humans (Buckingham and Shultz, 1996; Shultz, 2003; Shultz and Cohen, 2004; Shultz et al., (in press)), the data in thesis argue strongly that architectural plasticity is a powerful and indispensable ally in representation construction and sheds new light on mechanisms of structural plasticity in the brain, thereby contributing to our understanding of learning and memory.

References

- Aakalu, G., Smith, W. B., Jiang, C., Nguyen, N., and Schuman, E. M. (2001). Dynamic visualization of dendritic protein synthesis in hippocampal neurons. *Neuron* *30*, 489–502.
- Abe, K., Chisaka, O., Van Roy, F., and Takeichi, M. (2004). Stability of dendritic spines and synaptic contacts is controlled by alpha N-catenin. *Nat Neurosci* *7*, 357–363.
- Altman, J. (1962). Are new neurons formed in the brains of adult mammals? *Science* *135*, 1127–1128.
- Altman, J., and Das, G. D. (1965). Autoradiographic and histological evidence of postnatal hippocampal neurogenesis in rats. *J Comp Neurol* *124*, 319–335.
- Anastasiadis, P. Z., and Reynolds, A. B. (2001). Regulation of Rho GTPases by p120-catenin. *Curr Opin Cell Biol* *13*, 604–610.
- Atasoy, D., and Kavalali, E. T. (2006). Pre-synaptic unsilencing: searching for a mechanism. *Neuron* *50*, 345–346.
- Atwal, G. S. (2004). Dynamic plasticity in coupled avian midbrain maps. *Phys Rev E Stat Nonlin Soft Matter Phys* *70*, 061904.
- Bamji, S. X., Shimazu, K., Kimes, N., Huelsken, J., Birchmeier, W., Lu, B., and Reichardt, L. F. (2003). Role of beta-catenin in synaptic vesicle localization and pre-synaptic assembly. *Neuron* *40*, 719–731.
- Baum, E. B. (1988). Complete representations for learning from examples. In *Complexity in Information Theory*, Y. Abu-Mostafa, ed. (New York, NY: Springer-Verlag)
- Benson, D. L., and Tanaka, H. (1998). N-cadherin redistribution during synaptogenesis in hippocampal neurons. *J Neurosci* *18*, 6892–6904.

Berardi, N., Pizzorusso, T., and Maffei, L. (2004). Extracellular matrix and visual cortical plasticity: freeing the synapse. *Neuron* 44, 905–908.

Bi, G., and Poo, M. (2001). Synaptic modification by correlated activity: Hebb's postulate revisited. *Annu Rev Neurosci* 24, 139–166.

Black, J. E., Isaacs, K. R., Anderson, B. J., Alcantara, A. A., and Greenough, W. T. (1990). Learning causes synaptogenesis, whereas motor activity causes angiogenesis, in cerebellar cortex of adult rats. *Proc Natl Acad Sci USA* 87, 5568–5572.

Boggon, T. J., Murray, J., Chappuis-Flament, S., Wong, E., Gumbiner, B. M., and Shapiro, L. (2002). C-cadherin ectodomain structure and implications for cell adhesion mechanisms. *Science* 296, 1308–1313.

Bonhoeffer, T., and Yuste, R. (2002). Spine motility. Phenomenology, mechanisms, and function. *Neuron* 35, 1019–1027.

Bozdagi, O., Shan, W., Tanaka, H., Benson, D. L., Huntley, G. W. (2000). Increasing numbers of synaptic puncta during late-phase LTP: N-cadherin is synthesized, recruited to synaptic sites, and required for potentiation. *Neuron* 28, 245–259.

Braga, V. M. (2002). Cell-cell adhesion and signalling. *Curr Opin Cell Biol* 14, 546-556.

Braga, W. M. M., Machesky, L. M., Hall, A., and Hotchin, N. A. (1997). The small GTPases Rho and Rac are required for the establishment of cadherin-dependent cell-cell contacts. *J Cell Biol* 137, 1421–1431.

Brainard, M. S., and Knudsen, E. I. (1998). Sensitive periods for visual calibration of the auditory space map in the barn-owl optic tectum. *J Neurosci* 18, 3929–3942.

Buckingham, D., and Shultz, T. R. (1996). Computational power and realistic cognitive development. Paper presented at: Proceedings of the Eighteenth Annual Conference of the Cognitive Science Society (Mahwah, NJ: Erlbaum).

- Cabirol-Pol, M. J., Mizrahi, A., Simmers, J., and Meyrand, P. (2000). Combining laser scanning confocal microscopy and electron microscopy to determine sites of synaptic contact between two identified neurons. *J Neurosci Methods* 97, 175–181.
- Chang, P. L., Isaacs, K. R., and Greenough, W. T. (1991). Synapse formation occurs in association with the induction of long-term potentiation in two-year-old rat hippocampus in vitro. *Neurobiol Aging* 12, 517–522.
- Chklovskii, D. B., Mel, B. W., and Svoboda, K. (2004). Cortical rewiring and information storage. *Nature* 431, 782–788.
- Chuah, M. I., David, S., and Balschuk, O. (1991). Differentiation and survival of rat olfactory epithelial neurons in dissociated cell culture. *Devel Brain Res* 60, 123–132.
- Cohen-Cory, S., and Fraser, S. E. (1995). Effects of brain-derived neurotrophic factor on optic axon branching and remodelling in vivo. *Nature* 378, 192–196.
- Colicos, M. A., Collins, B. E., Sailor, M. J., and Goda, Y. (2001). Remodeling of synaptic actin induced by photoconductive stimulation. *Cell* 107, 605–616.
- Crick, F. (1982). Do dendritic spines twitch? *Trends Neurosci* 5, 44–46.
- Dailey, M. E., and Smith, S. J. (1996). The dynamics of dendritic structure in developing hippocampal slices. *J Neurosci* 16, 2983–2994.
- DeBello, W. M., Feldman, D. E., and Knudsen, E. I. (2001). Adaptive axonal remodeling in the midbrain auditory space map. *J Neurosci* 21, 3161–3172.
- DeBello, W. M., and Knudsen, E. I. (2004). Multiple sites of adaptive plasticity in the owl's auditory localization pathway. *J Neurosci* 24, 6853–6861.
- Dillon, C., and Goda, Y. (2005). The actin cytoskeleton: integrating form and function at the synapse. *Annu Rev Neurosci* 28, 25–55.
- Dougherty, R. P. (2005). Extensions of DAMAS and benefits and limitations of deconvolution in beamforming. Paper presented at: AIAA-2005-2961.

- Dunaevsky, A., Blazeski, R., Yuste, R., and Mason, C. (2001). Spine motility with synaptic contact. *Nat Neurosci* 4, 685-686.
- Dunaevsky, A., Tashiro, A., Majewska, A., Mason, C., and Yuste, R. (1999). Developmental regulation of spine motility in the mammalian central nervous system. *Proc Natl Acad Sci USA* 96, 13438–13443.
- Engert, F., and Bonhoeffer, T. (1999). Dendritic spine changes associated with hippocampal long-term synaptic plasticity. *Nature* 399, 66–70.
- Eriksson, P. S., Perfilieva, E., Bjork-Eriksson, T., Alborn, A. M., Nordborg, C., Peterson, D. A., and Gage, F. H. (1998). Neurogenesis in the adult human hippocampus. *Nat Med* 4, 1313–1317.
- Fannon, A. M., and Colman, D. R. (1996). A model for central synaptic junctional complex formation based on the differential adhesive specificities of the cadherins. *Neuron* 17, 423–434.
- Fiala, J. C., Feinberg, M., Popov, V., and Harris, K. M. (1998). Synaptogenesis via dendritic filopodia in developing hippocampal area CA1. *J Neurosci* 18, 8900–8911.
- Fiala, J. C., Spacek, J., and Harris, K. M. (2002). Dendritic spine pathology: cause or consequence of neurological disorders? *Brain Res Rev* 39, 29–54.
- Field, J., Nuir, D., Pilon, R., Sinclair, M., and Dodwell, P. (1980). Infants' orientation to lateral sounds from birth to three months. *Child Development* 51, 295–298.
- Fifkova, E., and Delay, R. J. (1982). Cytoplasmic actin in neuronal processes as a possible mediator of synaptic plasticity. *J Cell Biol* 95, 345–350.
- Fine, A., Amos, W. B., Durbin, R. M., and McNaughton, P. A. (1988). Confocal microscopy: applications in neurobiology. *Trends Neurosci* 11, 346–351.
- Fischer, M., Kaech, S., Knutti, D., and Matus, A. (1998). Rapid actin-based plasticity in dendritic spines. *Neuron* 20, 847–854.

Fischer, M., Karch, S., Wagner, U., Brinkhaus, H., and Matus, A. (2000). Glutamate receptors regulate actin based plasticity in dendritic spines. *Nat Neurosci* 3, 887–893.

Fodor, J. (1980). On the impossibility of learning “more powerful” structures. In *The Debate Between Jean Piaget and Noam Chomsky*, M. Piatelli-Palmarini, ed. (Routledge & Kegan Paul), pp. 142–152.

Fukata, M., and Kaibuchi, K. (2001). Rho-family GTPases in cadherin-mediated cell-cell adhesion. *Nat Rev Mol Cell Biol* 2, 887–897.

Gasparini, S., Saviane, C., Voronin, L. L., and Cherubini, E. (2000). Silent synapses in the developing hippocampus: lack of functional AMPA receptors or low probability of glutamate release? *Proc Natl Acad Sci USA* 97, 9741–9746.

Gelfland, J. J., Pearson, J. C., Spence, C. D., and Sullivan, W. E. (1988). Multisensor integration in biological systems. Paper presented at: 3rd IEEE Intl Symp Intell Control (Arlington, VA).

Geman, S., Bienenstock, E., and Doursat, R. (1992). Neural networks and the bias/variance dilemma. *Neural Comput* 4, 1–58.

Genovese, C. R., Lazar, N. A., and Nichols, T. (2002). Thresholding of statistical maps in functional neuroimaging using the false discovery rate. *Neuroimage* 15, 870–878.

Goda, Y. (2002). Cadherins communicate structural plasticity of pre-synaptic and post-synaptic terminals. *Neuron* 35, 1–3.

Gold, M. (1967). Language identification in the limit. *Information and Control* 10, 447–474.

Goldman, S. A., and Nottebohm, F. (1983). Neuronal production, migration, and differentiation in a vocal control nucleus of the adult female canary brain. *Proc Natl Acad Sci USA* 80, 2390–2394.

- Gould, E., and Gross, C. G. (2002). Neurogenesis in adult mammals: some progress and problems. *J Neurosci* 22, 619–623.
- Gould, E., Reeves, A. J., Graziano, M. S. A., and Gross, C. G. (1999). Neurogenesis in the neocortex of adult primates. *Science* 286, 548–552.
- Groc, L., Gustafsson, B., and Hanse, E. (2006). AMPA signalling in nascent glutamatergic synapses: there and not there! *Trends Neurosci* 29, 132–139.
- Gross, C. G. (2000). Neurogenesis in the adult brain: death of a dogma. *Nat Rev Neurosci* 1, 67–73.
- Grutzendler, J., Kasthuri, N., and Gan, W. B. (2002). Long-term dendritic spine stability in the adult cortex. *Nature* 420, 812–816.
- Gutfreund, Y., Zheng, W., and Knudsen, E. I. (2002). Gated visual input to the central auditory system. *Science* 297, 1556–1559.
- Halpain, S. (2000). Actin and the agile spine: how and why do dendritic spines dance? *Trends Neurosci* 23, 141–146.
- Harris, K. M. (1999). Structure, development, and plasticity of dendritic spines. *Curr Opin Neurobiol* 9, 343–348.
- Harris, K. M., Jensen, F. E., and Tsao, B. (1992). Three-dimensional structure of dendritic spines and synapses in rat hippocampus (CA1) at post-natal day 15 and adult ages: implications for the maturation of synaptic physiology and long-term potentiation. *J Neurosci* 12, 2685–2705.
- Hering, H., and Sheng, M. (2001). Dendritic spines, structure, dynamics and regulation. *Nat Rev Neurosci* 2, 880–888.
- Hibbs, A. R. (2000). *Confocal Microscopy for Biologists*, 3rd edn. (Ringwood East, Australia, BIOCON, Specialists in Confocal Microscopy).

Hirano, S., Kimoto, N., Shimoyama, Y., Hirohashi, S., Takeichi, M. (1992). Identification of a neural alpha-catenin as a key regulator of cadherin function and multicellular organization. *Cell* 70, 293–301.

Hirano, S., Suzuki, S. T., and Redies, C. (2003). The cadherin superfamily in neural development: diversity, function and interaction with other molecules. *Front Biosci* 8, 306–355.

Holtmaat, A., Wilbrecht, L., Knott, G. W., Welker, E., and Svoboda, K. (2006). Experience-dependent and cell-type-specific spine growth in the neocortex. *Nature* 441, 979–983.

Holtmaat, A. J., Trachtenberg, J. T., Wilbrecht, L., Shepherd, G. M., Zhang, X., Knott, G. W., and Svoboda, K. (2005). Transient and persistent dendritic spines in the neocortex in vivo. *Neuron* 45, 279–291.

Hyde, P. S., and Knudsen, E. I. (2001). A topographic instructive signal guides the adjustment of the auditory space map in the optic tectum. *J Neurosci* 21, 8586–8593.

Inoue, A., and Okabe, S. (2003). The dynamic organization of post-synaptic proteins: translocating molecules regulate synaptic function. *Curr Opin Neurobiol* 13, 332–340.

Jontes, J. D., Emond, M. R., and Smith, S. J. (2004). In vivo trafficking and targeting of N-cadherin to nascent pre-synaptic terminals. *J Neurosci* 24, 9027–9034.

Jontes, J. D., and Smith, S. J. (2000). Filopodia, spines, and the generation of synaptic diversity. *Neuron* 27, 11–14.

Kandel, E. R., Schwartz, J. H., and Jessell, T. M. (2000). *Principles of Neural Science*, 4th edn. (New York, NY: Mc-Graw Hill).

Kempermann, G., Kuhn, H. G., and Gage, F. H. (1997). More hippocampal neurons in adult mice living in an enriched environment. *Nature* 386, 493–495.

Kempster, R., Leibols, C., Wagner, H., and Hemmen, J. L. v. (2001). Formation of temporal-feature maps by axonal propagation of synaptic learning. *Proc Natl Acad Sci USA* 98, 4166–4171.

Kennedy, M. B. (2000). Signal-processing machines at the post-synaptic density. *Science* 290, 750–754.

Kepecs, A., van Rossum, M. C. W., Song, S., and Tegner, J. (2002). Spike-timing-dependent plasticity: common themes and divergent vistas. *Biol Cybern* 87, 446–458.

Kleim, J. A., Freeman, J. H., Jr., Bruneau, R., Nolan, B. C., Cooper, N. R., Zook, A., and Walters, D. (2002). Synapse formation is associated with memory storage in the cerebellum. *Proc Natl Acad Sci USA* 99, 13228–13231.

Knafo, S., Grossman, Y., Barkai, E., and Benshalom, G. (2001). Olfactory learning is associated with increased spine density along apical dendrites of pyramidal neurons in the rat piriform cortex. *Eur J Neurosci* 13, 633–638.

Knott, G. W., Holtmaat, A., Wilbrecht, L., Welker, E., and Svoboda, K. (2006). Spine growth precedes synapse formation in the adult neocortex in vivo. *Nat Neurosci* 9, 1117–1124.

Knott, G. W., Quairiaux, C., Genoud, C., and Welker, E. (2002). Formation of dendritic spines with GABAergic synapses induced by whisker stimulation in adult mice. *Neuron* 34, 265–273.

Knudsen, E. I. (1998). Capacity for plasticity in the adult owl auditory system expanded by juvenile experience. *Science* 279, 1531–1533.

Knudsen, E. I. (2002). Instructed learning in the auditory localization pathway of the barn owl. *Nature* 417, 322–328.

Knudsen, E. I., and Brainard, M. S. (1995). Creating a unified representation of visual and auditory space in the brain. *Annu Rev Neurosci* 18, 19–43.

- Knudsen, E. I., Esterly, S. D., and du Lac, S. (1991). Stretched and upside-down maps of auditory space in the optic tectum of blind-reared owls: acoustic basis and behavioral correlates. *J Neurosci* *11*, 1727–1747.
- Koh, I. Y., Lindquist, W. B., Zito, K., Nimchinsky, E. A., and Svoboda, K. (2002). An image analysis algorithm for dendritic spines. *Neural Comput* *14*, 1283–1310.
- Korkotian, E., and Segal, M. (2001). Spike-associated fast contraction of dendritic spines in cultured hippocampal neurons. *Neuron* *30*, 751–758.
- Kornack, D., and Rakic, P. (1999). Continuation of neurogenesis in the hippocampus of the adult macaque monkey. *Proc Natl Acad Sci USA* *96*, 5768–5773.
- Lamprecht, R., and LeDoux, J. (2004). Structural plasticity and memory. *Nat Rev Neurosci* *5*, 45–54.
- Lang, C., Barco, A., Zablow, L., Kandel, E. R., Siegelbaum, S. A., and Zakharenko, S. S. (2004). Transient expansion of synaptically connected dendritic spines upon induction of hippocampal long-term potentiation. *Proc Natl Acad Sci USA* *101*, 16665–16670.
- Lendvai, B., Stern, E. A., Chen, B., and Svoboda, K. (2000). Experience-dependent plasticity of dendritic spines in the developing rat barrel cortex in vivo. *Nature* *404*, 876–881.
- Lessmann, V., Gottmann, K., and Malcangio, M. (2003). Neurotrophin secretion: current facts and future prospects. *Prog Neurobiol* *69*, 341–374.
- Lestrel, P. E., ed. (1997). *Fourier Descriptors and Their Applications in Biology* (New York, NY: Cambridge University Press).
- Leuner, B., Falduto, J., and Shors, T. J. (2003). Associative memory formation increases the observation of dendritic spines in the hippocampus. *J Neurosci* *23*, 659–665.
- Linkenhoker, B. A., and Knudsen, E. I. (2002). Incremental training increases the plasticity of the auditory space map in adult barn owls. *Nature* *419*, 293–296.

- Lipkind, D., Nottebohm, F., Rado, R., and Barnea, A. (2002). Social change affects the survival of new neurons in the forebrain of adult songbirds. *Behav Brain Res* *133*, 31–43.
- Lippincott-Schwartz, J., Altan-Bonnet, N., and Patterson, G. H. (2003). Photobleaching and photoactivation: following protein dynamics in living cells. *Nat Cell Biol Suppl*, S7–14.
- Lippincott-Schwartz, J., and Patterson, G. H. (2003). Development and use of fluorescent protein markers in living cells. *Science* *300*, 87–91.
- Magie, C. R., Pinto-Santini, D., and Parkhurst, S. M. (2002). Rho1 interacts with p120ctn and alpha-catenin, and regulates cadherin-based adherens junction components in *drosophila*. *Development* *129*, 3771–3782.
- Majewska, A., and Sur, M. (2003). Motility of dendritic spines in visual cortex in vivo: changes during the critical period and effects of visual deprivation. *Proc Natl Acad Sci USA* *100*, 16024–16029.
- Majewska, A., Tashiro, A., and Yuste, R. (2000). Regulation of spine calcium dynamics by rapid spine motility. *J Neurosci* *20*, 8262–8268.
- Maletic-Savatic, M., Malinow, R., and Svoboda, K. (1999). Rapid dendritic morphogenesis in CA1 hippocampal dendrites induced by synaptic activity. *Science* *283*, 1923–1927.
- Maletic-Savatic, M., Malinow, R., Svoboda, K. (1999). Rapid dendritic morphogenesis in CA1 hippocampal dendrites induced by synaptic activity. *Science* *283*, 1923–1927.
- Malinow, R., and Malenka, R. C. (2002). AMPA receptor trafficking and synaptic plasticity. *Ann Rev Neurosci* *25*, 103–126.
- Martin, S. J., and Morris, R. G. M. (2002). New life to an old idea: The synaptic plasticity and memory hypothesis revisited. *Hippocampus* *12*, 609–636.

- Matsuzaki, M., Honkura, N., Ellis-Davies, G. C., and Kasai, H. (2004). Structural basis of long-term potentiation in single dendritic spines. *Nature* 429, 761–766.
- Matus, A. (2000). Actin-based plasticity in dendritic spines. *Science* 290, 754–758.
- Michalet, X., Kapanidis, A. N., Laurence, T., Pinaud, F., Doose, S., Pflughoeft, M., and Weiss, S. (2003). The power and prospects of fluorescence microscopies and spectroscopies. *Annu Rev Biophys Biomol Struct* 32, 161–182.
- Micheva, K. D., and Beaulieu, C. (1995). An anatomical substrate for experience-dependent plasticity of the rat barrel field cortex. *Proc Natl Acad Sci USA* 92, 11834–11838.
- Miyawaki, A., Sawano, A., and Kogure, T. (2003). Lighting up cells: labelling proteins with fluorophores. *Nat Cell Biol Suppl*, S1–7.
- Mizrahi, A., and Katz, L. C. (2003). Dendritic stability in the adult olfactory bulb. *Nat Neurosci* 6, 1201–1207.
- Moser, M. B., Trommald, M., Egeland, T., and Andersen, P. (1997). Spatial training in a complex environment and isolation alter the spine distribution differently in rat CA1 pyramidal cells. *J Comp Neurol* 380, 373–381.
- Murase, S., Mosser, E., and Schuman, E. M. (2002). Depolarization drives β -catenin into neuronal spines promoting changes in synaptic structure and function. *Neuron* 35, 91–105.
- Mysore, S. P. (1999) Issues of Representation, Detection, Prediction, and Classification in the Context of Machine Condition Monitoring and Shape Analysis, M. S. Thesis, The Pennsylvania State University, University Park.
- Müller, T., Cohidas, A., Reichmann, E., and Ullrich, A. (1999). Phosphorylation and free pool of β -catenin are regulated by tyrosine kinases and tyrosine phosphatases during epithelial cell migration. *J Biol Chem* 274, 10173–10183.

- Nagafuchi, A., Ishihara, S., and Tsukita, S. (1994). The roles of catenins in the cadherin-mediated cell adhesion functional analysis of E-cadherin- α -catenin fusion molecules. *J Cell Biol* 127, 235-245.
- Nagerl, U. V., Eberhorn, N., Cambridge, S. B., and Bonhoeffer, T. (2004). Bidirectional activity-dependent morphological plasticity in hippocampal neurons. *Neuron* 44, 759–767.
- Neuhoff, H., Roeper, J., and Schweizer, M. (1999). Activity-dependent formation of perforated synapses in cultured hippocampal neurons. *Eur J Neurosci* 11, 4241–4250.
- Nguyen, T., and Sudhof, T. C. (1997). Binding properties of neuroligin 1 and neurexin 1-beta reveal function as heterophilic cell adhesion molecules. *J Biol Chem* 272, 26032–26039.
- Nimchinsky, E. A., Sabatini, B. L., and Svoboda, K. (2002). Structure and function of dendritic spines. *Annu Rev Physiol* 64, 313–353.
- Nottebohm, F. (1985). Neuronal replacement in adulthood. *Ann N Y Acad Sci* 457, 143–161.
- Nowakowski, R. S., and Hayes, N. L. (2000). New neurons: extraordinary evidence or extraordinary conclusions. *Science* 288, 771.
- Okabe, T., Nakamura, T., Nishimura, Y. N., Kohu, K., Ohwada, S., Morishita, Y., and Akiyama, T. (2003). RICS, a novel GTPase-activating protein for Cdc42 and Rac1, is involved in the beta-catenin-N-cadherin and N-methyl-D-aspartate receptor signaling. *J Biol Chem* 278, 9920–9927.
- Okamoto, K., Nagai, T., Miyawaki, A., and Hayashi, Y. (2004). Rapid and persistent modulation of actin dynamics regulates post-synaptic reorganization underlying bidirectional plasticity. *Nat Neurosci* 7, 1104–1112.
- Oppenheim, A. V., Schaffer, R. W., and Buck, J. R. (1999). *Discrete-Time Signal Processing*, 2nd edn. (Upper Saddle River, NJ: Prentice Hall).

Oray, S., Majewska, A., and Sur, M. (2004). Dendritic spine dynamics are regulated by monocular deprivation and extracellular matrix degradation. *Neuron* 44, 1021–1030.

Overstreet-Wadiche, L. S., Bensen, A. L., and Westbrook, G. L. (2006). Delayed development of adult-generated granule cells in dentate gyrus. *J Neurosci* 26, 2326–2334.

Ozawa, M., and Kemler, R. (1998). The membrane-proximal region of the E-cadherin cytoplasmic domain prevents dimerization and negatively regulates adhesion activity. *J Cell Biol* 142, 1605–1613.

Ozawa, M., Ringwald, M., and Kemler, R. (1990a). Uvomorulin-catenin complex formation is regulated by a specific domain in the cytoplasmic region of the cell adhesion molecule. *Proc Natl Acad Sci USA* 87, 4246–4250.

Parnass, Z., Tashiro, A., and Yuste, R. (2000). Analysis of spine morphological plasticity in developing hippocampal pyramidal neurons. *Hippocampus* 10, 561–568.

Paton, J. A., and Nottebohm, F. N. (1984). Neurons generated in the adult brain are recruited into functional circuits. *Science* 225, 1046–1048.

Peters, A., and Kaiserman-Abramof, I. R. (1970). The small pyramidal neuron of the rat cerebral cortex. The perikaryon, dendrites and spines. *Am J Anat* 127, 321–55.

Peters, A., Palay, S. L., and Webster, H. D. (1991). *The Fine Structure of the Nervous System* (New York, NY: Oxford University Press).

Phend, K. D., Rustioni, A., and Weinberg, R. J. (1995). An osmium-free method of epon embedding that preserves both ultrastructure and antigenicity for post-embedding immunocytochemistry. *J Histochem Cytochem* 43, 283–292.

Phend, K. D., Weinberg, R. J., and Rustioni, A. (1992). Techniques to optimize post-embedding single and double staining for amino acid neurotransmitters. *J Histochem Cytochem* 40, 1011–1020.

Piaget, J. (1970). *Genetic Epistemology* (New York, NY: Columbia University Press).

- Piaget, J. (1980). *Adaptation and Intelligence: Organic Selection and Phenocopy* (Chicago, IL: University of Chicago Press).
- Poirazi, P., and Mel, B. W. (2001). Impact of active dendrites and structural plasticity on the memory capacity of neural tissue. *Neuron* 29, 779–796.
- Pouget, A., Deffayet, C., and Sejnowski, T. J. (1995). Reinforcement learning predicts the site of plasticity for auditory remapping in the barn owl. In *Advances in Neural Information Processing Systems 7*, G. Tesauro, D. Touretzky, and T. Leen, eds. (Cambridge, MA: MIT Press).
- Quartz, S. R. (1993). Neural networks, nativism, and the plausibility of constructivism. *Cognition* 48, 223–242.
- Quartz, S. R., and Sejnowski, T. J. (1997). The neural basis of cognitive development: a constructivist manifesto. *Behav Brain Sci* 20, 537–556; discussion, 556–596.
- Rakic, P. (2002). Neurogenesis in the adult primate neocortex: an evaluation of the evidence. *Nat Rev Neurosci* 3, 65–71.
- Ramakers, G. J. (2002). Rho proteins, mental retardation and the cellular basis of cognition. *Trends Neurosci* 25, 191–199.
- Ramirez-Amaya, V., Escobar, M. L., Chao, V., and Bermudez-Rattoni, F. (1999). Synaptogenesis of mossy fibers induced by spatial water maze overtraining. *Hippocampus* 9, 631–636.
- Redies, C. (2000). Cadherins in the central nervous system. *Prog Neurobiol* 61, 611–648.
- Redies, C., Inuzuka, H., and Takeichi, M. (1992). Restricted expression of N- and R-cadherin on neurites of the developing chicken CNS. *J Neurosci* 12, 3525–3534.
- Rosen, D. J., Rumelhart, D. E., and Knudsen, E. I. (1994). A connectionist model of the owl's sound localization system. In *Advances in Neural Information Processing Systems 6*, G. Tesauro, D. S. Touretzky and T. K. Leen, eds. (Cambridge, MA: MIT Press).

- Roura, S., Miravet, S., Piedra, J., de Harreors, A. G., and Muñach, M. (1999). Regulation of E-cadherin/catenin association by tyrosine phosphorylation. *J Biol Chem* 274, 36734–36740.
- Rucci, M., Tononi, G., and Edelman, G. M. (1997). Registration of neural maps through value-dependent learning: modeling the alignment of auditory and visual maps in the barn owl's optic tectum. *J Neurosci* 17, 334–352.
- Rusakov, D. A., and Stewart, M. G. (1995). Quantification of dendritic spine populations using image analysis and a tilting disector. *J Neurosci Methods* 60, 11–21.
- Sala, C., Piech, V., Wilson, N. R., Passafaro, M., Liu, G., and Sheng, M. (2001). Regulation of dendritic spine morphology and synaptic function by Shank and Homer. *Neuron* 31, 115–130.
- Salinas, P. C., and Price, S. R. (2005). Cadherins and catenins in synapse development. *Curr Opin Neurobiol* 15, 73–80.
- Sanai, N., Tramontin, A. D., Quinones-Hinojosa, A., Barbaro, N. M., Gupta, N., Kunwar, S., Lawton, M. T., McDermott, M. W., Parsa, A. T., Manuel-Garcia Verdugo, J., et al. (2004). Unique astrocyte ribbon in adult human brain contains neural stem cells but lacks chain migration. *Nature* 427, 740–744.
- Sara, Y., Virmani, T., Deak, F., Liu, X., and Kavalali, E. T. (2005). An isolated pool of vesicles recycles at rest and drives spontaneous neurotransmission. *Neuron* 45, 563–573.
- Schmidt, J. T. (2004). Activity-driven sharpening of the retinotectal projection: the search for retrograde synaptic signaling pathways. *J Neurobiol* 59, 114–133.
- Schuman, E. M., and Murase, S. (2003). Cadherins and synaptic plasticity: activity-dependent cyclin-dependent kinase 5 regulation of synaptic beta-catenin-cadherin interactions. *Philos Trans R Soc Lond B Biol Sci* 358, 749–756.
- Shapiro, L., and Colman, D. R. (1999). The diversity of cadherins and implications for a synaptic adhesive code in the CNS. *Neuron* 23, 427–430.

Shepherd, G. M., ed. (1998). *The Synaptic Organization of the Brain*, 4th edn. (New York, NY: Oxford University Press).

Shepherd, G. M., and Koch, C. (1998). Introduction to synaptic circuits. In *The Synaptic Organization of the Brain*, G. M. Shepherd, ed. (New York, NY: Oxford University Press).

Shimoyama, Y., Tsujimoto, G., Kitajima, M., and Natori, M. (2000). Identification of three human type-II classic cadherins and frequent heterophilic interactions between different subclasses of type-II classic cadherins. *Biochem J* 349, 159–167.

Shultz, T. R. (2003). *Computational Developmental Psychology* (Cambridge, MA: MIT Press).

Shultz, T. R., and Cohen, L. B. (2004). Modeling age differences in infant category learning. *Infancy* 5, 153–171.

Shultz, T. R., Mysore, S. P., and Quartz, S. R. (in press). Why let networks grow? In *Constructing Cognition: How the Brain Develops Representations*, D. Mareschal, S. Sirois, and G. Westermann, eds. (Oxford, UK: Oxford University Press).

Shultz, T. R., Schmidt, W. C., Buckingham, D., and Mareschal, D. (1995). Modeling cognitive development with a generative constructionist algorithm. In *Developing Cognitive Competence: New Approaches to Process Modeling*, T. J. Simon, and G. S. Halford, eds. (Hillsdale, NJ: Erlbaum).

Sirois, S., and Shultz, T. R. (1999). Learning, development, and nativism: connectionist implications. Paper presented at: Twenty-first Annual Conference of the Cognitive Science Society (Mahwah, NJ: Erlbaum).

Song, S., Miller, K. D., and Abbott, L. F. (2000). Competitive Hebbian learning through spike-timing-dependent synaptic plasticity. *Nat Neurosci* 3, 919–926.

Sorra, K. E., and Harris, K. M. (2000). Overview on the structure, composition, function, development, and plasticity of hippocampal dendritic spines. *Hippocampus* 10, 501–511.

- Sotelo, C. (1990). Cerebellar synaptogenesis: what we can learn from mutant mice. *J Exp Biol* 153, 225–249.
- Stanfield, B. B., and Trice, J. E. (1988). Evidence that granule cells generated in the dentate gyrus of adult rats extend axonal projections. *Exp Brain Res* 72, 399–406.
- Stepanyants, A., and Chklovskii, D. B. (2005). Neurogeometry and potential synaptic connectivity. *Trends Neurosci* 28, 387–394.
- Stewart, M. G., and Rusakov, D. A. (1995). Morphological changes associated with stages of memory formation in the chick following passive avoidance training. *Behav Brain Res* 66, 21–28.
- Sullivan, K. F., and Kay, S. A., eds. (1999). *Green Fluorescent Proteins* (San Diego, CA: Academic Press).
- Tada, T., and Sheng, M. (2006). Molecular mechanisms of dendritic spine morphogenesis. *Curr Opin Neurobiol* 16, 95–101.
- Takeichi, M. (1991). Cadherin cell adhesion receptor as a morphogenetic regulator. *Science* 251, 1451–1455.
- Takeichi, M., and Abe, K. (2005). Synaptic contact dynamics controlled by cadherin and catenins. *Trends Cell Biol* 15, 216–221.
- Takeichi, M., Uemura, T., Iwai, Y., Uchida, N., Inoue, T., Tanaka, T., and Suzuki, S. C. (1997). Cadherins in brain patterning and neural network formation. *Cold Spring Harbor Symp Quant Biol* 62, 505–510.
- Tanaka, H., Shan, W., Phillips, G. R., Arndt, K., Bozdagi, O., Shapiro, L., Huntley, G. W., Benson, D. L., Colman, D. R. (2000). Molecular modification of N-cadherin in response to synaptic activity. *Neuron* 25, 93–107.
- Tang, L., Hung, C. P., and Schuman, E. M. (1998). A role for the cadherin family of cell adhesion molecules in hippocampal long-term potentiation. *Neuron* 20, 1165–1175.

- Tang, Y., Nyengaard, J. R., De Groot, D. M., and Gundersen, H. J. (2001). Total regional and global number of synapses in the human brain neocortex. *Synapse* 41, 258–273.
- Tashiro, A., and Yuste, R. (2004). Regulation of dendritic spine motility and stability by Rac1 and Rho kinase: evidence for two forms of spine motility. *Mol Cell Neurosci* 26, 429–440.
- Togashi, H., Abe, K., Mizoguchi, A., Takaoka, K., Chisaka, O., and Takeichi, M. (2002). Cadherin regulates dendritic spine morphogenesis. *Neuron* 35, 77–89.
- Trachtenberg, J. T., Chen, B. E., Knott, G. E., Feng, G., Sanes, J. R., Welker, E., and Svoboda, K. (2002). Long-term *in-vivo* imaging of experience-dependent synaptic plasticity In adult cortex. *Nature* 420, 788–794.
- Uchida, N., Honjo, Y., Johnson, K. R., Wheelock, M. J., and Takeichi, M. (1996). The catenin/cadherin adhesion system is located in synaptic junctions bordering transmitter release zones. *J Cell Biol* 135, 767–779.
- Valiant, L. G. (1984). A theory of the learnable. *Communications of the ACM* 27, 1134–1142.
- Westermann, G. (2000) Constructivist Neural Networks Models of Cognitive Development, Ph.D. Thesis, University of Edinburgh, Edinburgh.
- Wheelock, M. J., and Johnson, K. R. (2003). Cadherins as modulators of cellular phenotype. *Annu Rev Cell Dev Biol* 19, 207–235.
- White, J. G., Amos, W. B., and Fordham, M. (1987). An evaluation of confocal versus conventional imaging of biological structures by fluorescence light microscopy. *J Cell Biol* 105, 41–48.
- Wong, W. T., and Wong, R. O. (2000). Rapid dendritic movements during synapse formation and rearrangement. *Curr Opin Neurobiol* 10, 118–124.

- Yamagata, M., Sanes, J. R., and Weiner, J. A. (2003). Synaptic adhesion molecules. *Curr Opin Cell Biol* 15, 621–632.
- Yu, X., and Malenka, R. C. (2003). Beta-catenin is critical for dendritic morphogenesis. *Nat Neurosci* 6, 1169–1177.
- Yuste, R. (2000). The discovery of dendritic spines. In International Brain Research Organization (http://www.ibro.info/Pub_Main_Display.asp?Main_ID=59).
- Yuste, R., and Bonhoeffer, T. (2001). Morphological changes in dendritic spines associated with long-term synaptic plasticity. *Annu Rev Neurosci* 24, 1071-1089.
- Yuste, R., Lanni, F., and Konnerth, A., eds. (2000). *Imaging Neurons: A Laboratory Manual* (New York, NY: Cold Spring Harbor Laboratory Press).
- Zahn, C. T., and Roskies, R. Z. (1972). Fourier descriptors for closed curves. *IEEE Transactions on Computers* C 21, 269–281.
- Zhou, Q., Homma, K. J., and Poo, M. M. (2004). Shrinkage of dendritic spines associated with long-term depression of hippocampal synapses. *Neuron* 44, 749–757.
- Zito, K., Knott, G., Shepherd, G. M., Shenolikar, S., and Svoboda, K. (2004). Induction of spine growth and synapse formation by regulation of the spine actin cytoskeleton. *Neuron* 44, 321–334.
- Zito, K., and Svoboda, K. (2002). Activity-dependent synaptogenesis in the adult mammalian cortex. *Neuron* 35, 1015–1017.
- Zuo, Y., Yang, G., Kwon, E., and Gan, W. B. (2005). Long-term sensory deprivation prevents dendritic spine loss in primary somatosensory cortex. *Nature* 436, 261–265.